NUMERICAL EVALUATION OF POROSITY BAND FORMATION AS A MECHANISM FOR MELT FOCUSING AT MID-OCEAN RIDGES

A Thesis Submitted to the College of Graduate Studies and Research in Partial Fulfilment of the Requirements for a Degree in Master of Science from the Department of Geological Sciences, University of Saskatchewan, Saskatoon, Saskatchewan

By

David Gebhardt

Permission to Use

In presenting this thesis in partial fulfillment of the requirements for a Postgraduate degree from the University of Saskatchewan, I agree that the Libraries of this University may make it freely available for inspection. I further agree that permission for copying of this thesis in any manner, in whole or in part, for scholarly purposes may be granted by the professor who supervised my thesis work or, in their absence, by the Head of the Department or the Dean of the College in which my thesis work was done. It is understood that any copying or publication or use of this thesis or parts thereof for financial gain shall not be allowed without my written permission. It is also understood that due recognition shall be given to me and to the University of Saskatchewan in any scholarly use which may be made of any material in my thesis.

Requests for permission to copy or to make other uses of materials in this thesis in whole or part should be addressed to:

Head of the Department of Geological Sciences
114 Science Place
University of Saskatchewan
Saskatoon, Saskatchewan
S7N 5E2
Canada

OR

Dean
College of Graduate Studies and Research
University of Saskatchewan
107 Administration Place
Saskatoon, Saskatchewan
S7N 5A2
Canada

Abstract

It has been well established through various experimental and numerical studies that imposing an external shear on a system of partial melt will result in the compaction of the solid matrix and expulsion of the interstitial liquid melt; this leads to the formation of regions of contrasting high and low porosity that are commonly referred to as melt bands. An early numerical study of melt bands speculated that these structures could contribute to melt extraction at mid-ocean ridges. This thesis examines the formation of melt bands beneath mid-ocean ridges. With linear and nonlinear models similar to those from previous numerical melt band studies, melt bands are evaluated as a mechanism for lateral melt extraction using the shear geometry derived from the velocity field of the plate-driven corner flow of a mid-ocean ridge. The degree of similarity between previous numerical and experimental results has been found to be greatly influenced by the imposed rheology of the solid matrix phase. Knowing this, the numerical models in this contribution will use three different matrix shear viscosity laws: isotropic strain rate independent, isotropic strain rate dependent and anisotropic strain rate independent.

The linear analysis indicates that though fast growing bands may be oriented toward the ridge axis, the bands that undergo the greatest change in porosity over time are oriented toward the lithosphere-asthenosphere boundary at the base of the plate. The nonlinear simulations produce bands with orientations similar to those found in the linear analysis, along with a great deal of unexpected porosity accumulation present on the boundaries of the model domain. These models indicate that melt bands will not likely act as high permeability melt-channeling conduits except near the lithosphere-asthenosphere boundary at the base of the plate.

These models are highly sensitive to the poorly defined matrix bulk viscosity, with an increased bulk viscosity resulting in little or no development of significant band-like structures. The models are also sensitive to the initial heterogeneity, which, like the bulk viscosity, is also poorly defined; too great an initial heterogeneity results in the bands quickly surpassing the disaggregation limit for mantle rocks.

Acknowledgments

I am very grateful for the opportunity I have had to work with my supervisor, Dr. Samuel Butler, over the course of this project. The guidance and support he provided has been an invaluable part of the research and work involved in the compilation of this document.

Table of Contents

List of Figures

List of Tables

Chapter 1: Introduction

In this first chapter I present a summary of background information pertaining to this research project. I begin with a discussion of the structure and theory of mid-ocean ridges (MORs), both in terms of dynamic behaviour and constituent material. Following this, I discuss in more detail the investigations that have been conducted concerning partial melt, the material found at MORs. Next, I present an explanation of the unique features of this research project that set it apart from similar work. Finally, I present an outline for the rest of this contribution.

1.1 Mid-Ocean Ridges

First identified in the nineteenth century depth soundings (Searle, 2013), MORs have been a popular area of investigation for geoscientists for decades. As time has passed, improvements in geophysical and geological survey methods have allowed for increasingly accurate descriptions of the subsurface structure at MORs. Bathymetric and seismic surveys have established that melt is extracted from MORs within 1 km of the ridge axis (Vera et al, 1990). The study of ophiolites massifs has given petrological insight into the dynamics at MORs (Ceuleneer and Rabinomicz, 1992). Ophiolites are uplifted portions of oceanic crust and underlying mantle rock that have become emplaced on continental crust typically as part of an orogenic event. These structures demonstrate a flow pattern that is driven by internal buoyancy near the ridge axis that gives way to a plate-spreading controlled flow at distances of a few tens of kilometers from the ridge axis. An example of the melt delivery system running along the ridge axis has been preserved in the Masqad area of the Oman ophiolite. The Masqad area also demonstrates melt-migrating structures that indicate a coupling between melt migration and the flow of the solid material of the mantle (Ceuleneer and Rabinomicz, 1992). A later combination of electromagnetic and seismic surveys found evidence of melt down to a depth of approximately 100 km below the ridge crest in a broad region extending nearly 100 km off-axis (Forsyth et al. 1998). Geochemical evidence (Kelemen et al., 1997) points to the need for a rapid melt transportation mechanism directed to the extraction point at the ridge crest. An illustration of the structure of MORs is given in Figure 1.

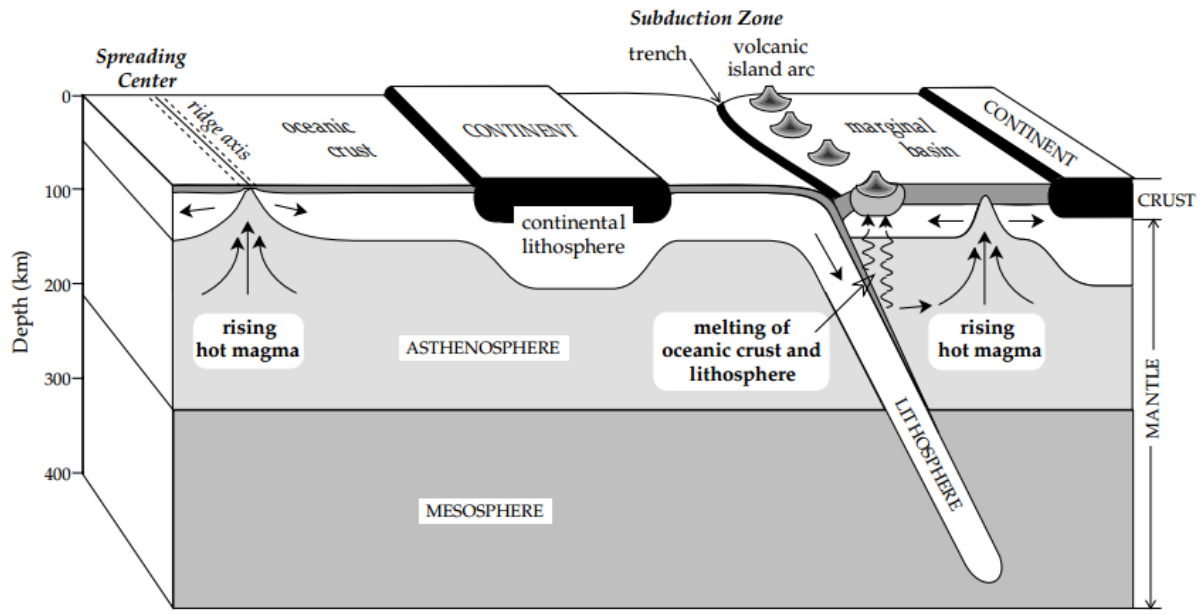

Figure 1: Hypothetical vertical cross-section from the surface of the Earth to the part-way into the mantle. The MOR, identified as a spreading centre, overlays an upwelling of mantle melt. MORs play a vital role in plate tectonics, since they are the location where new oceanic crust is formed. This figure is taken from Lowrie (2007).

Theoretical models explaining the behaviour of MORs have accompanied these observational studies. These models describe the dynamics of both the material present within the MOR and the MORs as a system. Ahern and Turcotte (1979) described a model for magma migration at MORs based on porous media flow and a passive spreading model by Lachenbruch (1976) described motion for a MOR corner flow based on a viscous incompressible fluid. Equations governing partial melt systems consisting of a compacting, viscous matrix and an interstitial melt were derived by McKenzie (1984) and Scott and Stevenson (1984). These contributions present equations describing the mass and force balance for both the matrix and melt phases. A later MOR corner flow model incorporating the two-phase fluid dynamics of McKenzie described a velocity field for both matrix and melt phases (Spiegelman and McKenzie, 1987).

1.2 Partial Melt and Melt Bands

Much work has been done using the governing equations of systems of partial melt in both numerical and experimental settings. An early theoretical model by Stevenson (1989) determined that strain-induced porosity instabilities would occur in the presence of porosity-

weakening rheology. Later numerical work by Richardson (1998) confirmed the existence of the band-like structures perpendicular to the direction of maximum compression. In that same contribution, Richardson suggested that the formation of these strain-induced bands could act as a potential mechanism for melt extraction at MORs. This suggestion would not be addressed again for almost a decade.

Laboratory studies of melt band formation have been conducted on synthetic rock aggregates that approximate MOR basalts in terms of both composition and physical characteristics using both direct shear (Holtzman et al., 2003; Holtzman and Kohlstedt, 2007) and torsional shear (Kohlstedt et al., 2010; King et al., 2010; Qi et al., 2015) geometries. These experimental studies used both Newtonian and non-Newtonian matrix rheology regimes (King et al., 2010). All of these contributions found the porosity instability to exist in sample sizes larger than the compaction length of the sample material. The compaction length is the characteristic length scale of two-phase partial melt systems, defined by the bulk and shear viscosities of the matrix, the matrix permeability and the viscosity of the melt, over which gradients in melt pressure and melt fraction can be sustained (McKenzie, 1984). The bands that formed in these experiments were found to be oriented approximately 20° from the shear plane and approximately 25° from the direction of maximum compression.

A large number of numerical simulations have been used to study the behaviour of porosity instabilities in partial melt. This work has made use of both linear approximations and full non-linear models. Using simple shear flow geometry and a Newtonian, porosity-weakening rheology, the linear analysis of Speigelman (2003) produced bands parallel to the direction of maximum compression, or 45° from the shear plane. Subsequent simple shear studies used a non-Newtonian, porosity weakening rheology in both linear and nonlinear models (Katz et al., 2006; Butler, 2009). Introducing this change to the matrix rheology produced bands at 15°-20° from the shear plane, making these results more in line with experimental band orientations. However, these low-angle orientations were only achieved for a high strain rate dependence ($n_v = 6$) outside of the typically acceptable range for mantle materials ($n_v \approx 3.5$) (Hirth and Kohlstedt, 2003; Korenega and Karato, 2008). These low-angle results were also at odds with experimental melt band studies that saw band segregation persist in both strain rate independent and dependent regimes (King et al., 2010). An example of numerical melt bands generated using

Comsol Multiphysics is shown in Figure 2. This model used simple shear and a Newtonian rheology, resulting in bands forming near 45° clockwise from horizontal.

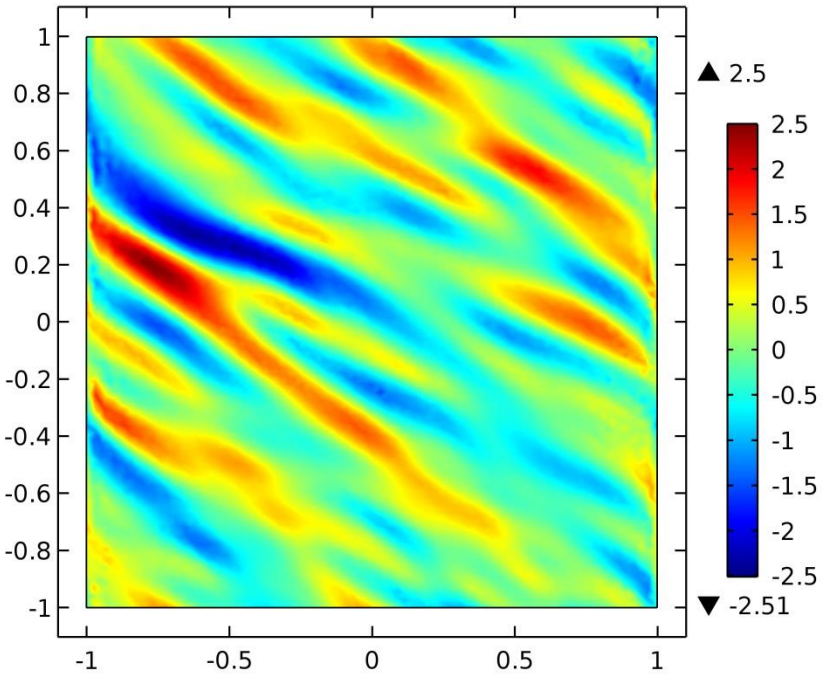

Figure 2: Example of bands grown in simple shear using a Newtonian matrix rheology. The porosity field has been normalized in time so as to make the onset of band growth clear throughout the simulation. The actual porosity high (warm colors) in this figure is 0.0102 and the porosity low (cool colors) is 0.00983. The axes of the figure define a box that is 2x2 compaction lengths large in space.

A new anisotropic matrix rheology model was proposed by Takei and Holtzman (2009), and later modified by Takei and Katz (2013), as a possible explanation for the existence and persistence of low-angle melt bands. Arguing that melt arrangement within the matrix is anisotropic at the grain-scale, an anisotropic viscosity tensor that couples the shear and volumetric components of the matrix stress/strain rate was presented that accounts for a preferential alignment of melt pockets along grain boundaries in two-phase systems under stress (Takei and Katz, 2013; Daines and Kohlstedt, 1997). This new viscosity model was applied in the numerical work of Butler (2012) and Katz and Takei (2013) where low-angle bands formed in the presence of the anisotropy. However, these bands rotated to high angles in the presence of high strain, contradicting what was seen in high strain experimental observations (Holtzman and Kohlstedt, 2007). The experiments of Qi et al. (2015) have verified concepts from the theory for anisotropic viscosity in torsional deformation at large strain. However, there is still significant discrepancy between the results of experimental and numerical melt band formation.

1.3 The Focus of This Contribution

Recent MOR models focus on a variety of topics, such as the effects of chemical heterogeneity on melt extraction (Katz and Weatherley, 2012) and the origin of axisymmetric melt distribution (Katz, 2010). However, there are not many contributions that are chiefly concerned with the formation and effects of melt bands at MORs. In their study of melt band formation under simple shear with non-Newtonian rheology, Katz et al. (2006) demonstrated that imposing low-angle bands consistent with non-Newtonian numerical models and partial melt experiments resulted in bands that were oriented largely toward the ridge axis and crest; this direction is considered to be ideal for channelling directly to the ridge axis. This result was found by imposing a 25° retrograde rotation from the direction of principal compressive strain-rate, found from the strain-rate tensor for a temperature and strain rate dependent rheology in a mid-ocean ridge corner flow model.

My work primarily differs from the approach taken by Katz et al. (2006) in that instead of imposing fixed band orientations based on numerical and experimental work on the principal strain-rate axes throughout the MOR domain, I am interested in the rotation and change in amplitude experienced by the bands as they progress along MOR corner flow streamlines from deep in the mantle to the base of the plate at the lithosphere-asthenosphere boundary. I utilize both linear and nonlinear models in this work. With the linear analysis I am interested in finding the orientation of the fastest growing bands as well as the evolved orientation for the bands with the maximum perturbation amplitudes. This is done using a variety of initial orientations along multiple streamlines in the MOR domain. With the nonlinear models I am interested in observing band evolution MOR streamlines for the complete and nonlinear equations governing systems of partial melt. Along with this, I am interested in comparing the results of the linear and nonlinear models so as to test the predictions of the linear theory. Both models neglect buoyancy and thermodynamics, and each model will test all three commonly accepted matrix viscosity laws: isotropic strain rate independent, isotropic strain rate dependent, and isotropic strain rate independent.

1.4 Thesis Overview

Four chapters follow this introduction, for a total of five in this thesis. The second chapter presents the background theory of this project. This includes a discussion of the governing equations for partial melt and a presentation of both the matrix viscosity laws, and MOR geometry. The third chapter of this thesis discusses the numerical methods used to conduct the research, focusing primarily on the equations needed for the linear analysis as well as the algorithms for both the linear and nonlinear models. The fourth chapter presents and discusses the results of the numerical models. The linear analysis results are presented first, followed by the nonlinear results, which in turn is followed by a comparison between the two models. Finally, the last chapter presents the conclusions of this study along with potential future considerations. A list of references follows the last chapter along with a number of appendices.

Chapter 2: Theory

This chapter presents the background theory necessary to understand this research project. I begin this section by introducing mass and force balance equations that govern systems of partial melt, after which I gradually modify the equations into the form used for this research project. Following this, three different matrix viscosity laws are discussed. This chapter ends in presenting the geometry of a MOR and its velocity field.

2.1 Dimensional Governing Equations for Systems of Partial Melt

The equations governing compacting two-phase systems were derived by McKenzie (1984) and Scott and Stevenson (1984). In those contributions, the presented equations described the movement of both the melt and matrix phases in a system of partial melt in terms of force and mass balances. The dimensional form of these equation are given by

$$\frac{\partial \phi}{\partial t} + \nabla \cdot (\phi \vec{u}) = 0, \tag{1}$$

$$\frac{\partial (1-\phi)}{\partial t} + \nabla \cdot \left((1-\phi)\vec{U}\right) = 0, \tag{2}$$

$$\phi\left(\vec{u} - \vec{U}\right) = -\frac{k_\phi}{\mu}(\nabla P), \tag{3}$$

$$\nabla P(1+\xi) = \nabla \cdot \boldsymbol{\sigma}, \tag{4}$$

In these equations, ϕ is porosity, P is the fluid pressure, $\vec{u}$ is the fluid velocity, and $\vec{U}$ is the matrix velocity. In the present analysis, all computations are completed using two-dimensional Cartesian geometry so each fluid velocity has a horizontal and vertical component, u and v for the melt phase, respectively, and U and V for the matrix phase, respectively. Matrix permeability is denoted by k_ϕ, μ is the melt viscosity, and ξ is the matrix bulk viscosity. Matrix permeability is taken to be $k_\phi = \left(\frac{\phi}{\phi_0}\right)^3$ (Carmen, 1939), where ϕ_0 is the initial background porosity. Finally, $\boldsymbol{\sigma}$ is the deviatoric stress tensor. Following Takei and Holtzman (2009), the components of $\boldsymbol{\sigma}$ are related to the strain rate components by

$$\begin{pmatrix} \sigma_{xx} \\ \sigma_{yy} \\ \sigma_{xy} \end{pmatrix} = \begin{pmatrix} \xi+\eta & \xi-\eta & 0 \\ \xi-\eta & \xi+\eta & 0 \\ 0 & 0 & 2\eta \end{pmatrix} \begin{pmatrix} \dot{\epsilon_{xx}} \\ \dot{\epsilon_{yy}} \\ \dot{\epsilon_{xy}} \end{pmatrix}, \tag{5}$$

where $\dot{\epsilon_{ij}}$ denote the components of the strain rate tensor and η is the matrix shear viscosity. The strain rate components in equation (5) are defined as $\dot{\epsilon}_{xx} = \frac{\partial U}{\partial x}, \dot{\epsilon}_{yy} = \frac{\partial V}{\partial y}$, and $\dot{\epsilon}_{xy} = \frac{1}{2}\left(\frac{\partial U}{\partial y} + \frac{\partial V}{\partial x}\right)$. The matrix bulk viscosity is defined as $\xi = \frac{5}{3}\eta$, in keeping with Takei and Katz (2013).

Equations (1) and (2) correspond to the mass balance equations for the interstitial melt and viscous matrix phases, respectively. Equation (1) states that increasing the amount of melt in a representative elementary volume (REV) containing the two fluid phases results in an increase in porosity, while equation (2) states that increasing the amount of matrix in an REV results in a decrease in porosity. Equations (3) and (4) denote the force balances for the two fluid phases. Equation (3), a modified version of Darcy's Law, describes the force balance for the melt phase. It states that motion of the melt phase is driven by pressure gradients. Equation (4) is the mass balance for the matrix phase, and it states that pressure gradients in an REV are balanced by viscous forces of the matrix phase. Together, the melt and matrix phases in partial melt are considered to be incompressible. This can be demonstrated by adding equation (1) and (2) to yield:

$$\nabla \cdot [\phi\vec{u} + (1-\phi)\vec{U}] = 0. \tag{6}$$

In their original form, the governing equations include terms that account for melting and gravity. However, both of these effects are neglected in the current contribution. This clearly means that the models used in this work are not fully Earth-like. However, by neglecting gravity and thermodynamics, I focus on melt-band formation as purely the result of the background shear generated by the MOR corner flow.

2.2 Removing Fluid Velocity Dependence

It is possible to simplify the governing equations by removing dependence on the melt velocity from the melt force balance equation. To do this, begin by re-writing Equation (6) as

$$\nabla \cdot \left[\left(\vec{u} - \vec{U}\right)\phi\right] = -\nabla \cdot \vec{U} \tag{7}$$

Next, taking the divergence of equation (3) allows for the substitution of equation (7)

$$\nabla \cdot \left[\left(\vec{u} - \vec{U}\right)\phi\right] = -\nabla \cdot \vec{U} = \nabla \cdot \left[-\frac{k_\phi}{\mu}(\nabla P)\right]$$

$$\rightarrow \nabla \cdot \vec{U} = \nabla \cdot \left[\frac{k_\phi}{\mu} (\nabla P) \right] \tag{8}$$

Equation (8) now describes a force balance that is free of the melt velocity.

2.3 Non-Dimensionalization

To further simplify analysis, the following dimensionless parameters are introduced:

$$\begin{cases} x' = \dfrac{x}{\delta_c} \\ t' = t\dot{\gamma} \\ k'_\phi = \dfrac{k_\phi}{k_{\phi 0}} \\ \eta' = \dfrac{\eta}{\eta_0} \\ \xi' = \dfrac{\xi}{\eta_0} \\ U' = \dfrac{U}{U_0} \\ P' = \dfrac{P}{P_0} \\ \sigma' = \dfrac{\sigma}{\eta_0 U_0 / \delta_c} \end{cases} . \tag{9}$$

Lengths are scaled by the compaction length δ_c and time is scaled by the inverse strain rate $\dot{\gamma}$, while permeability and both matrix viscosities are scaled by their respective initial values. The initial velocity scale is given by $U_0 = \dot{\gamma}\delta_c$ and the pressure scale is defined as $P_0 = \frac{\eta_0 U_0}{\delta_c}$. The compaction length is defined as

$$\delta_c = \sqrt{\frac{(\xi + 1)\eta_0 k_0}{\mu}}. \tag{10}$$

The compaction length is the characteristic length scale for systems of partial melt over which gradients in melt pressure and melt fraction can be sustained (McKenzie, 1984). When deformation of partial melt takes place at a length scale larger than the compaction length, significant deformation of the solid will occur. However, deformation at length scales smaller than the compaction length results in motion of only the interstitial melt. The compaction length for mantle rocks with low melt fraction varies from 10 to 10^4 m (Keleman et al., 1997).

Taking these scaled parameters into account leads to a new set of dimensionless equations:

$$\frac{\partial(1-\phi)}{\partial t'} + \nabla \cdot \left((1-\phi)\overrightarrow{U'}\right) = 0, \tag{11}$$

$$\nabla \cdot \overrightarrow{U'} = \nabla \cdot [(\nabla P')], \tag{12}$$

$$\nabla P'(1+\xi') = \nabla \cdot \boldsymbol{\sigma}'. \tag{13}$$

2.4 Matrix Shear Viscosity Laws

Three different matrix shear viscosity laws are used in this project: isotropic, strain rate independent; isotropic, strain rate dependent; and, anisotropic, strain rate independent. All of these laws share a porosity weakening dependence. Both of the isotropic viscosities are determined from the following equation

$$\eta = exp\left(\frac{\lambda(\phi-\phi_0)}{n_v}\right)\left[\frac{1}{\sqrt{2}}\left[\left(\frac{dU}{dx}\right)^2 + \left(\frac{dV}{dy}\right)^2 + \frac{1}{2}\left(\frac{dU}{dy}+\frac{dV}{dx}\right)^2\right]^{\frac{1}{2}}\right]^{\frac{(1-n_v)}{n_v}}, \tag{14}$$

where $\lambda = -25$ (Mei et al, 2002). In this equation ϕ_0 is the initial porosity, and n_v is the strain exponent. Newtonian viscosity is achieved by setting the strain exponent, n_v, to 1 while $n_v \neq 1$ yields non-Newtonian viscosities corresponding to different creep regimes for mantle materials (Korenaga and Karato, 2008, Hirth and Kohlstedt, 2003).

The anisotropic viscosity model comes from Takei and Katz (2013), which is a generalized version of a previous model from Takei and Holtzman (2009). It is centered on the introduction of an anisotropic viscosity tensor. That tensor in two dimensions is given by

$$C_{ijkl} = e^{-\lambda(\phi-\phi_0)}\begin{bmatrix} r_\xi + \frac{4}{3} + \alpha\cos^4\Theta & r_\xi - \frac{2}{3} + \alpha\sin^2 2\Theta & -\alpha\cos^3\Theta\sin\Theta \\ r_\xi - \frac{2}{3} + \alpha\sin^2 2\Theta & r_\xi + \frac{4}{3} + \alpha\sin^4\Theta & -\alpha\cos\Theta\sin^3\Theta \\ -\alpha\cos^3\Theta\sin\Theta & -\alpha\cos\Theta\sin^3\Theta & 1 - \frac{\alpha}{4}\sin^2 2\Theta \end{bmatrix}. \tag{15}$$

New terms in this equation are the anisotropy angle, Θ, and the anisotropy magnitude, α. In equation (15), r_ξ is the constant of proportionality relating the bulk and shear viscosity of the matrix phase and is taken to be 5/3 (Takei and Katz, 2013). Following Takei and Katz (2013), the anisotropy angle is defined to be the local direction of maximum tensile stress. The magnitude is defined as

$$\alpha = 2\tanh\left(\frac{2(\sigma_3 - \sigma_1)}{\sigma_{sat}}\right), \tag{16}$$

where $\sigma_1, \sigma_3, \sigma_{sat}$ are the principal compression, principal tension and the saturation stress, respectively. The saturation stress is defined as a material property, and is taken to be 2 as in Takei and Katz (2013) where stress is made dimensionless by the background viscosity and strain-rate. Isotropic viscosity can be generated from equation (16) by setting $\alpha = 0$. A more detailed consideration of this anisotropic viscosity model is given in Appendix 2.

2.5 Mid-Ocean Ridge Geometry

The MOR geometry model I use was originally defined by Spiegelman and McKenzie (1987). In that contribution, the authors present a corner flow model based on the similarity solution in polar coordinates for two-dimensional flow in a corner derived by Batchelor (1967) with boundary condition appropriate for MOR geometry. This model is isoviscous, incompressible, as well as axisymmetric. Figure 3 shows the resulting geometry of this model. The streamlines shown in Figure 3 are the trajectories for REVs of melt matrix material. Both fast and slow spreading ridges can be accommodated by changing the wedge angle, which is defined as the angle between horizontal and the lithosphere-asthenosphere boundary. Figure 3a shows a slow spreading ridge where the wedge angle is approximately 40°, while Figure 3b shows a fast spreading ridge with a wedge angle of 13°.

Figure 4 contains the same ridge geometry, but shows the variation in orientation of the strain-rate axes of tension (red) and compression (black) throughout the sub-plate MOR domain. These axes are orthogonal, as is expected due to the symmetry of the strain-rate tensor for the MOR corner flow. Previous work with compacting systems has shown that these directions are very important, as porosity bands tend to form at angles relative to the angle of maximum compression, and as the main components of the anisotropic viscosity model are dependent on the directions of maximum tension and maximum compression. The principal axes in Figure 4b are similar to the axes for highly strain-rate and temperature dependent matrix viscosity (Katz et al, 2006). Takei and Holtzman (2009) also used the isoviscous corner flow in models of the fluid pressure gradients at MORs.

This model produces a two-component velocity field defined by

$$U = B(tan^{-1}\left(\frac{x}{y}\right) - (\frac{xy}{x^2 + y^2})), \tag{17}$$

$$V = -A + B(\frac{x^2}{x^2 + y^2}), \tag{18}$$

where A and B are constants resulting from the MOR boundary conditions that both depend on the wedge angle of the ridge. A detailed derivation of these velocity components can be found in Appendix 3.

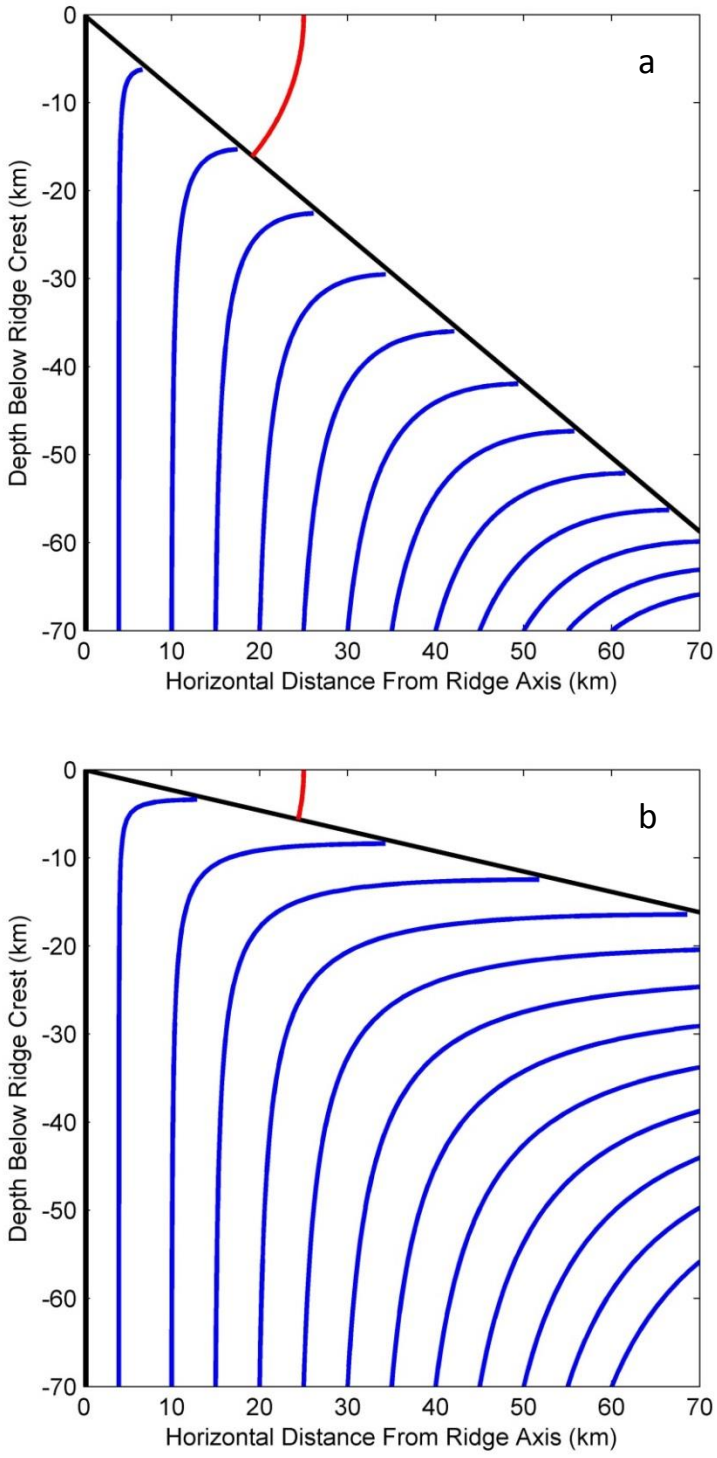

Figure 3: MOR geometry for a) slow spreading ridges and b) fast spreading ridges. Blue lines denote the corner flow streamlines, which are defined in Appendix 1. The lithosphere-asthenosphere boundary is given by the inclined black line, while the vertical black line represents the axis of symmetry for the ridge, with the origin being the ridge axis. The angle between the lithosphere-asthenosphere boundary and horizontal, given by the red curve, defines the wedge angle. The slow spreading geometry in a) was previously published by Gebhardt and Butler (2016).

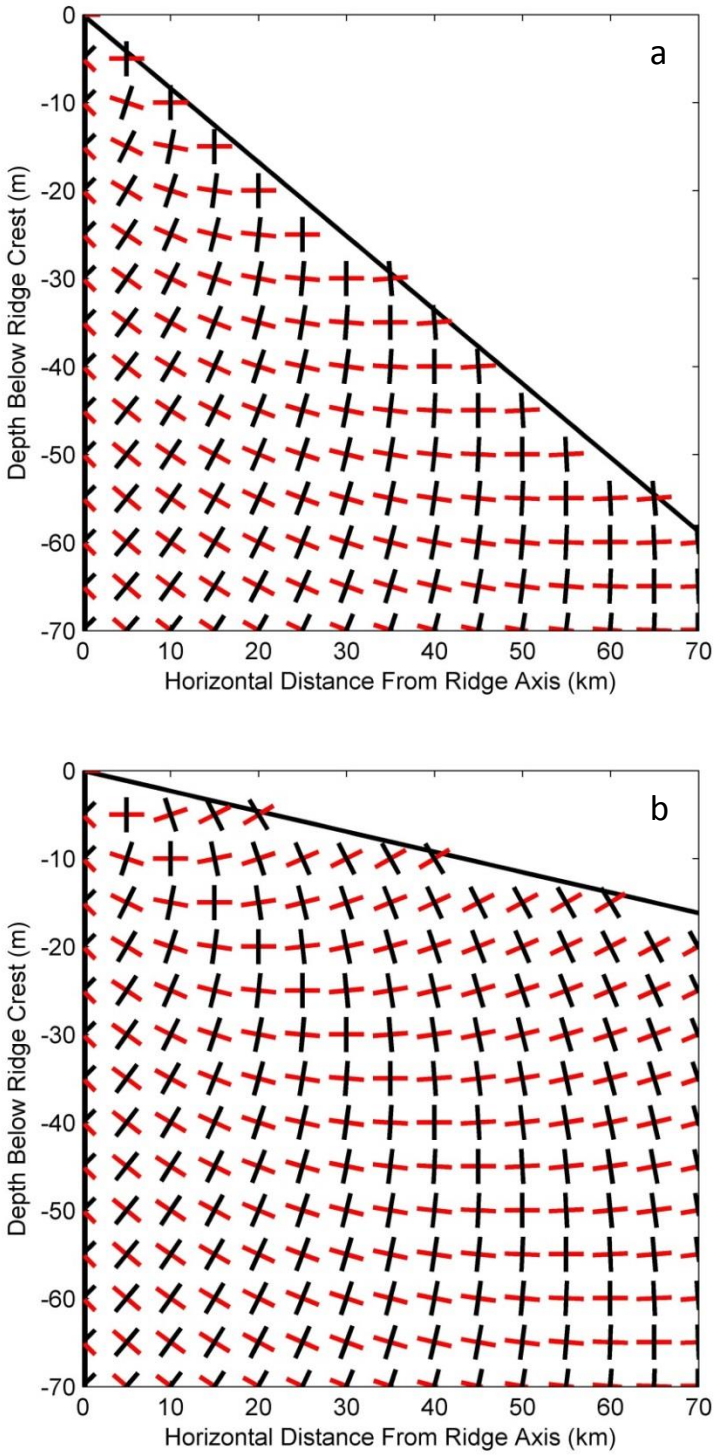

Figure 4: Directions of maximum compression (black) and maximum tension (red) for both a) slow spreading and b) fast spreading MOR geometry. The slow spreading geometry with principle axes in a) was previously published by Gebhardt and Butler (2016).

Chapter 3: Methods of Analysis

In this chapter, I present the two mathematical methods I used in the analysis of melt band formation in the corner flow of a MOR. Both methods are calculated in a reference frame that moves along a MOR streamline with the background flow. The first of these methods is a linear instability analysis, or linear perturbation analysis; the second is a simulation of the nonlinear governing equations. Linear instability analysis is a common method of investigation for fluid systems. It is a useful way of identifying the ideal physical conditions required for the onset of interesting behaviour in a fluid system. The mathematics involved with this method reduces a typically complicated fluid system to a relatively simple model. Simulations of the governing equations, on the other hand, utilize numerical schemes to generate approximate but complete models of fluid systems.

3.1 Linear Analysis Overview

In the perturbation analysis, the porosity field is decomposed into plane waves (Spiegelman, 2003) of the form

$$\phi = \phi_0 + \Delta\phi exp\left(i\big(k_x(t)x + k_y(t)y\big) + s(t)\right). \tag{19}$$

In equation (19), $\Delta\phi$ corresponds to the initial porosity perturbation amplitude, $k_x(t)$ and $k_y(t)$ correspond to orientation-defining wavenumbers in the x and y directions and $s(t)$ corresponds to the amplitude of the porosity perturbation. All first order perturbations of the other dynamical variables are assumed to be proportional to the ϕ perturbation. Only linear variations of the background velocity are taken into account in our analysis. This approximation is valid provided that the modeled fluid parcels are much smaller than the length scale of the MOR domain over which the flow is changing.

The wavenumbers are considered to be time dependent just as in the linear analysis of Spiegelman (2003). However because the mid-ocean ridge produces a shear with both simple and pure components, this contribution uses more general evolution equations for the wavenumbers (Craik and Criminale, 1986) given by:

$$\frac{dk_x}{dt} = -\frac{dU}{dx}k_x - \frac{dV}{dx}k_y, \tag{20}$$

$$\frac{dk_y}{dt} = -\frac{dU}{dy}k_x - \frac{dV}{dy}k_y. \tag{21}$$

Equations (20) and (21) describe the rotation of the bands by the background flow.

The multi-component shear of the corner flow also leads to a growth rate that is different than that found in previous theoretical melt band studies. In general, the growth rate for the porosity perturbations is defined by

$$\frac{ds}{dt} = (1-\phi_0)\left(ik_x(t)\tilde{U} + ik_y(t)\tilde{V}\right). \tag{22}$$

In this equation, $\tilde{U}$and $\tilde{V}$ are the coefficients indicating the amplitude of the horizontal and vertical velocity perturbation components, respectively, relative to the porosity perturbation amplitude. A detailed derivation of equations (20), (21), and (33) is given in Appendix 4.

3.2 Isotropic, Strain Rate Independent Growth Rate Derivation

Deriving the growth rate for each of the three rheology laws is focused on determining the coefficients $\tilde{U}$ and $\tilde{V}$. Similar to the growth rate derivation method used in Butler (2012), I begin with equations (12) and (13), the force balance equations for both phases. These equations will be written to first order and Fourier transformed. Applying these operations to equation (12) yields

$$ik_x\tilde{U} + ik_y\tilde{V} = -\left(k_x^2 + k_y^2\right)\tilde{P}, \tag{23}$$

where the tildas denote Fourier transformed quantities.

Accomplishing the same work on equation (13) is a more involved process, as the equation is more complex. Expanding the vector calculus operators in equation (13) yields two equations:

$$\frac{\partial}{\partial x}\left[-P(\xi+1) + (\xi+1)\eta\frac{\partial U}{\partial x} + (\xi-1)\eta\frac{\partial V}{\partial y}\right] + \frac{\partial}{\partial y}\left[\eta\left(\frac{\partial U}{\partial y} + \frac{\partial V}{\partial x}\right)\right] = 0, \tag{24}$$

$$\frac{\partial}{\partial y}\left[-P(\xi+1) + (\xi-1)\eta\frac{\partial U}{\partial x} + (\xi+1)\eta\frac{\partial V}{\partial y}\right] + \frac{\partial}{\partial x}\left[\eta\left(\frac{\partial U}{\partial y} + \frac{\partial V}{\partial x}\right)\right] = 0. \tag{25}$$

The isotropic, strain rate independent matrix shear viscosity is given by

$$\eta = e^{\lambda(\phi-\phi_0)}. \tag{26}$$

Applying a Taylor series expansion with respect to ϕ about ϕ_0, the viscosity can be re-written to first order as

$$\eta = 1 + \lambda\phi' \tag{27}$$

where $\phi' = (\phi - \phi_0)$. The strain rate terms can also be written in terms of zeroth and first order terms, representing the background MOR corner flow strain rate and the first order variation from the background strain-rate, respectively. An example of this strain rate decomposition is given by

$$\frac{\partial U}{\partial x} = \frac{\partial U_b}{\partial x} + \frac{\partial U_1}{\partial x} \tag{28}$$

where the subscript b denotes the zeroth order background strain and the subscript 1 denotes the first order variation.

Applying these first order perturbations to equations (24) and (25) and writing the result to first order yields

$$\begin{aligned} -\frac{\partial P}{\partial x}(\xi+1) + (\xi+1)\left[\lambda\frac{\partial\phi'}{\partial x}\frac{\partial U_b}{\partial x} + \frac{\partial^2 U_1}{\partial x^2}\right] + (\xi-1)\left[\lambda\frac{\partial\phi'}{\partial x}\frac{\partial V_b}{\partial y} + \frac{\partial^2 V_1}{\partial x\partial y}\right] \\ + \lambda\frac{\partial\phi'}{\partial y}\left(\frac{\partial U_b}{\partial y} + \frac{\partial V_b}{\partial x}\right) + \frac{\partial^2 U_1}{\partial y^2} + \frac{\partial^2 V_1}{\partial x\partial y} = 0, \end{aligned} \tag{29}$$

$$\begin{aligned} -\frac{\partial P}{\partial y}(\xi+1) + (\xi+1)\left[\lambda\frac{\partial\phi'}{\partial y}\frac{\partial V_b}{\partial y} + \frac{\partial^2 V_1}{\partial y^2}\right] + (\xi-1)\left[\lambda\frac{\partial\phi'}{\partial y}\frac{\partial U_b}{\partial x} + \frac{\partial^2 U_1}{\partial x\partial y}\right] \\ + \lambda\frac{\partial\phi'}{\partial x}\left(\frac{\partial U_b}{\partial y} + \frac{\partial V_b}{\partial x}\right) + \frac{\partial^2 U_1}{\partial x\partial y} + \frac{\partial^2 V_1}{\partial x^2} = 0. \end{aligned} \tag{30}$$

Taking the Fourier transform of equations (29) and (30), grouping like terms, and accounting for the incompressibility of the background flow results in

$$\begin{aligned} -(\xi+1)ik_x\tilde{P} - \left((\xi+1)k_x^2 + k_y^2\right)\widetilde{U} + \xi k_y k_x \tilde{V} \\ = -\lambda\left(2\frac{\partial U_b}{\partial x}ik_x + \left(\frac{\partial U_b}{\partial y} + \frac{\partial V_b}{\partial x}\right)ik_y\right)\widetilde{\phi'}, \end{aligned} \tag{31}$$

$$\begin{aligned} -(\xi+1)ik_y\tilde{P} - \xi k_y k_x\widetilde{U} + \left(k_x^2 + (\xi+1)k_y^2\right)\tilde{V} \\ = -\lambda\left(\left(\frac{\partial U_b}{\partial y} + \frac{\partial V_b}{\partial x}\right)ik_x + 2\frac{\partial V_b}{\partial y}ik_y\right)\widetilde{\phi'}. \end{aligned} \tag{32}$$

Finally, making the substitution $\widetilde{F'} = i\tilde{F}$, equations (23), (31) and (32) can be arranged in the following matrix equation

$$\begin{bmatrix} k_x^2+k_y^2 & -k_x & -k_y \\ -(\xi+1)k_x & (\xi+1)k_x^2+k_y^2 & \xi k_y k_x \\ -(\xi+1)k_y & \xi k_y k_x & k_x^2+(\xi+1)k_y^2 \end{bmatrix} \begin{bmatrix} \widetilde{P}' \\ \widetilde{U}' \\ \widetilde{V}' \end{bmatrix} = \begin{bmatrix} 0 \\ -\lambda\left(2\frac{\partial U_b}{\partial x}k_x + \left(\frac{\partial U_b}{\partial y}+\frac{\partial V_b}{\partial x}\right)k_y\right) \\ -\lambda\left(\left(\frac{\partial U_b}{\partial y}+\frac{\partial V_b}{\partial x}\right)k_x + 2\frac{\partial V_b}{\partial y}k_y\right) \end{bmatrix} \quad (33)$$

Using Mathematica to invert the matrix on the left hand side of equation (33), the vector of coefficients can be easily determined. Plugging the resulting coefficients for $\widetilde{U}$ and $\widetilde{V}$ into equation (22), the growth rate for the case of isotropic, strain rate independent matrix shear viscosity can be written as:

$$\frac{ds}{dt} = \frac{2\lambda(\phi_0-1)\left(k_x^2\frac{\partial U_b}{\partial x}+k_y^2\frac{\partial V_b}{\partial y}+k_xk_y\left(\frac{\partial U_b}{\partial y}+\frac{\partial V_b}{\partial x}\right)\right)}{(\xi+1)\left(k_x^2+k_y^2+1\right)}. \quad (34)$$

Similar derivations of the growth rates for the other two matrix rheologies can be found in Appendix 5 and 6.

3.3 Linear Analysis Algorithm

The linear analysis has a twofold goal: first, to identify the orientation of the fastest growing bands throughout the MOR domain; and second, to identify the orientation of the bands with the most significant porosity perturbation amplitude in the MOR domain. This analysis is accomplished using an ODE solver in Matlab. Equations (20), (21), and (22) constitute the system of ODEs that define the melt band behaviour in the MOR corner flow. These three equations, along with equations defining the MOR streamlines and velocity field from Spiegelman and McKenzie (1987), are solved simultaneously along multiple streamlines. Starting at streamlines close to the ridge axis and continuing onto streamlines increasingly farther from the axis, the centre of the solver domain begins at a depth of 70 km and continues along a streamline until its termination at the lithosphere-asthenosphere boundary. The depth to this boundary increases with increasing distance from the ridge axis for both slow spreading and

fast spreading MORs, as is shown in Figures 3 and 4. The geometry of the MOR is further explained in Appendix 1.

The results of the wavenumber ODEs are translated into band orientations through the substitution $k_x = |k|sin\theta$ and $k_y = |k|cos\theta$. In these definitions, θ is defined as the clockwise angle from the positive horizontal axis. Bands are evolved using a variety of initial angles in the range $\theta\epsilon[0,\pi]$, and a unit initial amplitude is imposed by setting $s(0) = 0$.

The fastest growing bands are identified by the maximum value of the growth rate as a function of an instantaneous, clockwise-positive orientation relative to horizontal, as seen in the top panel of Figure 5. In order to generate these angular spectra, equation (22) was evaluated at each integer angle in the range $[0,\pi]$ for each rheology case.

The orientation at which bands will grow the fastest is determined from the angular spectra of both the vertical and horizontal wavenumbers. The numerical results of equations (20), (21), and (22) are each grouped into 3-dimensional vectors, where the first dimension is for the number of streamlines, the second corresponds to the number of solution points along the streamline, and the third is for the initial angles in the range of θ. The position within the MOR domain is determined from a combination of the streamline number and solution point along the streamline. The growth rate curve in Figure 5a has been generated by evaluating the isotropic, strain rate independent growth rate given by equation (34) at each angle from horizontal in the range $\theta\epsilon[0,\pi]$ at a position 45 km below the ridge crest and 25 km from the ridge axis. The growth rate maximum has been identified in terms of θ, and that same value of θ has been noted in both the initial k_x and k_y spectra. The angle at which the band will then form fastest is given by $\arctan(k_x/k_y)$.

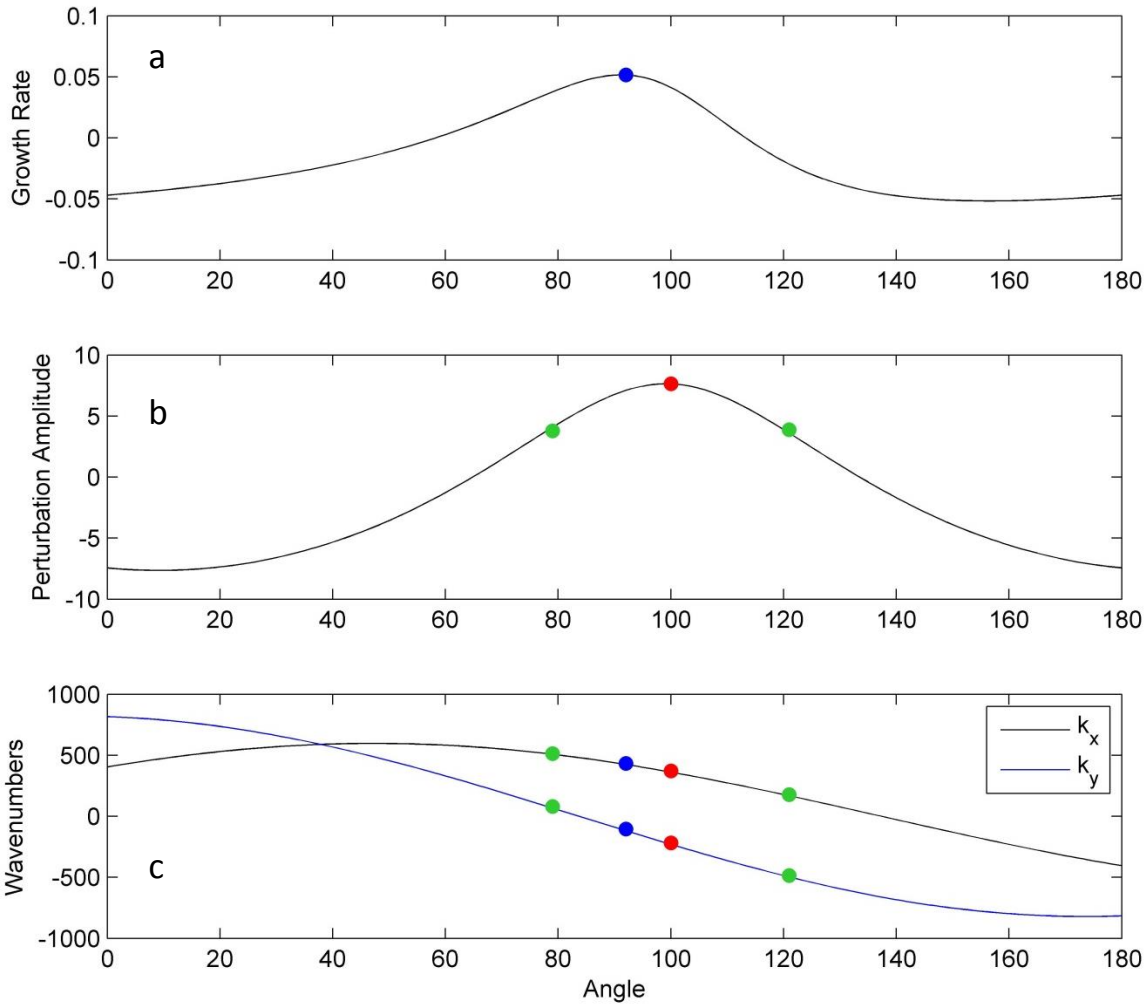

Figure 5: All panels come from 45 km below the ridge crest and 25 km from the ridge axis. a) Sample growth rate variation with angle from horizontal. The maximum value is indicated in blue. b) Perturbation amplitude variation with angle; here the maximum value is indicated in red, and the half-maximum amplitude envelope is indicated by green. c) Initial k_x and k_y spectra, with all the previous indicated significant values from the growth rate and amplitude plots also indicated. The orientation of the melt bands corresponding to the various desired maxima is determined from wavenumber spectra such as these.

Displaying the orientation of the bands that have undergone the greatest perturbation amplitude growth is similar. Figure 5b shows the perturbation amplitude spectrum for 45 km below the ridge crest and 25 km from the ridge axis, with the maximum value indicated in red. This same point is also indicated in the wavenumber spectra, giving the orientation of the most significant band at that location. In the case of the strain-rate dependant and anisotropic rheologies, two similar-magnitude peaks were often present in the perturbation amplitude spectra. At times, these two peaks became less sharp, occasionally even nearly merging into a single very broad maximum. To account for unexpected spectral width, a half-maximum

amplitude envelope was identified to indicate the occasional uncertainty in peak placement. This envelope is indicated in green in Figure 5b and 5c.

3.4 Nonlinear Simulation Overview

The primary goal of the nonlinear model is to investigate the full evolution in time of the governing equations for two-phase compacting media described by equations (11), (12), and (13). This model takes into account the same MOR-defined background flow present in the linear analysis, but also includes the nonlinear components of the strain acting on the partial melt system, the nonlinearities associated with advection, and those associated with the viscosity laws.

The governing equations are solved in a 2-dimensional square domain using Comsol Multiphysics where the length of each side of the domain is scaled by the compaction length. The centre of the square domain is centered on a streamline and its edges extend $n\delta_c$ in the both positive and negative x and y directions. For these simulations, $n = 2.5$ making the length of each edge $5\delta_c$. The position of the square domain within the larger MOR domain progresses in a manner similar to the linear analysis: the domain will initially begin at a depth of 70 km, and will progress up, along a streamline toward the base of the plate at the lithosphere-asthenosphere boundary. While the domain translates along a given streamline, a background velocity field is applied that corresponds to the linear gradient in the MOR velocity field. The model is set up so this process can be repeated along the same streamlines used for the linear analysis. An example of the translation of the square domain along a streamline is shown in Figure 6a.

The initial condition for the simulation is a random porosity field distribution defined by $\phi_0(x, y) = \Delta\phi \cdot Rn(x, y)$, where $Rn(x, y)$ is a two-dimensional white noise generator function predefined in Comsol. This initial porosity field is illustrated in Figure 6a. The boundary conditions on the square domain are periodic in both the x and y directions. Equations (11), (12), and (13) are solved using a finite element analysis scheme over a triangular mesh, as is shown in Figure 6b. The size of the mesh elements is controlled by Comsol, with the selected mesh being the second-most-fine option available so as to maximize resolution of melt band structures without greatly increasing the total model run time.

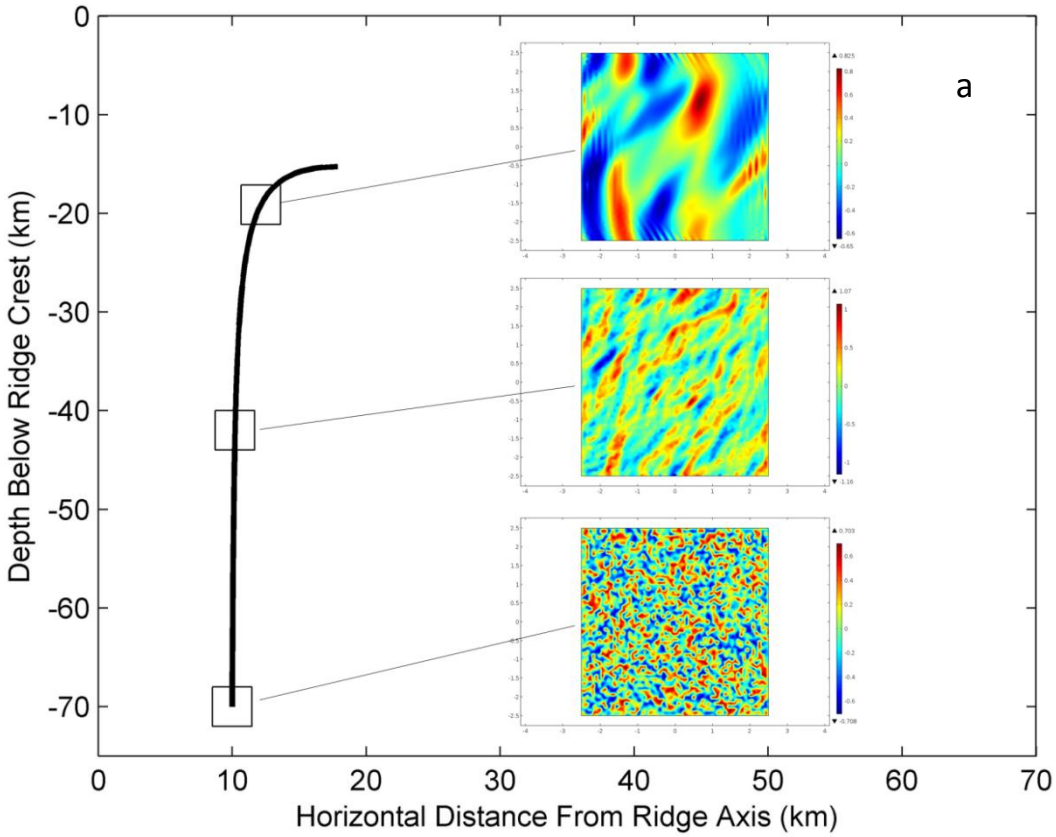

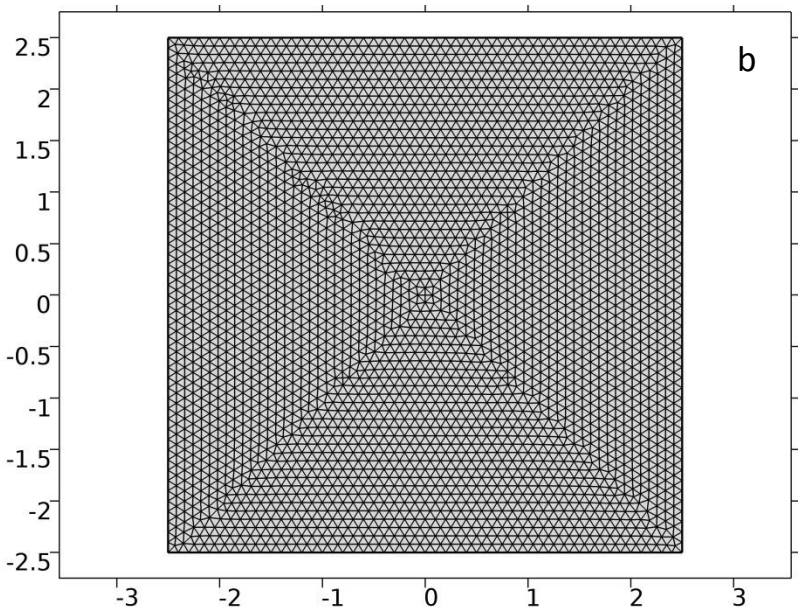

Figure 6: Sample simulation and mesh along 10km streamline. a) Example of melt band formation and evolution along the 10 km streamline of a slow-spreading ridge in the case of isotropic, strain rate independent rheology. The three magnified views correspond to the initial random porosity distribution (bottom), a mid-way view of the band formation clearly in progress (middle), and the final distribution of the porosity field at the termination of the model. b) Example of the extra-fine triangular mesh used in the finite element PDE solver.

Chapter 4: Results

The results for both the linear and nonlinear models are presented in this chapter, the linear analysis results being presented first, followed by a discussion of those results. Following that, the nonlinear results are shown and discussed. The discussion of the nonlinear results will include a comparison of the results from the two methods. A significant portion of the linear analysis results and discussion, including Figures 7, 10-12, and 16-18, have been previously published in *Geophysical Research Letters* by myself and my supervisor (Gebhardt and Butler, 2016).

4.1 Linear Analysis Results

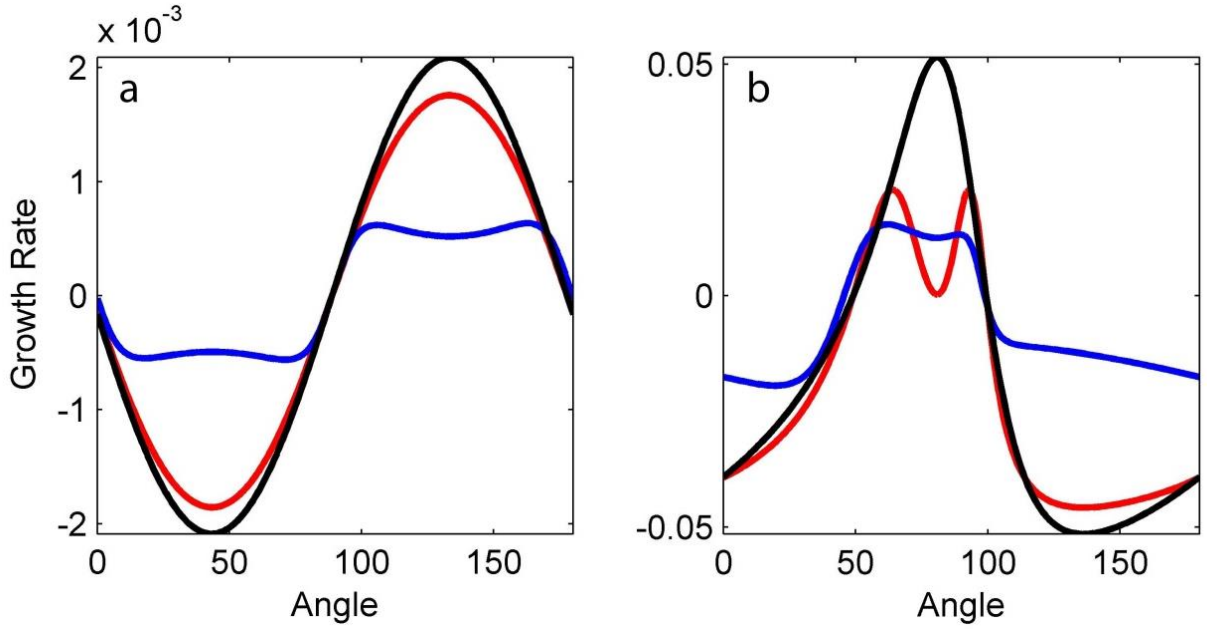

Figure 7: Growth rate variation with orientation for strain rate-independent (black), strain rate-dependent ($n_v = 6$, blue), and anisotropic (red) matrix shear viscosities. Panel (a) comes from 1 km from the ridge axis and (b) from 40 km from the ridge axis, both at a depth of 50 km. This figure was originally published by Gebhardt and Butler (2016).

Some unique influences of the three matrix rheologies are demonstrated in Figure 7. More than one growth rate maximum is known to occur in the case of strain rate dependent and anisotropic matrix rheologies (Katz et al., 2006, Butler, 2009, Takei and Katz, 2013). Figure 7 demonstrates a range in growth rate spectra behaviour for the case of anisotropic viscosity. This is attributed to the value of the anisotropy magnitude. In Figure 7a, taken from a position 1 km

from the ridge axis and a depth of 50 km, the anisotropic growth rate (red) behaves very similarly to the isotropic, strain-rate independent curve (black) due to a relatively low value of the anisotropy magnitude (α=0.29). Remaining at that depth but moving to 40 km from the ridge axis, the anisotropic growth rate in Figure 7b shows two maxima due to an increase in the anisotropy magnitude to α=1.99. A full range for the value of the anisotropy magnitude throughout the domain of a slow-spreading MOR can be seen in Figure 8. In addition to the change in behaviour of the anisotropic growth rate, an angular shift of approximately 50° is present in Figures 7a and 7b, resulting from the different flow geometries at the two locations. Finally, the growth rate magnitude is much greater in Figure 7b than in Figure 7a; this is attributed to greater strain at 40 km from the ridge axis.

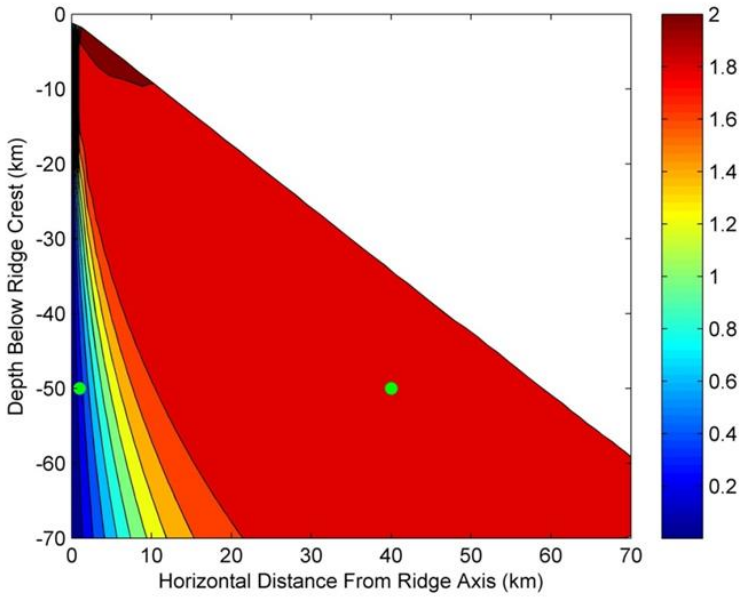

Figure 8: A contour plot of the variation in the anisotropy magnitude throughout the MOR domain where the locations of the growth rate spectra from Figure 7 are indicated in green.

In the case where more than one peak is present in the growth rate angular spectrum, the local maximum corresponding to the lower of the two angles is selected. The reason for this relates to the background vorticity of the MOR flow. As demonstrated in Figure 9, the background vorticity throughout the MOR domain is clockwise for both ridge geometries. Figures 9a and 9b show a very small magnitude for the local vorticity field throughout the MOR domain. However, Figures 9c and 9d show that the magnitude of the integrated vorticity is more significant, one to two orders of magnitude greater than the magnitude of the growth rate. This suggests that the cumulative effective clockwise rotation of the background flow would significantly influence band orientation, resulting in high angle bands being rotated over time to orientations corresponding to negative growth (decay). As noted by Gebhardt and Butler (2016), this justification for low-angle peak selection "is consistent with previous studies using simple

shear that have shown background flows quickly rotating high angle bands away from orientations with positive growth rates while low angle bands remain in favorable orientation for perturbation growth (Katz et al., 2006)."

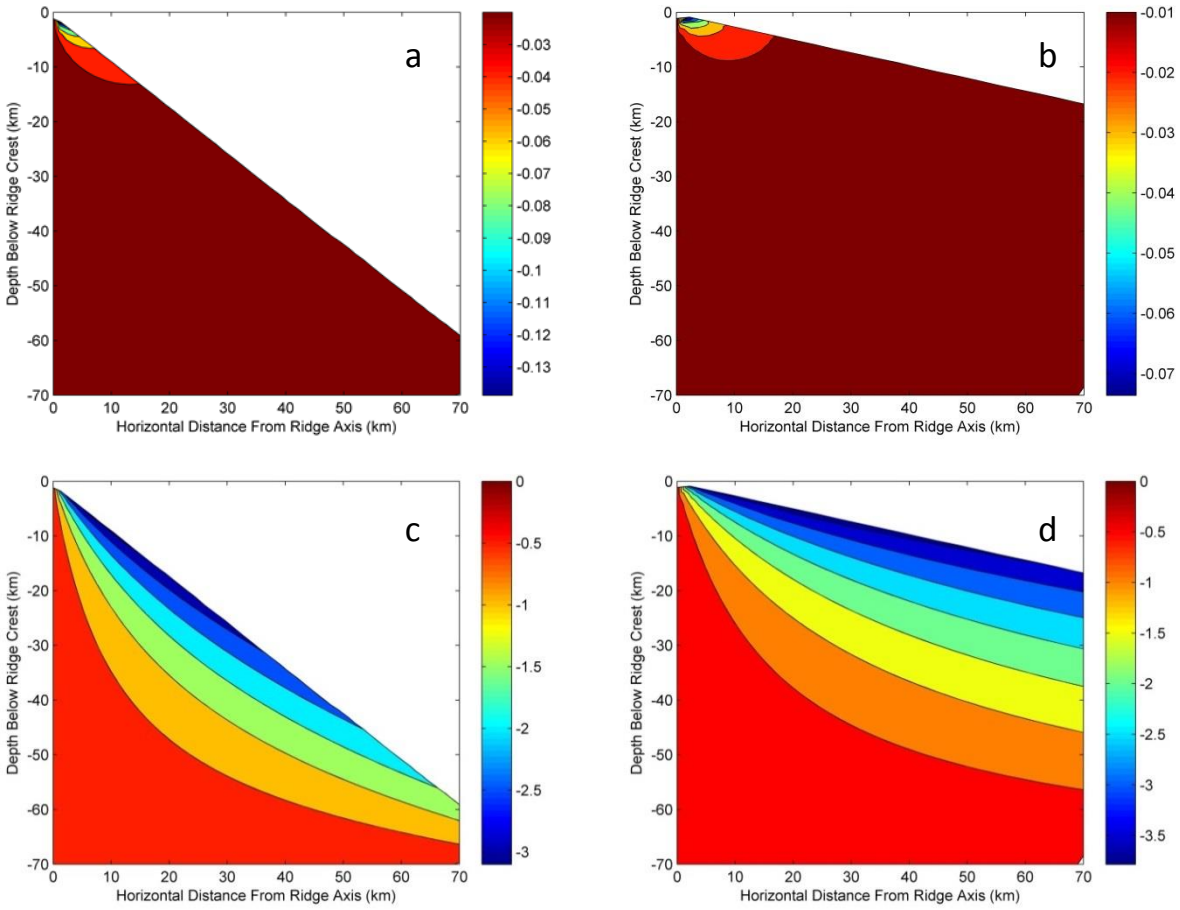

Figure 9: Vorticity variation in the MOR domain for slow spreading and fast spreading ridge geometries. Panels a) and b) show the local, instantaneous vorticity throughout the domain while panels c) and d) show vorticity integrated along streamlines. The negative magnitude in all four panels corresponds to a clockwise rotation.

Repeating the process of finding the maximum growth rate, maximum amplitude, and half-max amplitude envelope and finding the corresponding orientations leads to a great deal of data and the challenge of presenting those data in a clear manner. To accomplish this, the fastest growing bands and the maximally perturbed bands are plotted as short lines overlaying contour plots of the maximum growth rate and maximum perturbation amplitude, respectively. The band-lines are inclined at the orientation appropriate for their position in the MOR domain. In the case of strain-rate dependent and anisotropic viscosity perturbation amplitude, multiple orientations

for the maximum perturbation amplitude are shown on the plots when the magnitude of a second distinct maximum is within 10% of the greatest perturbation amplitude.

The contours for the maximum perturbation amplitude are saturated at a maximum value of $s_{max} = 6.8977$. This value is motivated by both the fixed initial porosity of 1% used in this analysis, along with the range of acceptable porosities in the mantle. Porosity in the mantle ranges between [0,0.3], where 0.3 corresponds to the rheologically critical melt fraction (RCMF), the point at which contiguity between grains is lost (Scott and Kohlstedt, 2006). To ensure the local porosity remains above 0, a maximum value for the perturbation amplitude can be expressed as $s_{max} = \ln\left(\frac{\phi_0}{\Delta\phi}\right)$. This is determined by from equation (19) be setting $\phi = 0$ and the oscillatory part of the exponential to -1. A similar expression can be derived for the RCMF porosity limit, but the small ϕ_0 used in this analysis makes the lower bound a greater concern. As noted by Gebhardt and Butler (2016), a lack of constraint on $\Delta\phi$ results in variability in the value of s_{max}. For example, when $\Delta\phi = 0.1\phi_0$, $s_{max} = 6.8977$, as is shown in Figures 16 through 21. However, for $\Delta\phi = 0.0001\phi_0$, $s_{max} = 9.2103$.

The results of the orientations for the fastest growing bands are shown in Figures 10 through 15. Looking at these six figures, it is clear that in the case of isotropic, strain rate dependent and anisotropic, strain rate independent rheologies, there are regions within the MOR domain that produce fast growing bands that are oriented toward the ridge axis. This is the case for both slow and fast spreading ridges, as demonstrated in Figures 11, 12, 14, and 15. The same cannot be said in the case of isotropic, strain rate independent rheology. Figures 10 and 13 clearly show that the fast growing bands are generally more preferably oriented toward the base of the plate at the lithosphere-asthenosphere boundary.

The band orientations demonstrated in Figures 10 and 13 are parallel to the directions of maximum compression (shown with black lines in Figure 4). The strain rate dependent bands of Figures 11 and 14 form at consistently low angles to the direction of maximum compression, while the anisotropic bands in Figures 12 and 15 clearly demonstrate a range in behavior consistent with the range in the value of the magnitude of the anisotropy. Near the ridge axis, the anisotropic band orientations closely resemble those of the strain-rate independent case, while further from the ridge axis the bands gradually form at low angles to the direction of maximum compression. The band orientations for the strain rate dependent rheology are consistent with the results from the work by Katz et al. (2006).

The contour plots in Figures 16 through 21 show the maximum perturbation amplitude throughout the MOR domain. Slow spreading ridge geometry results are given in Figures 16 to18 while the fast spreading ridge results are shown in Figures 19 to 21. Where only a single orientation is given, the second peak has been absorbed into the first leading to a very broad single peak. As mentioned previously, the half-maximum envelope is indicated by the green bars in all of these figures "to demonstrate the potential angular range of both the very broad single peaks and the multiple peaks present" (Gebhardt and Butler, 2016). In all six of these figures, it is clear that the bands are oriented toward the base of the plate at the lithosphere-asthenosphere boundary.

Comparing the corresponding viscosity cases in the set of growth rate and perturbation amplitude figures, it is clear that the fastest growing band orientations are not preserved in time. Instead, these bands undergo clockwise rotation to the orientations corresponding to the evolved bands with the largest perturbation amplitude. The extent of the band rotation depends on the relative sizes of the background vorticity and growth rate of the perturbation. The results shown in Figures16 through 21 therefore demonstrate the significant influence caused by the background flow of the MOR: "the maximally perturbed bands for all three rheologies have been rotated by the background flow away from the maximum growth rate orientation, resulting in bands directed toward the base of the plate at the lithosphere-asthenosphere boundary" (Gebhardt and Butler, 2016). This clockwise rotation away from the direction of fastest growth experienced by the evolved bands is present in both the slow spreading and fast spreading ridge geometries.

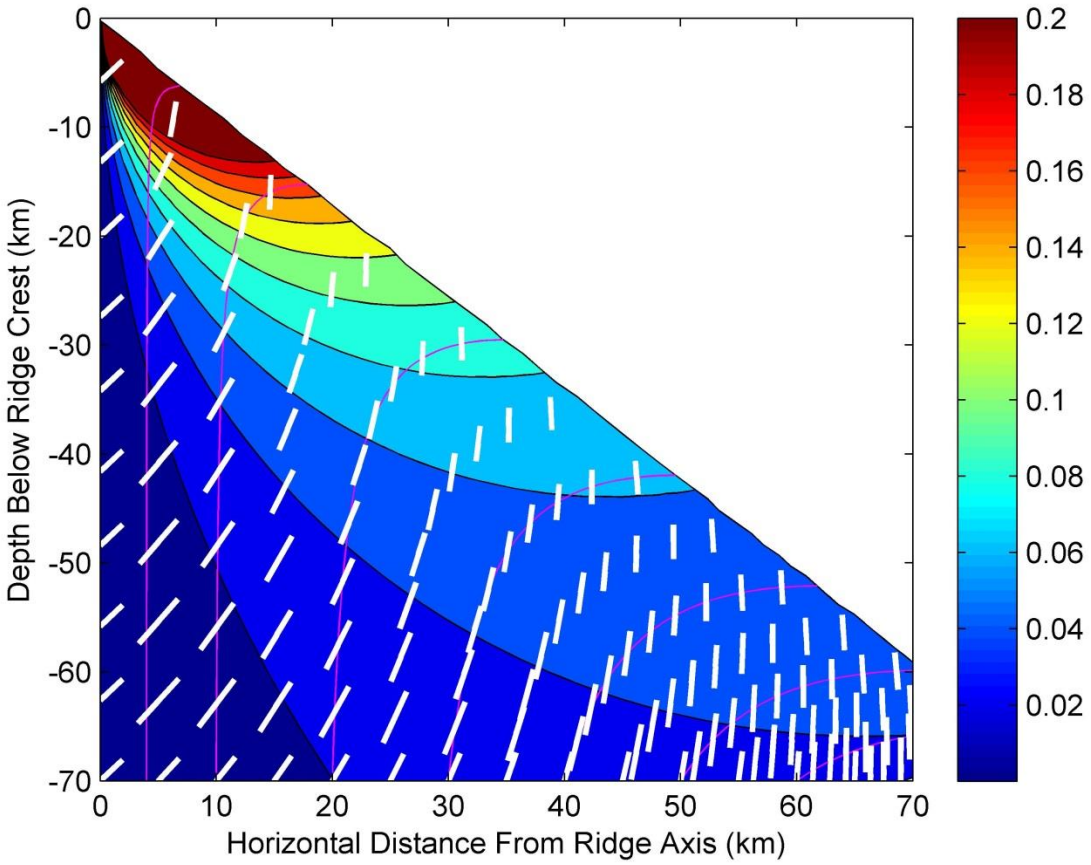

Figure 10: Contour plot of maximum instantaneous growth rate for a slow spreading ridge with isotropic strain-rate independent rheology. Band orientation is indicated by the overlain white lines. These lines indicate orientation only. Bands in this case are oriented toward the lithosphere-asthenosphere boundary. All linear analysis figures for the slow spreading ridge geometry were originally published by Gebhardt and Butler (2016).

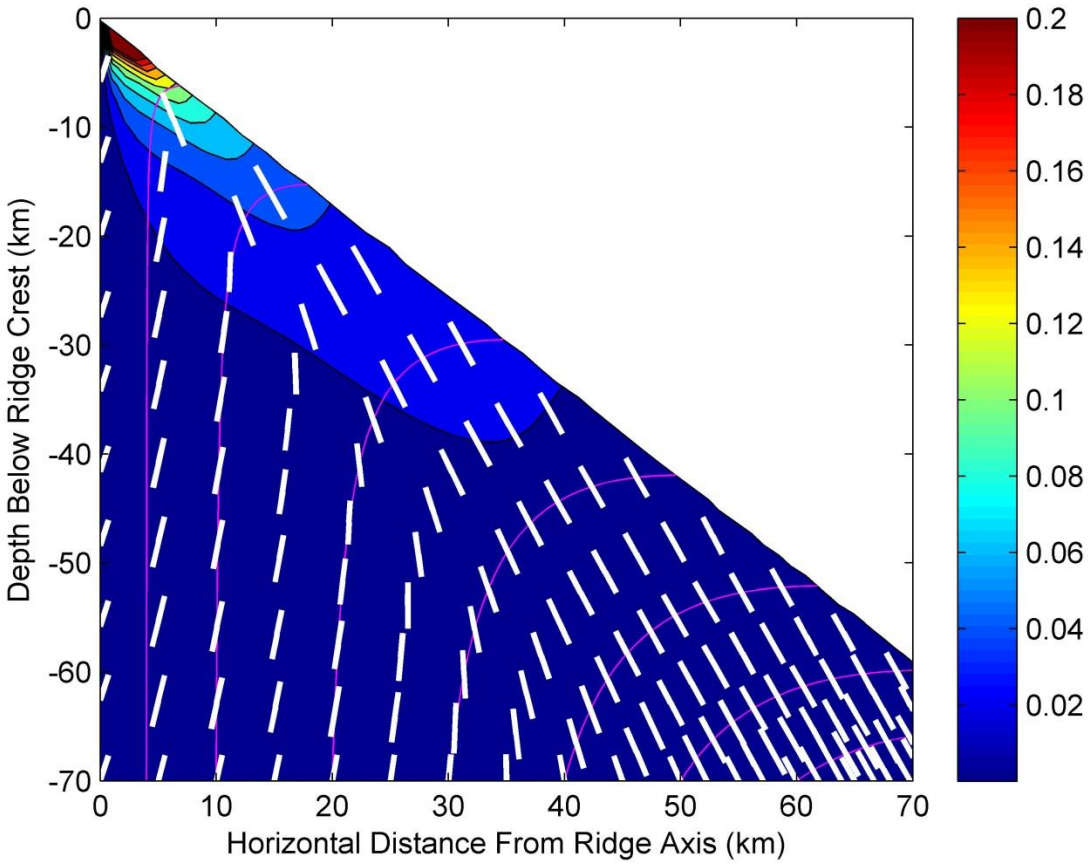

Figure 11: Contour plot of maximum instantaneous growth rate for a slow spreading ridge with isotropic, strain rate dependent ($n_v = 6$) rheology. Under these circumstances, band orientations are consistently at low angles to the direction of maximum compression resulting in regions where bands are oriented toward the ridge axis.

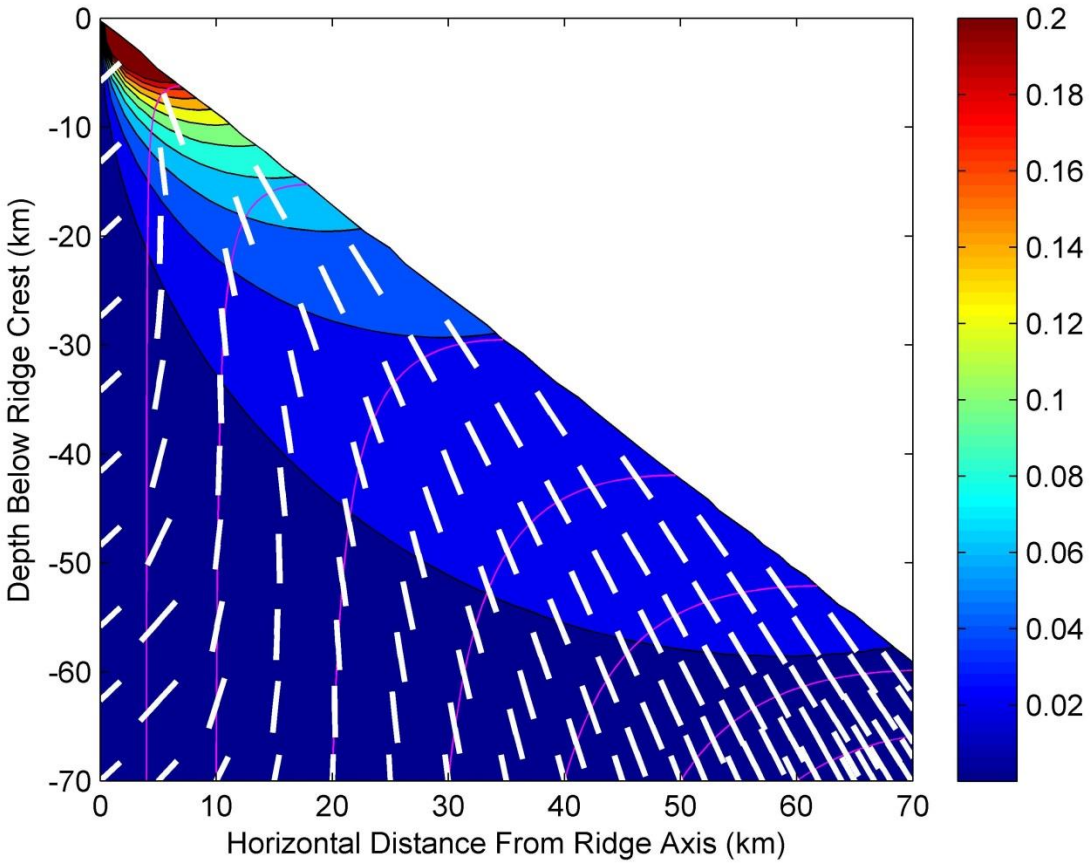

Figure 12: Contour plot of maximum instantaneous growth rate for a slow spreading ridge with anisotropic, strain-rate independent matrix rheology. These bands are also oriented toward the ridge axis in some regions. However, these bands do not form at consistently low angles to the direction of maximum compression. This is attributed to the range in anisotropy magnitude throughout the MOR domain.

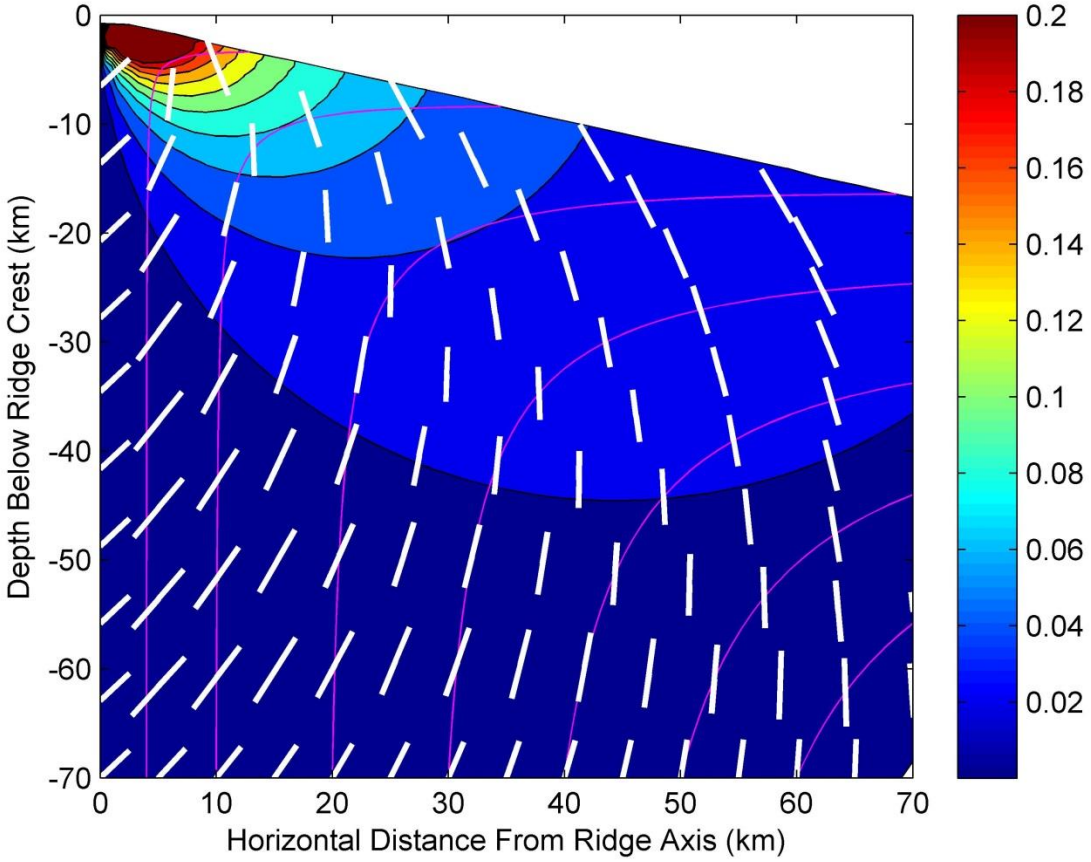

Figure 13: Contour plot of maximum instantaneous growth rate for a fast spreading ridge with isotropic, strain rate independent matrix rheology. These bands are again oriented toward the base of the plate at angles parallel to the directions of maximum compression.

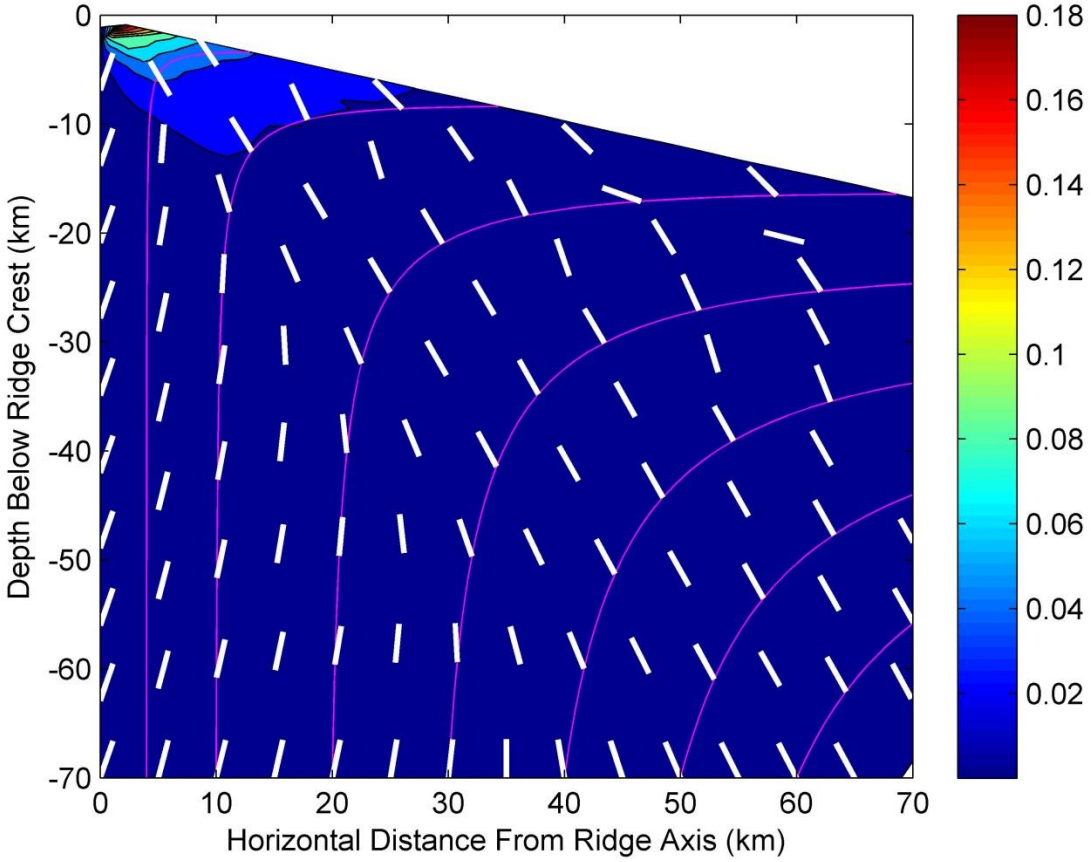

Figure 14: Contour plot of maximum instantaneous growth rate for a fast spreading ridge with isotropic, strain rate dependent ($n_v = 6$) rheology. As with its slow spreading counterpart, this viscosity condition results in band orientations that are consistently at low angles to the direction of maximum compression leading to regions where bands are oriented toward the ridge axis.

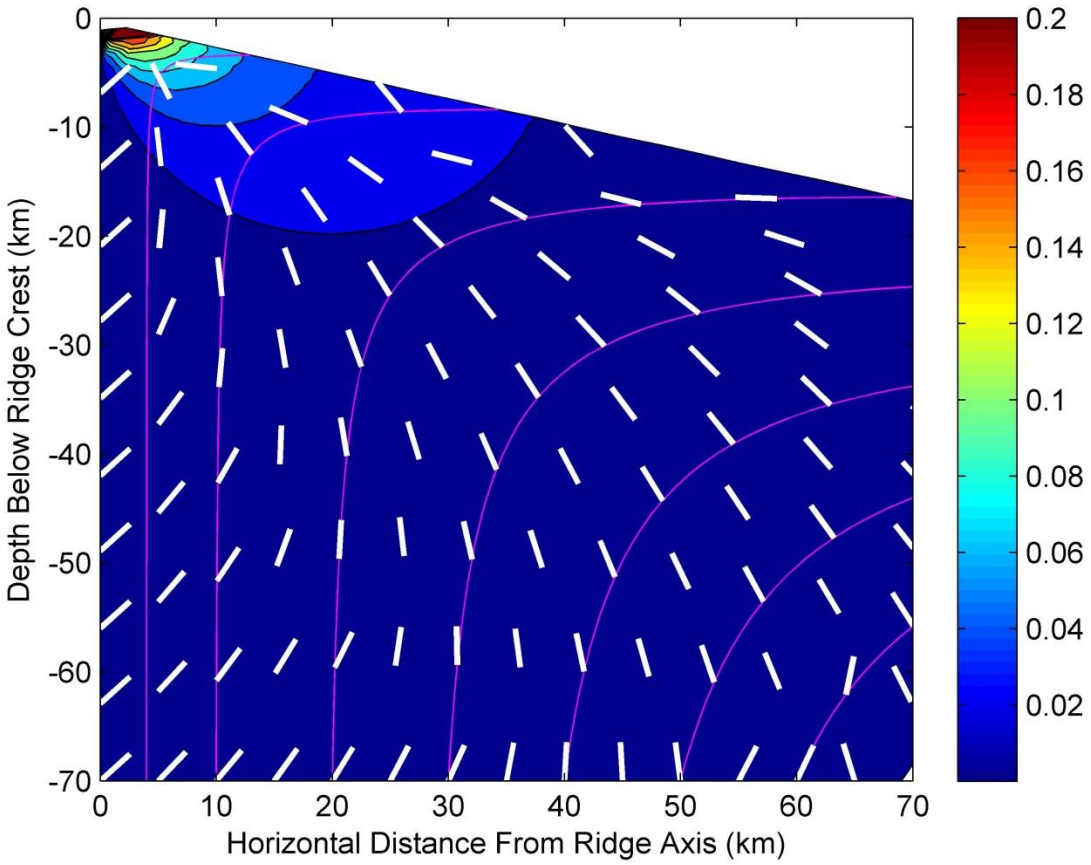

Figure 15: Contour plot of maximum instantaneous growth rate for a fast spreading ridge with anisotropic, strain-rate independent matrix rheology. These bands are also oriented toward the ridge axis in some regions. The variation in band orientation relative to the direction of maximum compression is again attributed to the variation in the value of the anisotropy magnitude.

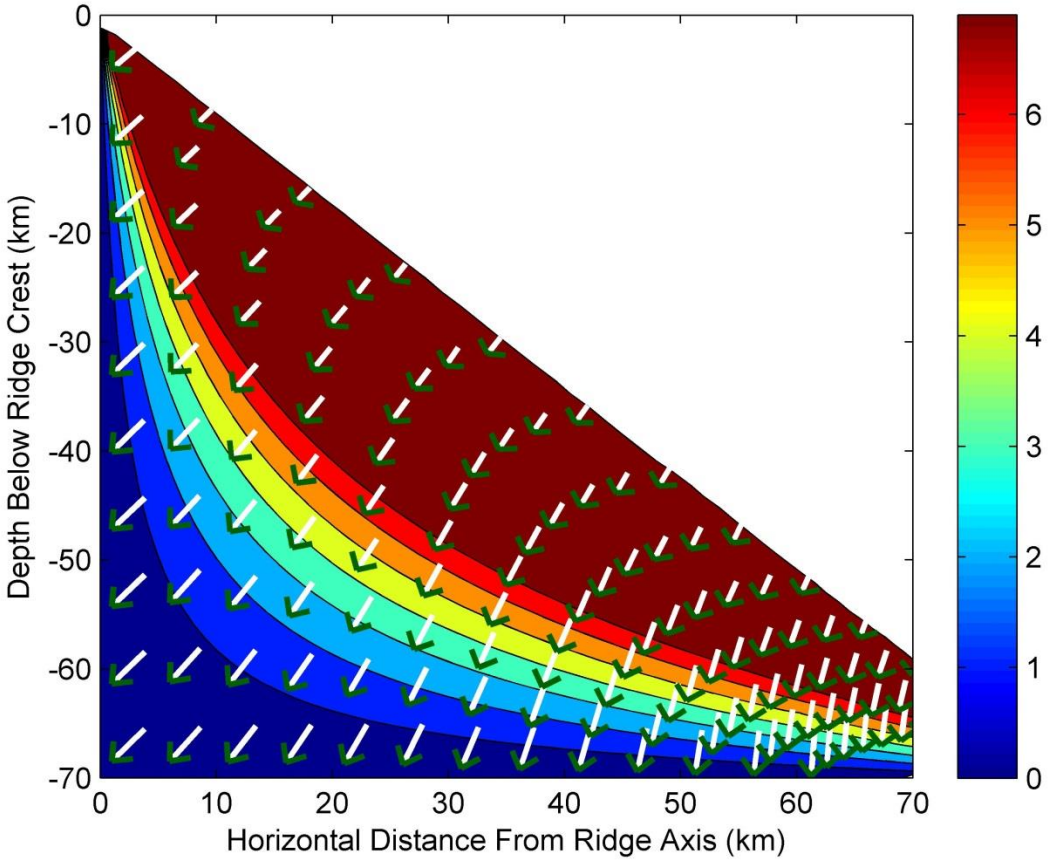

Figure 16: Contour plots of maximum perturbation amplitude for a slow spreading ridge with isotropic, strain rate independent rheology. In this case, the bands have been rotated by the background flow into a more direct orientation toward the base of the plate. A limit for s_{max} in the case where $\Delta\phi = 0.1\phi_0$ has been imposed on all amplitude contour plots. Here this results in significant regions of MOR domain exceeding the limit of s_{max} resulting in unphysical porosities, thereby invalidating the linear analysis in those regions.

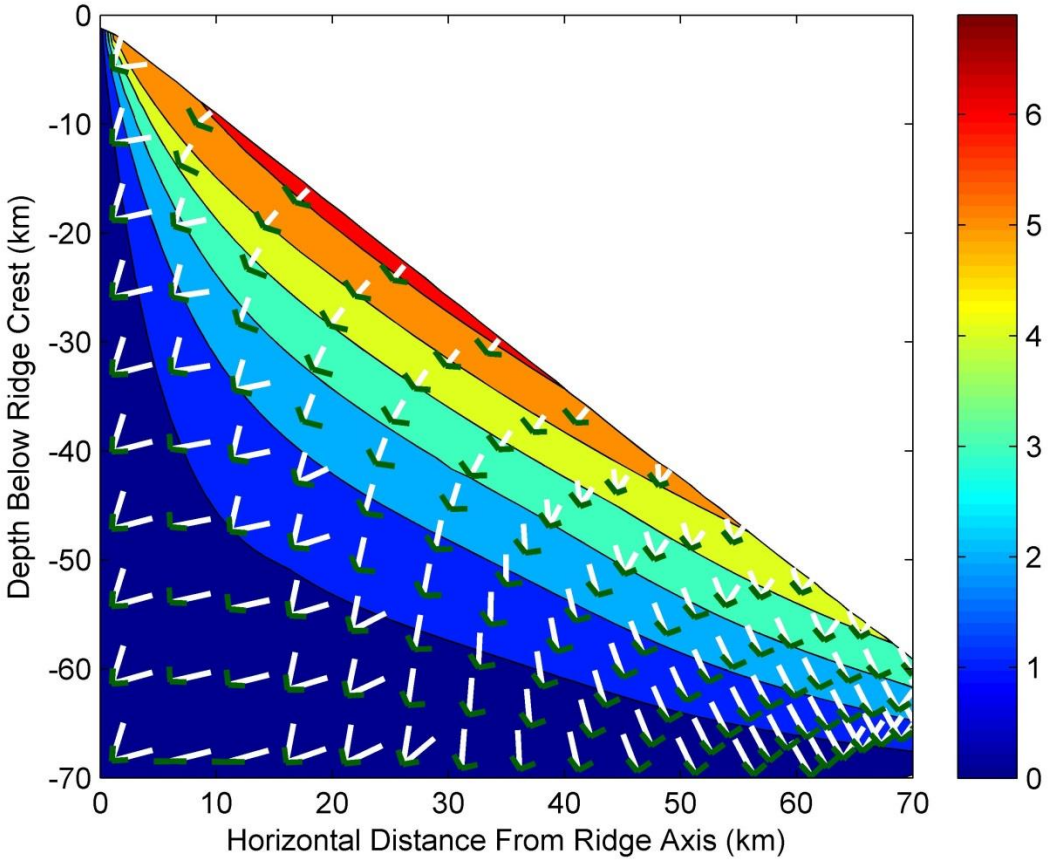

Figure 17: Contour plots of maximum perturbation amplitude for a slow spreading ridge with isotropic, strain rate dependent ($n_v = 6$) rheology. Here a significantly smaller region of the MOR domain exceeds the limit of s_{max}. Bands have again been rotated by the background flow to be oriented more directly at the lithosphere-asthenosphere boundary.

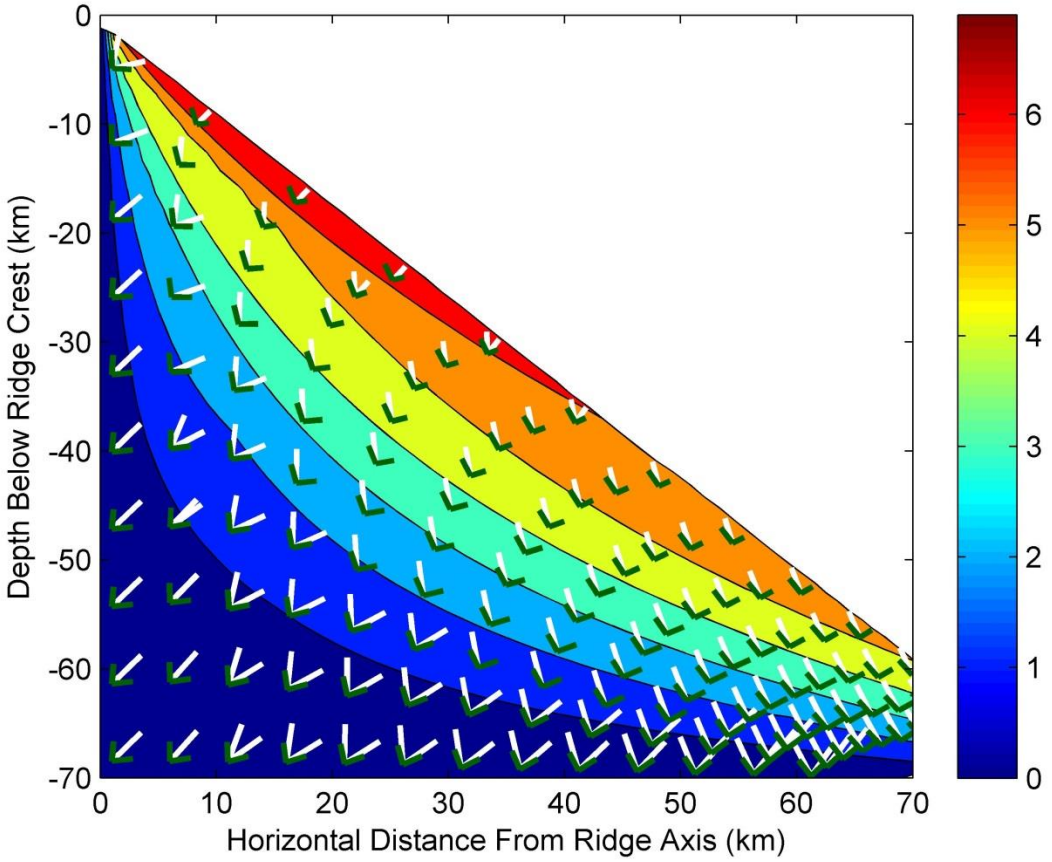

Figure 18: Contour plots of maximum perturbation amplitude for a slow spreading ridge with anisotropic, strain rate independent rheology. Again, a significantly smaller region of the MOR domain exceeds the limit of s_{max} and bands have again been rotated by the background flow to be oriented more directly at the lithosphere-asthenosphere boundary.

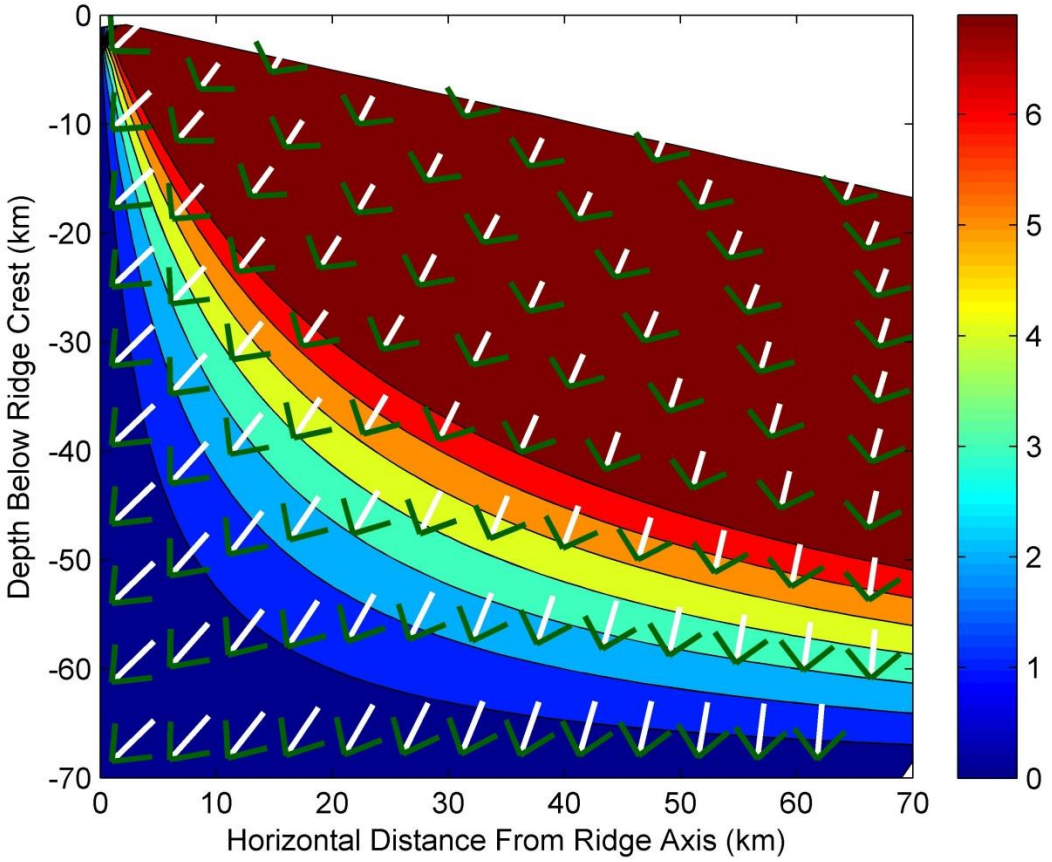

Figure 19: Contour plots of maximum perturbation amplitude for a fast spreading ridge with isotropic, strain rate independent rheology. As with its slow spreading counterpart, the bands have been rotated by the background flow into a more direct orientation toward the base of the plate. A very significant portion of the MOR domain exceeds the limit of s_{max}.

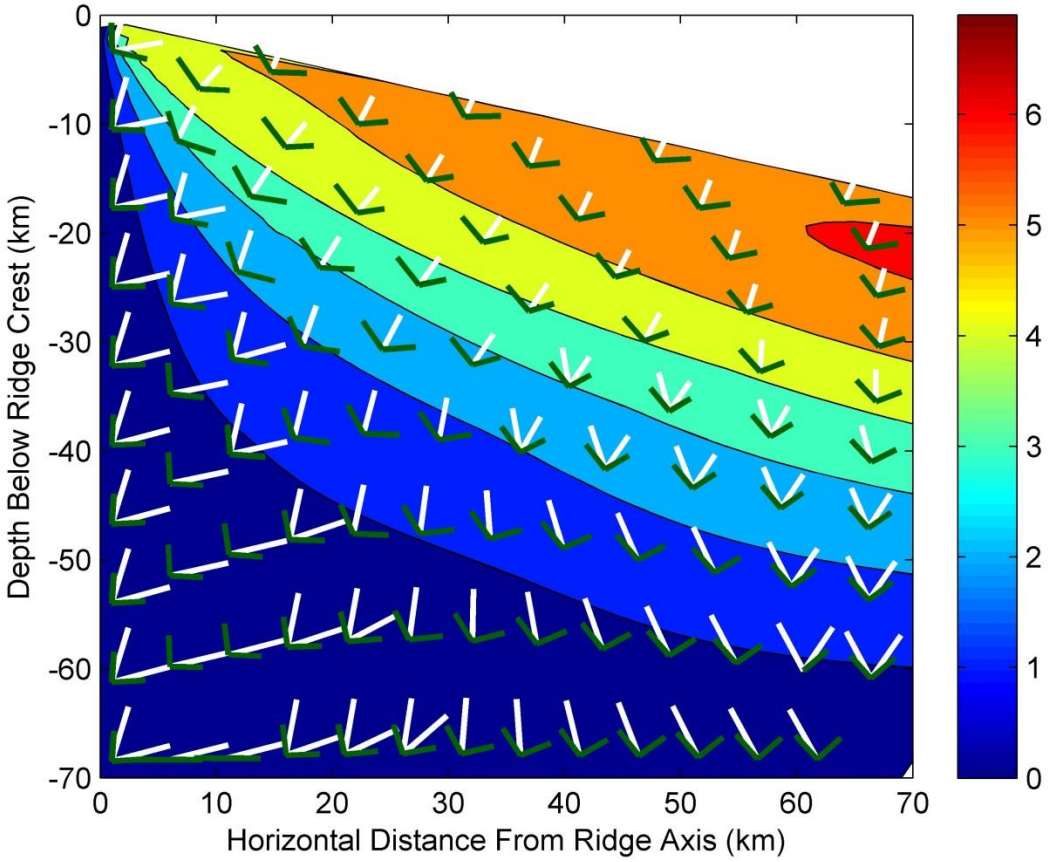

Figure 20: Contour plots of maximum perturbation amplitude for a fast spreading ridge with isotropic, strain rate dependent ($n_v = 6$) rheology. Bands have again been rotated by the background flow to be oriented more directly at the lithosphere-asthenosphere boundary. Here almost nowhere in the MOR domain exceeds the limit of s_{max}, except for a small region below the base of the plate.

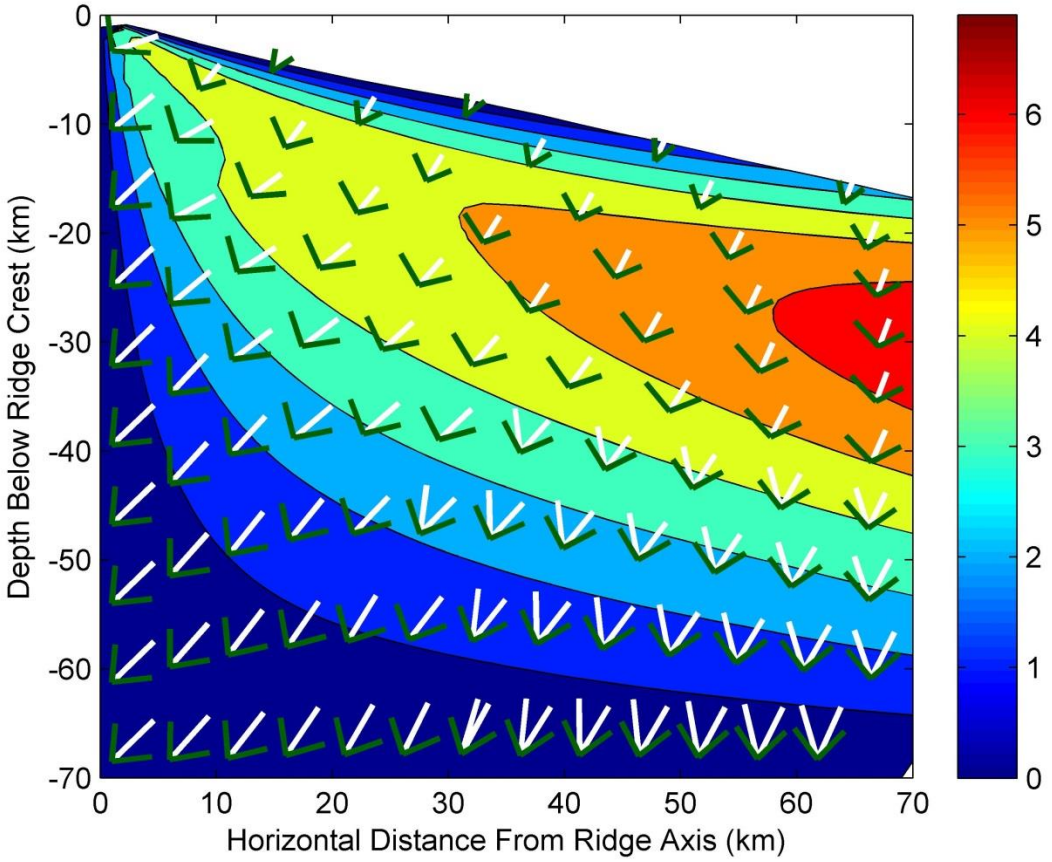

Figure 21: Contour plots of maximum perturbation amplitude for a fast spreading ridge with anisotropic, strain rate independent rheology. As is the case with all the other perturbation amplitude plots, bands have again been rotated by the background flow to be oriented more directly at the lithosphere-asthenosphere boundary. Here, only a relatively small region of the MOR domain exceeds the limit of s_{max}, though this region is at a depth below the base of the plate.

4.2 Linear Analysis Results Discussion

As noted by Gebhardt and Butler (2016), this linear analysis is strictly only valid for small variations from the initial porosity, $\phi_0 = 0.01$. Further limitations come in the form of two poorly defined variables: the initial perturbation amplitude, $\Delta\phi$, and the matrix bulk viscosity. The size of the color-saturated regions in slow and fast spreading ridge geometries (Figures 16 and 19) demonstrates that Newtonian rheology results in significant regions of the MOR domain that exceed the maximum allowed perturbation amplitude. However, both the non-Newtonian (Figures 17 and 20) and anisotropic (Figures 18 and 21) rheologies present perturbation amplitudes that are valid for larger portions of the MOR domain, for both ridge geometries.

The following discussion of the results regarding the linear analysis for the slow spreading ridge geometry was originally published by Gebhardt and Butler (2016) in *Geophysical Research Letters*:

> The lack of constraint on $\Delta\phi$ also affects predictions for the variation in permeability throughout the MOR domain. The region with the highest permeability variation is generally located along the lithosphere-asthenosphere boundary, though the vertical extent of this region is variable. The permeability range decreases with decreasing $\Delta\phi$, and therefore decreasing the range in permeability would result in less effective channeling through the bands. When $\Delta\phi = 0.1\phi_0$, the permeability increases by a factor of 10^4 from the starting depth to the base of the plate, with large increases in permeability already present at depths of around 30km below the base of the plate. For $\Delta\phi = 0.0001\phi_0$, the permeability varies by only a factor of 10^{-2} in the whole MOR domain and the highest permeability is confined right along the base of the plate. Therefore for the small values of $\Delta\phi$ required to make all the cases of the linear analysis presented here valid, channeling through bands would likely only be effective very close to the base of the plate, although effective channeling could occur at a greater depth for the strain-rate dependent and anisotropic viscosity bands due to the range in acceptable values of $\Delta\phi$.
>
> The presented results use a bulk viscosity that is 5/3 the shear viscosity (Takei and Katz, 2013). The analysis was repeated with an increased bulk viscosity of 200, consistent with other theoretical models where the bulk viscosity varies inversely with porosity (Bercovici and Ricard, 2003). This increase resulted in a decrease in magnitude for both the growth rate and perturbation amplitude with little effect on orientation for all viscosity cases. Increasing the bulk viscosity also results in a significant decrease in the range of permeability. When $\Delta\phi = 0.1\phi_0$, the permeability increases by only a factor of 10^{-2} while for $\Delta\phi = 0.0001\phi_0$, the permeability varies by a factor of 10^{-5}. The significance of the melt bands both in terms of amplitude and channeling ability is therefore greatly reduced in the presence of a greatly increased bulk viscosity.

Alternate perturbation amplitude results were also considered. In addition to looking for the orientations corresponding to the maximally perturbed porosity bands at a given location in

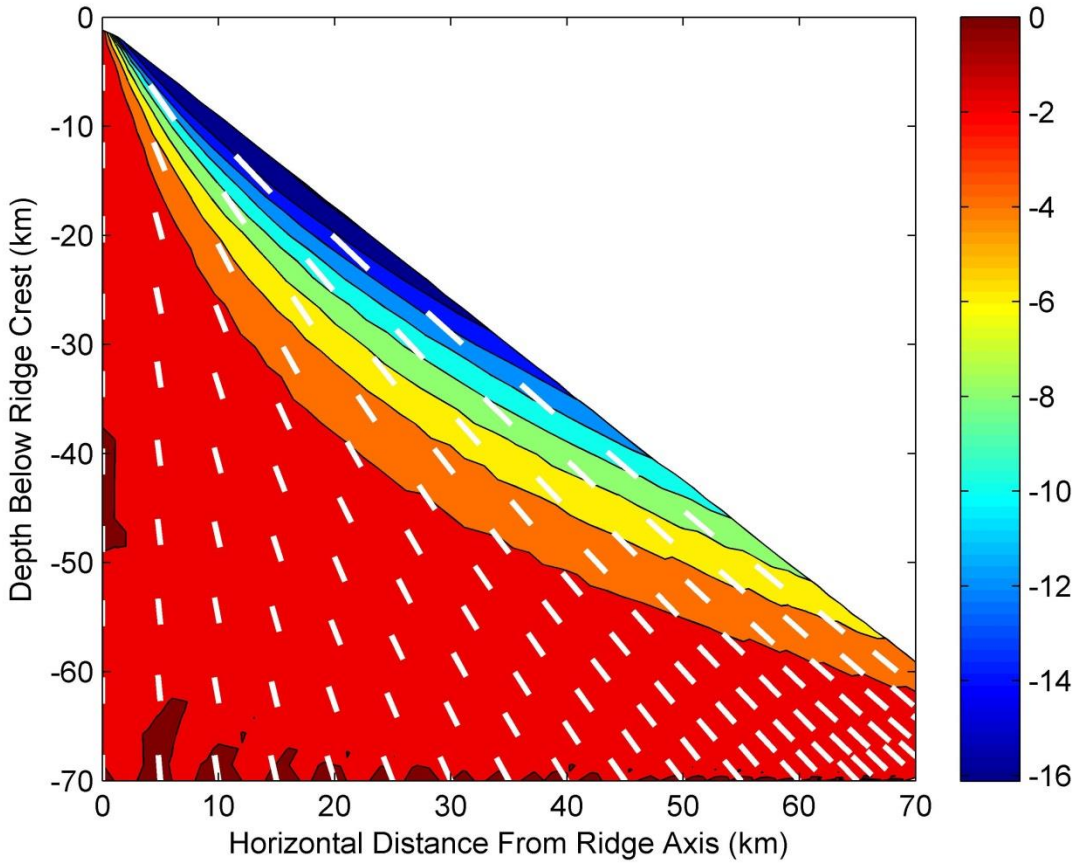

Figure 22: Contour plot of perturbation amplitude for bands evolved for preferential orientation toward the ridge axis for the case of a slow spreading ridge geometry with an isotropic, strain rate independent matrix rheology. Note that the negative amplitude for all the contours indicates that the bands in these orientations decay instead of grow.

the MOR domain, perturbation evolution that resulted in bands oriented directly toward the ridge axis was also considered. The result of this evolution in the case of isotropic, strain rate independent rheology is shown in Figure 22. The negative amplitude present throughout the entire MOR domain in Figure 22 indicates that bands in these orientations decay rather than grow. This was found to be the case for all three viscosity conditions for both slow and fast spreading ridge geometries. These results from the other viscosity cases can be found in Appendix 7.

4.3 Nonlinear Simulation Results

Figures 23 through 26 contain sections from the nonlinear Comsol models. The panels in each figure were generated by running the model along the 15 km, 30 km, and 60 km corner flow streamlines. In these figures, the bottom row of panels corresponds to positions along respective streamlines where porosity localization starts to become apparent, while the middle row of panels shows the progression of melt band formation at a midway point along the streamline. Finally, the top row of panels shows the state of the bands at either the termination point of the model or the intersection of the streamlines with the base of the plate, whichever comes first. Only along the 60 km streamline for slow spreading ridge geometry did the model reach the lithosphere-asthenosphere boundary.

No end condition exists in the nonlinear models to force the termination of the simulations. Instead, models terminate when they fail. Failure is related to the porosity becoming essentially 0 somewhere in the model domain. This leads to a lack of constraint on the liquid pressure in the system since the porosity and permeability terms in equation (3) – the Darcy law force balance for the melt phase – both go to 0. Subsequently, neighboring values of the liquid pressure can take on values that exceed the relative tolerance of the model.

The band growth shown in Figures 23 to 26 is very similar. Porosity localization into band-like structures begins early in simulations with the size of bands growing substantially by around the midpoint of the model run times. By the termination of the models, significant band-like structures are present, along with a significant amount of numerical instability along the boundaries. In some cases, the magnitude of the noise at the end of simulations is much greater than the magnitude in the bands that the bands are no longer visible. In Figure 27, the

termination of the 55 km streamline is shown with the automatic color range in the top panel where no bands are visible, while the bottom panel uses a manual color range making band-like structures visible. This sort of noise-dominant behaviour is especially evident at streamlines far from the ridge axis. In the case of slow spreading ridge geometry, the visibility of bands at the termination of the models is significantly reduced starting at streamlines located around 32 km from the ridge axis, while for fast spreading geometry reduced end-state visibility begins around the 22 km streamline.

Figures 23 and 24 show the result of models run with isotropic, strain rate independent matrix viscosity while Figures 25 and 26 come from models run with isotropic, strain rate dependent rheology. When the anisotropic models were run, the high magnitude noise was dominant throughout the simulations. This resulted in no discernible significant band formation. For this reason, the nonlinear anisotropic model results are not included here and instead are presented in Appendix 6.

A mesh-refinement error analysis was performed on the nonlinear simulations. Increasing the mesh size did not significantly change the model results as band orientations and porosity magnitudes were similar. The only noticeable difference in the models with different mesh sizes was the resolution of the bands, where smaller meshes resulted in more precisely defined band structures.

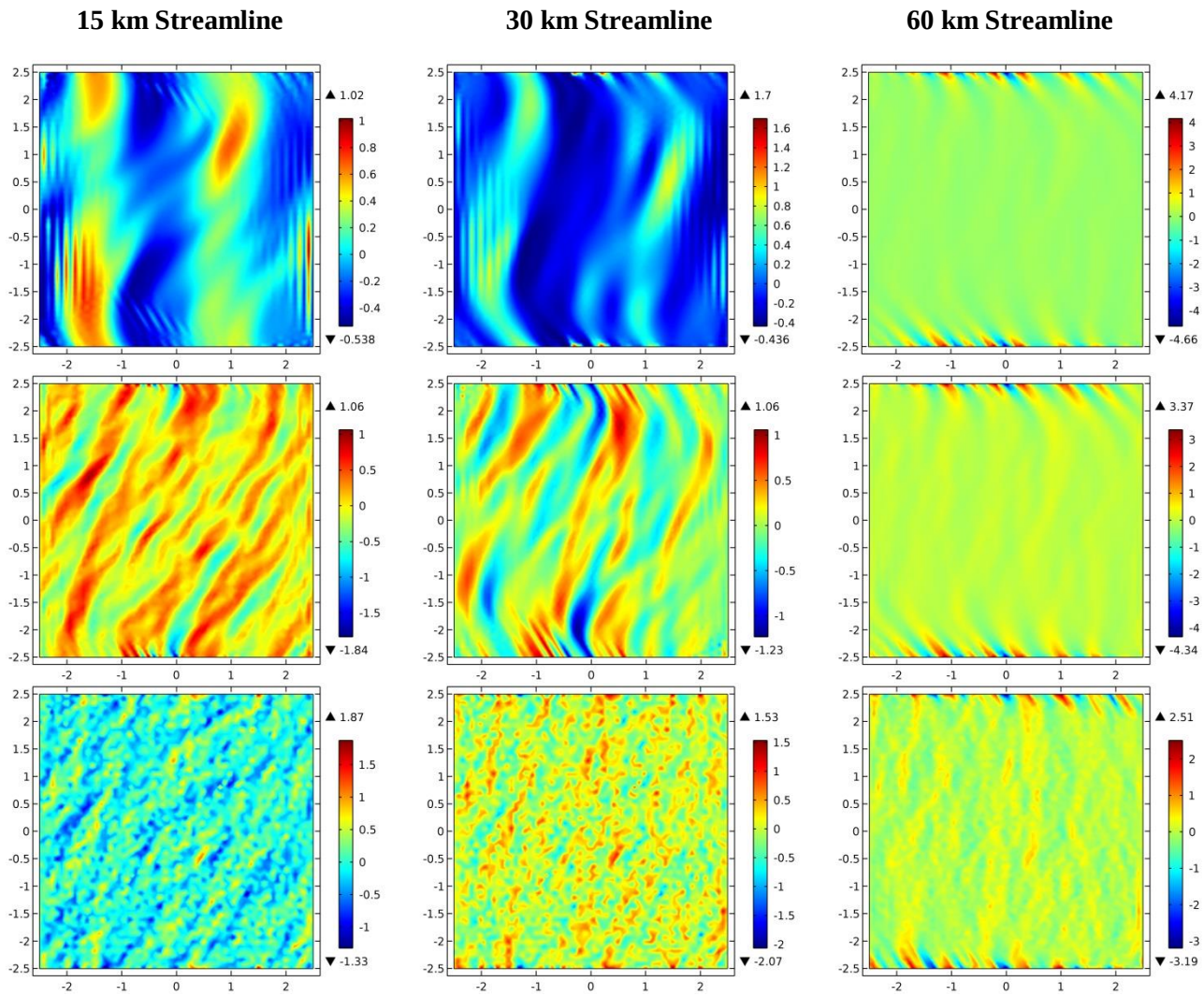

Figure 23: Nonlinear melt band evolution along multiple streamlines in the case of isotropic, strain rate independent matrix rheology and slow spreading ridge geometry. The lowest row corresponds to the greatest depth along the streamlines, the middle row a midway look at the band formation and the top row the location where the model terminated or reached the base of the plate at the lithosphere-asthenosphere boundary. From the 15 km streamline, the panels come from 15.2 km from ridge axis and 59.3 km below the ridge crest (bottom), 15.8 km from ridge axis and 42.1 km below the ridge crest (middle), and 19.6 km from ridge axis and 25.3 km below the ridge crest (top). For the 30 km streamline, the panels come from 30.4 km from ridge axis and 66.0 km below the ridge crest (bottom), 34.1 km from ridge axis and 50.8 km below the ridge crest (middle), and 44.6km from ridge axis and 42.4 km below the ridge crest (top). Finally, for the 60 km streamline, the panels come from 63.8 km from ridge axis and 66.8 km below the ridge crest (bottom), 73.2 km from ridge axis and 65.4 km below the ridge crest (middle), and 77.5km from ridge axis and 65.3km below the ridge crest (top). The top panel of the 60 km streamline is located at the base of the plate.

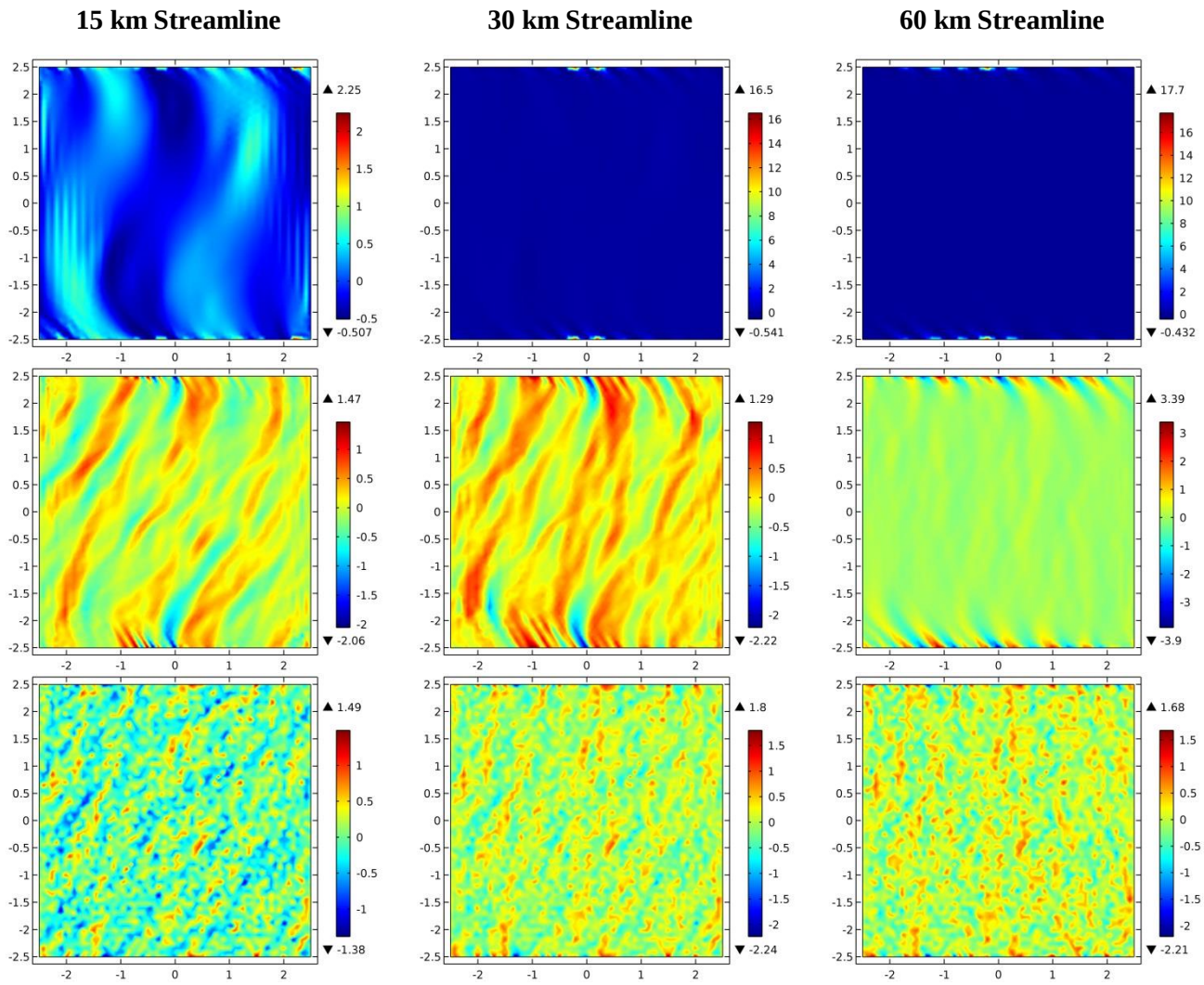

Figure 24: Nonlinear melt band evolution along multiple streamlines in the case of isotropic, strain rate independent matrix rheology and fast spreading ridge geometry. From the 15 km streamline, the panels come from 15.1 km from ridge axis and 57.4 km below the ridge crest (bottom), 16.2 km from ridge axis and 30.2 km below the ridge crest (middle), and 21.9 km from ridge axis and 16.2 km below the ridge crest (top). For the 30 km streamline, the panels come from 30.5 km from ridge axis and 62.2 km below the ridge crest (bottom), 33.2 km from ridge axis and 44.3 km below the ridge crest (middle), and 43.3 km from ridge axis and 30.1 km below the ridge crest (top). Finally, for the 60 km streamline, the panels come from 61.3 km from ridge axis and 67.1 km below the ridge crest (bottom), 69.2 km from ridge axis and 56.5 km below the ridge crest (middle), and 85.0 km from ridge axis and 48.2 km below the ridge crest (top).

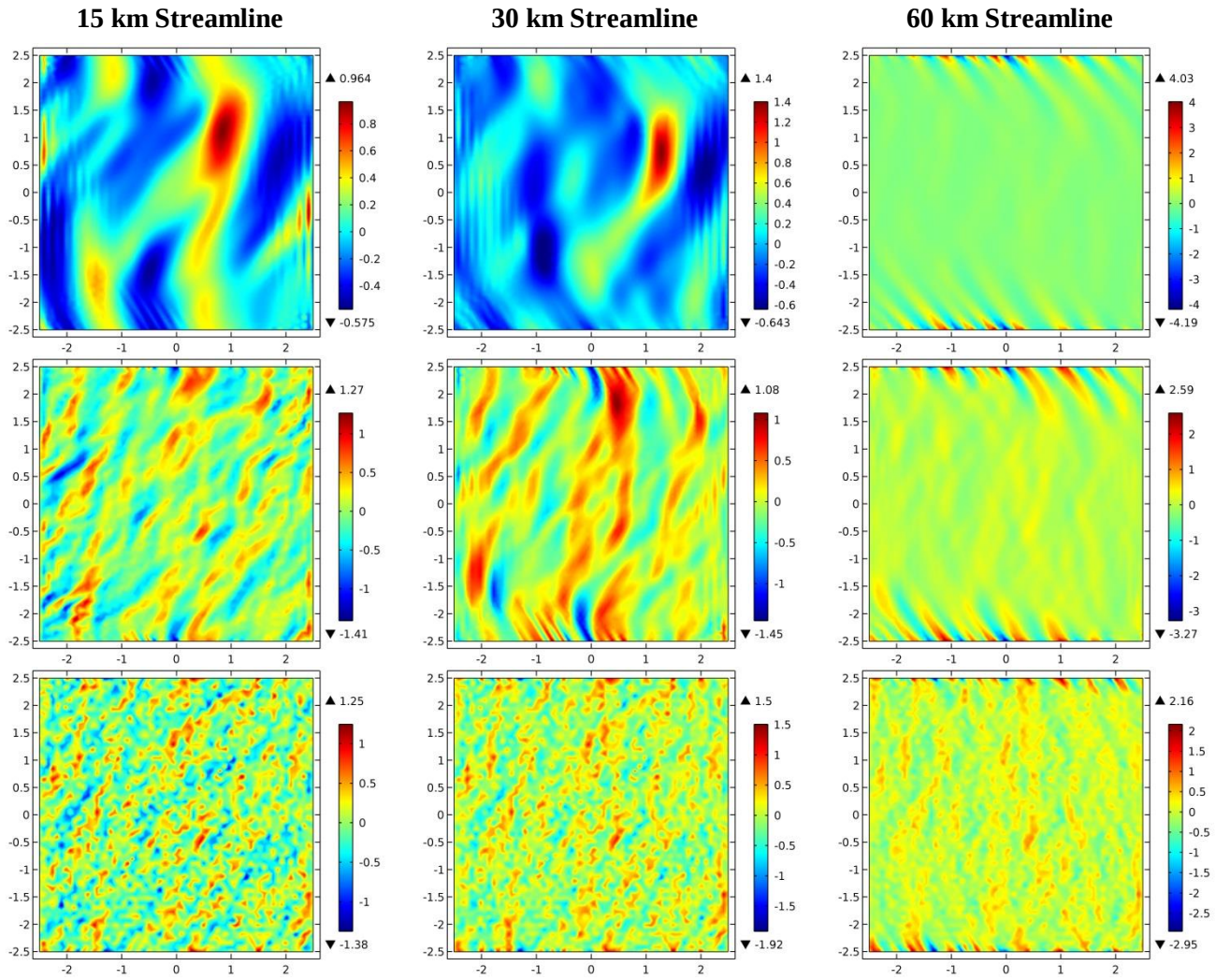

Figure 25: Nonlinear melt band evolution along multiple streamlines in the case of isotropic, strain rate dependent $(n_v = 6)$ matrix rheology and slow spreading ridge geometry. From the 15 km streamline, the panels come from 15.1 km from ridge axis and 62.4 km below the ridge crest (bottom), 15.5 km from ridge axis and 46.3 km below the ridge crest (middle), and 18.9 km from ridge axis and 26.4 km below the ridge crest (top). For the 30 km streamline, the panels come from 30.4 km from ridge axis and 66.1 km below the ridge crest (bottom), 33.2 km from ridge axis and 53.2 km below the ridge crest (middle), and 41.4 km from ridge axis and 43.4 km below the ridge crest (top). Finally, for the 60 km streamline, the panels come from 62.5 km from ridge axis and 68.4 km below the ridge crest (bottom), 69.0 km from ridge axis and 66.1 km below the ridge crest (middle), and 77.8 km from ridge axis and 65.2 km below the ridge crest (top). The top panel of the 60 km streamline is located at the base of the plate.

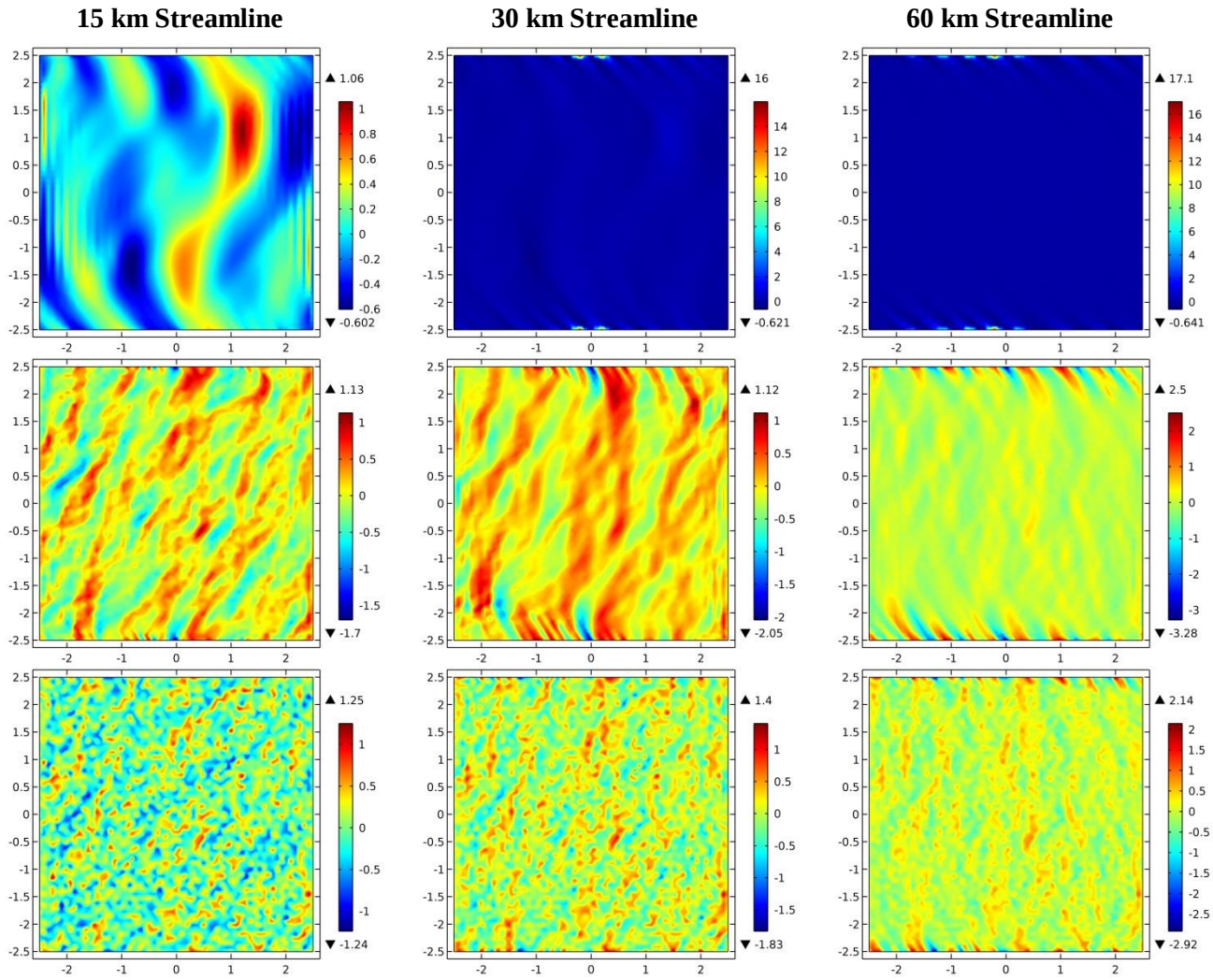

Figure 26: Nonlinear melt band evolution along multiple streamlines in the case of isotropic, strain rate dependent $(n_v = 6)$ matrix rheology and fast spreading ridge geometry. From the 15 km streamline, the panels come from 15.1 km from ridge axis and 62.7 km below the ridge crest (bottom), 15.5 km from ridge axis and 40.8 km below the ridge crest (middle), and 20.2 km from ridge axis and 17.6 km below the ridge crest (top). For the 30 km streamline, the panels come from 30.4 km from ridge axis and 63.5 km below the ridge crest (bottom), 32.7 km from ridge axis and 46.5 km below the ridge crest (middle), and 42.5 km from ridge axis and 30.6 km below the ridge crest (top). Finally, for the 60 km streamline, the panels come from 62.2 km from ridge axis and 65.4 km below the ridge crest (bottom), 66.2 km from ridge axis and 59.6 km below the ridge crest (middle), and 83.9 km from ridge axis and 48.6 km below the ridge crest (top).

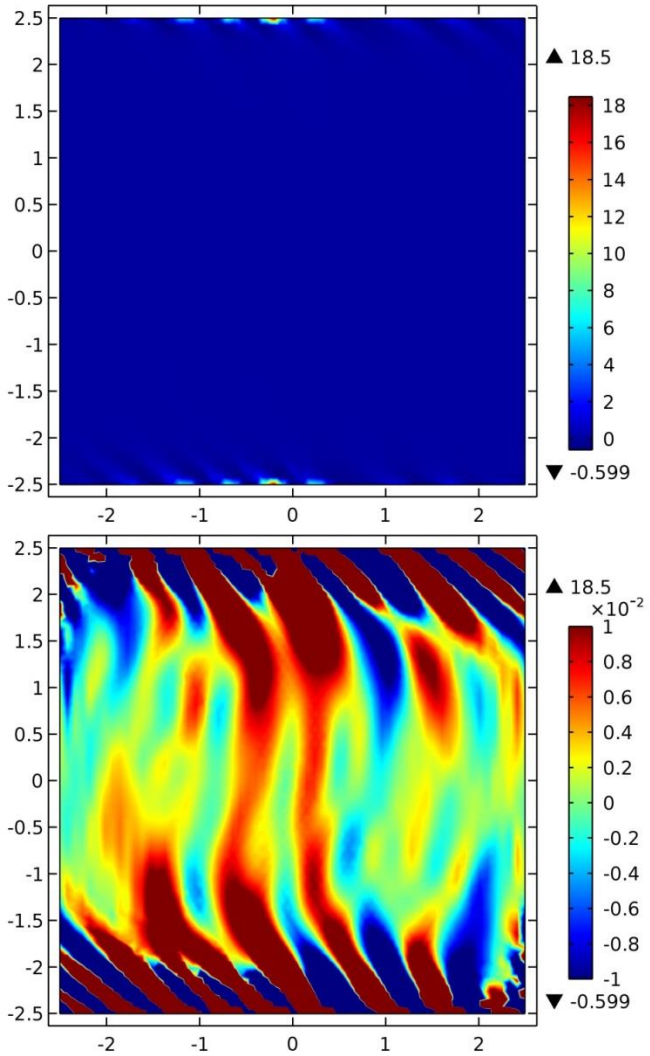

Figure 27: Both panels shows the end result of the 55 km streamline simulation for an isotropic, strain rate independent rheology for fast spreading ridge geometry. The top panel shows the original result of the porosity field while the bottom panel has had the maximum plotted values significantly lowered. In the bottom panel, yellow band-like structures are still visible and much of the porosity has accumulated on the top and bottom boundaries.

4.4 Nonlinear Simulation Results Discussion

One consistent feature of both isotropic, slow spreading geometry nonlinear models is that all simulations along streamlines beginning at horizontal positions after ~55km terminate well past the lithosphere-asthenosphere boundary. This has been noted in Figures 1 and 3, where the end position of the 60km streamline simulations comes from the lithosphere-asthenosphere boundary instead of the termination point of the simulation. For slow spreading streamlines with starting locations closer than 55km from the ridge axis, the models consistently terminated before reaching the base of the plate, and all nonlinear simulations terminated well before the base of the plate in the fast-spreading simulations. The termination locations for a number of streamlines are shown in Figure 28. The nonlinear models consistently terminate around strains of approximately 1, although this value decreases slightly with increasing horizontal distance from the ridge axis.

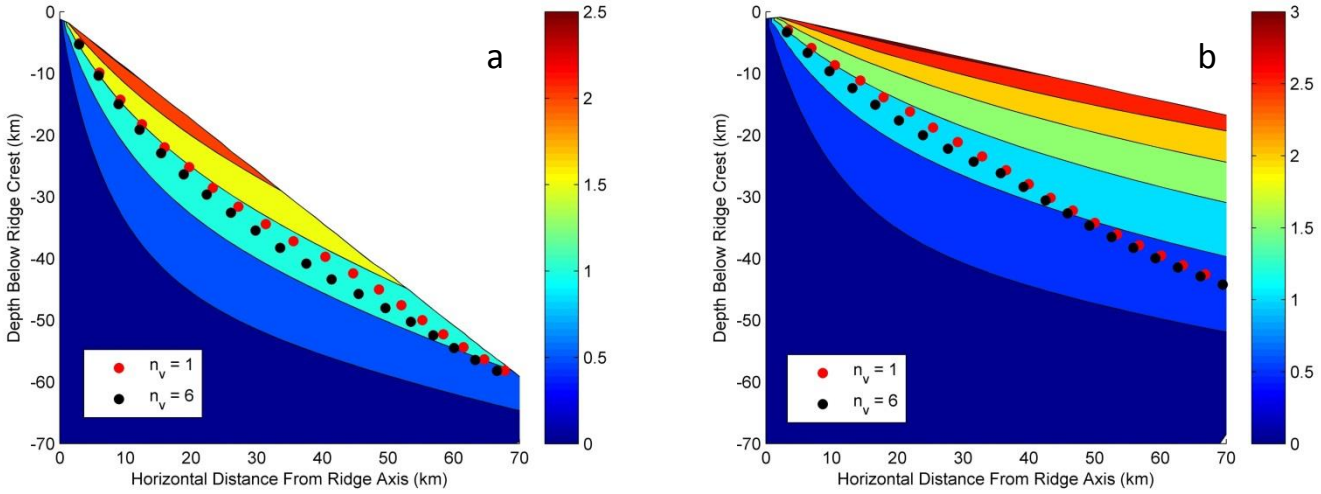

Figure 28: Termination points for nonlinear models are plotted over the contours of the integrated strain for the MOR corner flow. For a slow-spreading ridge (a), the models almost reach the base of the plate, while for fast-spreading geometry (b) the models terminate well before the lithosphere-asthenosphere boundary.

The porosity fields shown in Figures 23 through 26 are normalized at each time step, so as to clearly view the onset of band development. Without this normalization, no bands are visible until very close to the end of the simulation. For example, in the case of strain rate independent rheology along the 15 km streamline even though the porosity reaches $2\phi_0$ at a depth of 35.6 km, 19.3 km from the ridge axis no discernible band formation has occurred without normalizing the porosity. This location is significantly closer to the base of the plate than locations shown in the 15 km streamline panels in Figure 23 that were chosen to show the onset

of melt localization and the early-time bands. The maximum porosity reached by the end of that simulation is $\phi_{max} = 0.0293$, which is well below the RCMF maximum. Table 1 shows a summary of the nonlinear simulation data for the streamlines shown in Figures 23 through 26. All ϕ_{max} values occur at the end of the simulations and all locations are given in ordered pairs consisting of horizontal positions from the ridge axis and depths below the ridge crest. Table 1 clearly shows that the simulations that reach and exceed the RCMF do so generally at or soon before the termination of the model. Table 1 also shows that some two of the 60 km simulations solved past the lithosphere-asthenosphere boundary. In these cases, the porosity at the base of the plate is also given as ϕ_{plate}; in both instances ϕ_{plate} is not much larger than ϕ_0, indicating that the strain at that distance from the ridge axis was insufficient to cause significant melt localization.

Streamline Horizontal Start Location (km)	n_v	Wedge Angle	ϕ_{max}	ϕ_{plate}	$\phi > \phi_{RCMF}$ Location (km)	Simulation End (km)
15	1	40	0.0293	-	-	(19.6,25.4)
30	1	40	0.0558	-	-	(44.6,42.4)
60	1	40	0.319	0.0122	(74.7,65.6)	(77.5,65.3)
15	1	13	0.063	-	-	(21.9,16.2)
30	1	13	0.333	-	(43.3,30.1)	(43.3,30.1)
60	1	13	0.44	-	(84.5,48.3)	(85.0,48.2)
15	6	40	0.0273	-	-	(77.8,65.3)
30	6	40	0.0318	-	-	(41.4,43.4)
60	6	40	0.262	0.0127	-	(18.9,26.4)
15	6	13	0.0278	-	-	(20.2,17.6)
30	6	13	0.277	-	-	(42.5,30.6)
60	6	13	0.302	-	(83.9,48.6)	(83.9,48.6)

Table 1: Maximum porosity values for nonlinear COMSOL models. When the model continued past the lithosphere-asthenosphere boundary, the value of the porosity at the plate is given. The columns with distances provide a comparison between the location of the end of the model and the location where the porosity field exceeded the RCMF.

In the linear analysis, changing the value of the initial perturbation amplitude resulted in significant changes to the region throughout the MOR domain where the linear analysis was valid, in terms of the RCMF (Gebhardt and Butler, 2016). A similar test was conducted with the nonlinear models by increasing the variation in the random initial porosity field. Increasing the initial porosity field variation led to models terminating significantly earlier than before. For

example, the strain-rate independent, slow-spreading simulation along the 15km streamline ended at 19.6 km from the ridge axis and 25.4 km below the ridge crest. Increasing the initial porosity variation by a factor of 3 – mirroring the power decrease from the linear analysis – led to the model terminating much sooner along the streamline, at 16.0 km from the ridge axis and 39.3 km below the ridge crest. The magnitude of the end simulation porosity also increased to $\phi_{max} = 0.07$ (where before $\phi_{max} = 0.0293$), although there was less accumulation of porosity along the boundaries.

The Comsol models were also run with an increased bulk viscosity of 200. The linear analysis predicted that an increase in bulk viscosity would significantly reduce the possibility of melt channeling occurring in the porosity bands due to a significant decrease in permeability variation and perturbation amplitude. The effect of a raised bulk viscosity is similar to that found in the linear models in that little to no band growth is visible along any streamlines in the MOR domain. This is the case for both isotropic matrix rheologies as well as for both slow and fast spreading ridge geometries. An example of this is shown in Figure 29.

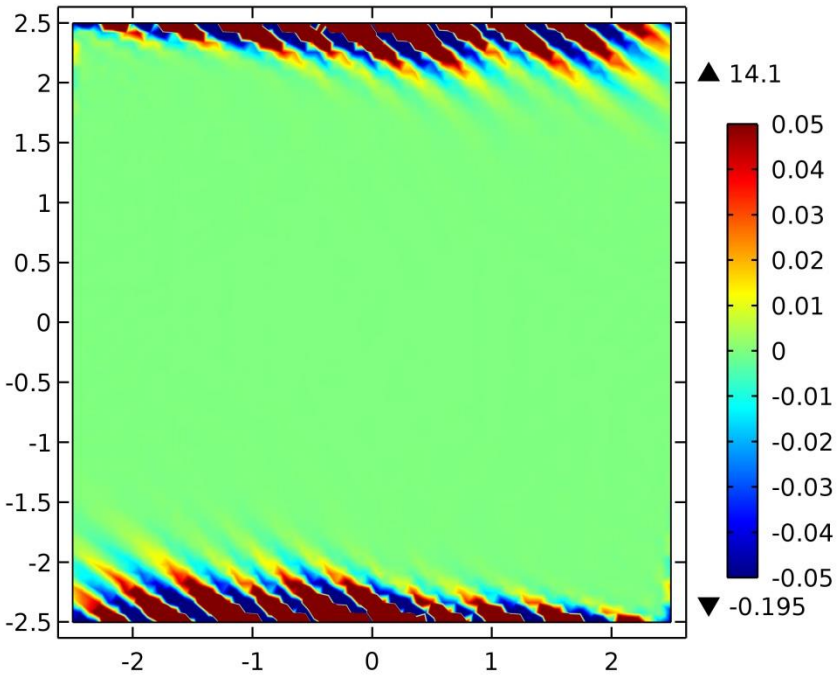

Figure 29: End result for a simulation run along the 40km streamline using fast spreading ridge geometry with strain rate independent matrix rheology. The colour range has been modified to highlight bands, of which none are present.

The high bulk viscosity simulations progressed slightly further along streamlines before they terminate. However, a similar high porosity "noise" was still present along the top and

bottom boundaries of the domain. In Figure 29, the maximum porosity in the domain by the end of the simulation was $\phi_{max} = 0.74$, which is well above the RCMF limit. The accumulation of porosity along the top and bottom boundaries despite a lack of band formation throughout the rest of the simulation domain seems to indicate that this accumulation is unrelated to band growth and instead is due to some sort of as-yet-unidentified numerical issue.

4.5 Comparing the Linear and Nonlinear Models

The primary means of comparison for the linear and nonlinear models is the generation of an angular spectrum from the nonlinear data. Power spectra calculated from the integration of the amplitude of the discrete Fourier transform of the nonlinear porosity field at each angle will give the porosity amplitude variation with angle; this is done for all time steps in the slow nonlinear models and at every second time step in the fast models. Generating an angular spectrum allows for a direct comparison with the band orientations found in the linear analysis. The results of this are shown in Figures 30 through 41.

In each of these figures the power spectrum from 0° to 180° is contoured, with the orientations corresponding to the fastest growing bands as calculated from the linear analysis indicated with a black dashed line and orientations for the bands with the maximum porosity perturbation given in solid black. In some of the figures, there are two separate solid black lines and sometimes also a solid green line. Two solid black lines are shown when there are two maxima in the linear analysis. The green lines correspond to the half-max-amplitude envelope. The envelope is not included in all the angular spectrum plots in an effort to make the figures less busy.

In general, the nonlinear and linear orientations are quite similar. This is in keeping with previous work by Butler (2009, 2010) where good agreement was demonstrated between the results of linear and nonlinear models until near the end of simulations, where strains of around 1 occurred. The late-time spectra presented here may not be reliable due to the tendency for boundaries to accumulate porosity in the nonlinear models. The 15 km streamline spectra appears to show most nonlinear bands forming near the orientation of fastest growing linear bands; however, the maximum perturbation orientations are not entirely dissimilar from the distribution of the spectra, in particular in the strain rate dependent rheology cases – see Figures

36 and 39. The predominant angles in 30 km spectra seem to favor the maximum perturbation amplitude orientations in the strain rate dependent rheology cases (Figures 37 and 40), while the strain rate independent rheology produces spectra where the most prominent orientations are located between the fastest growing and maximally perturbed orientations. The 30 km streamlines presented porosity accumulation along the boundaries in Figures 23 through 26. This is certainly evident in the fast spreading spectra at 0° and 180°, and it is also possibly evident in the late-runtime spectra highs at sub-75° orientations.

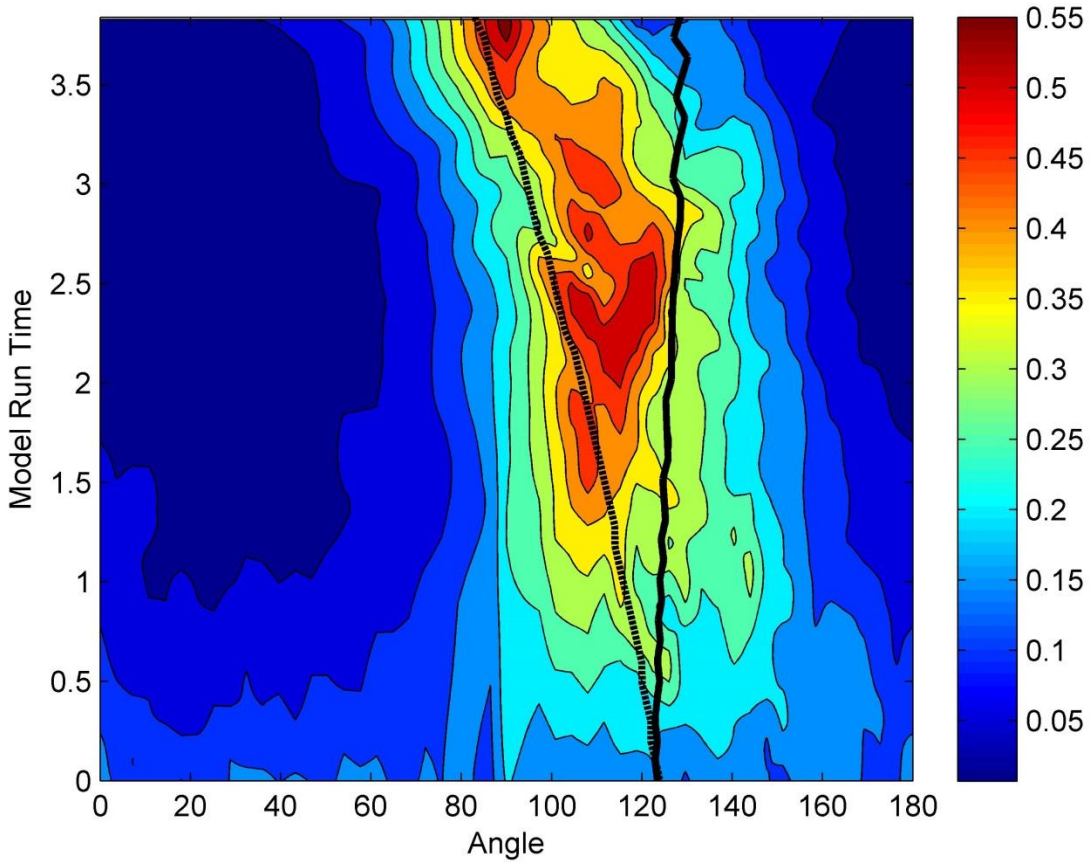

Figure 30: Contour of the angular power spectrum for the nonlinear simulation along the 15 km slow-spreading streamline for a strain rate independent matrix rheology. Overlaying the spectrum contour are orientations from the linear analysis. Orientations for the fastest growing bands are given by the dashed lines while the orientations for the bands with the maximum porosity perturbation are given in solid black.

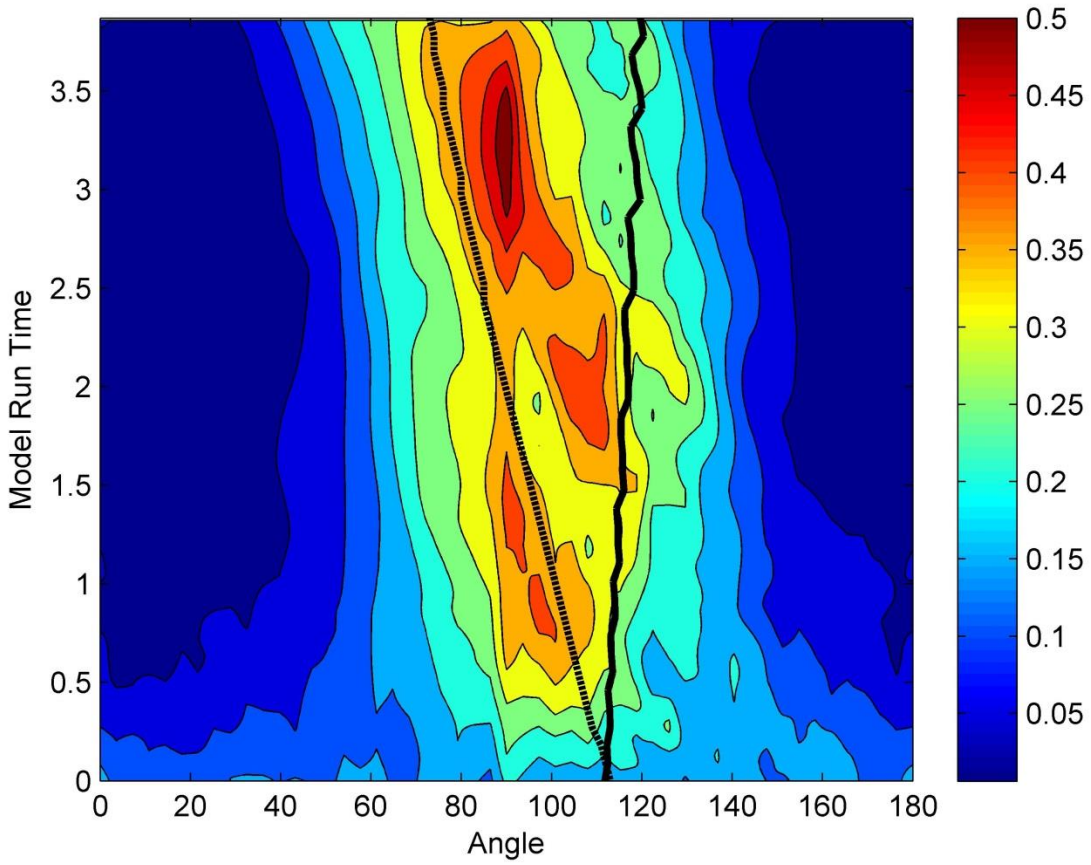

Figure 31: Contour of the angular power spectrum for the nonlinear simulation along the 30 km slow-spreading streamline for a strain rate independent matrix rheology.

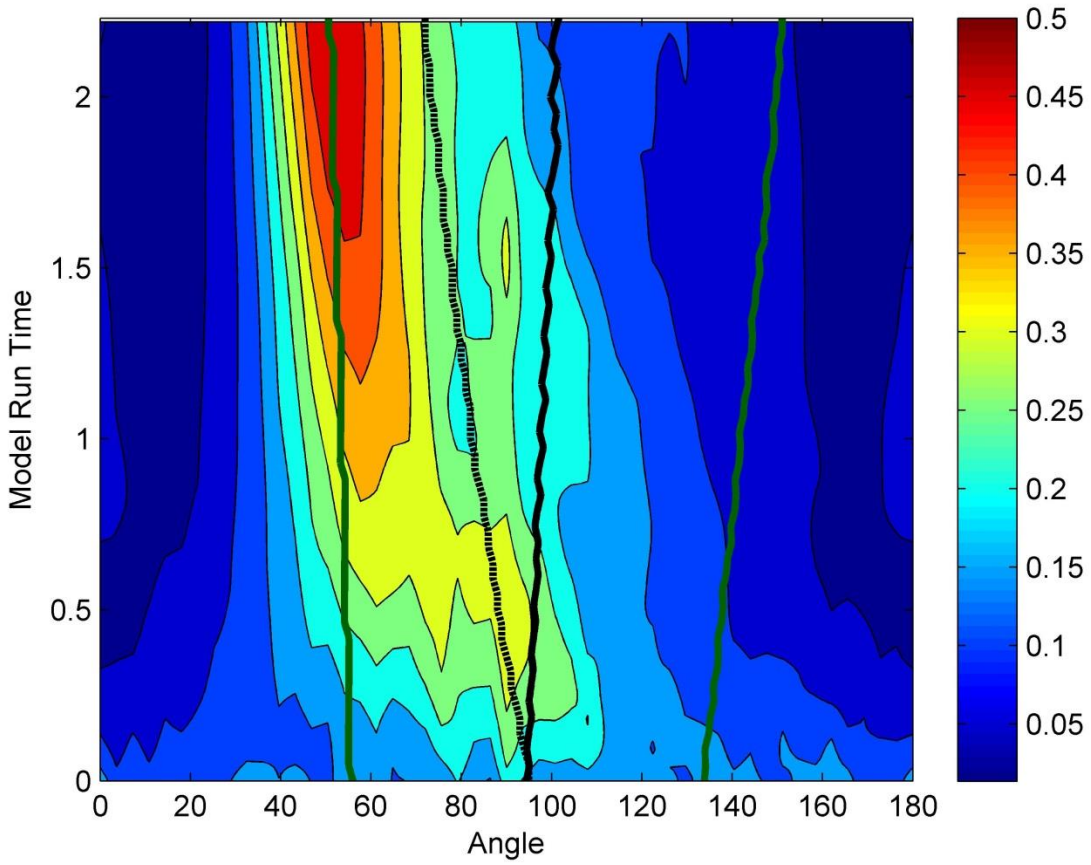

Figure 32: Contour of the angular power spectrum for the nonlinear simulation along the 60 km slow-spreading streamline for a strain rate independent matrix rheology, now also with the half-maximum-amplitude envelope given in green.

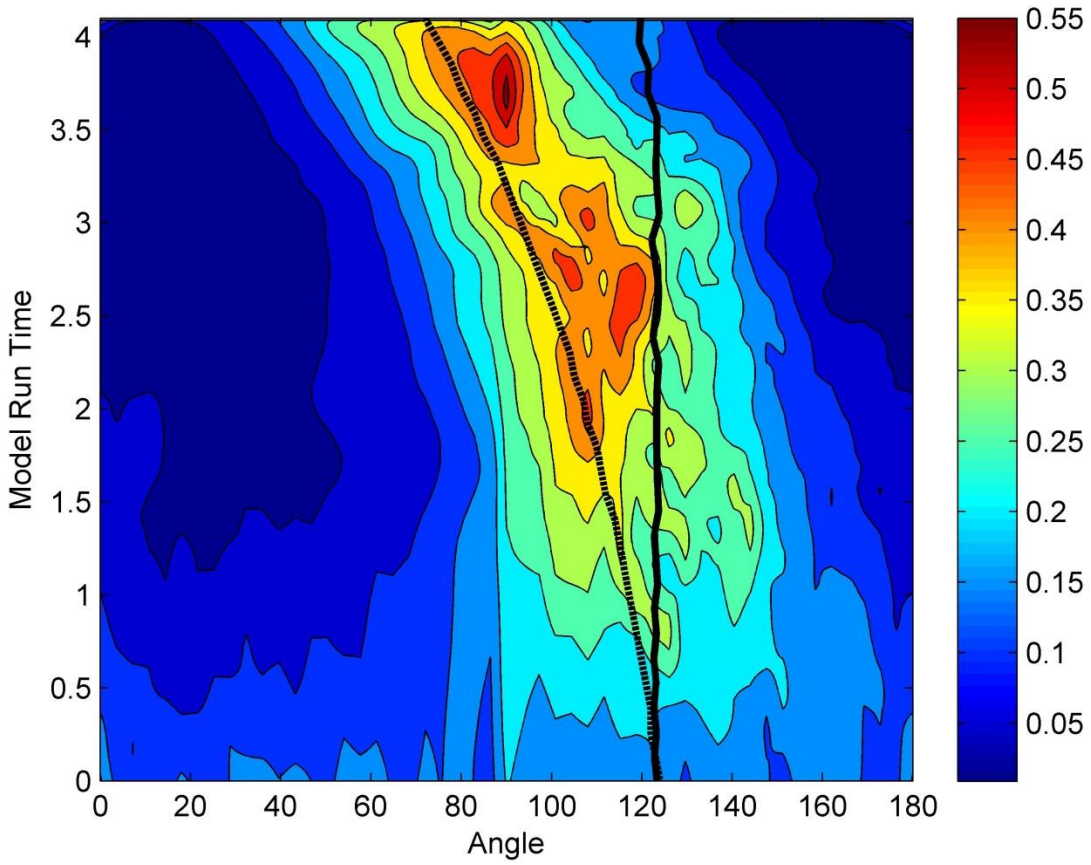

Figure 33: Contour of the angular power spectrum for the nonlinear simulation along the 15 km fast-spreading streamline for a strain rate independent matrix rheology.

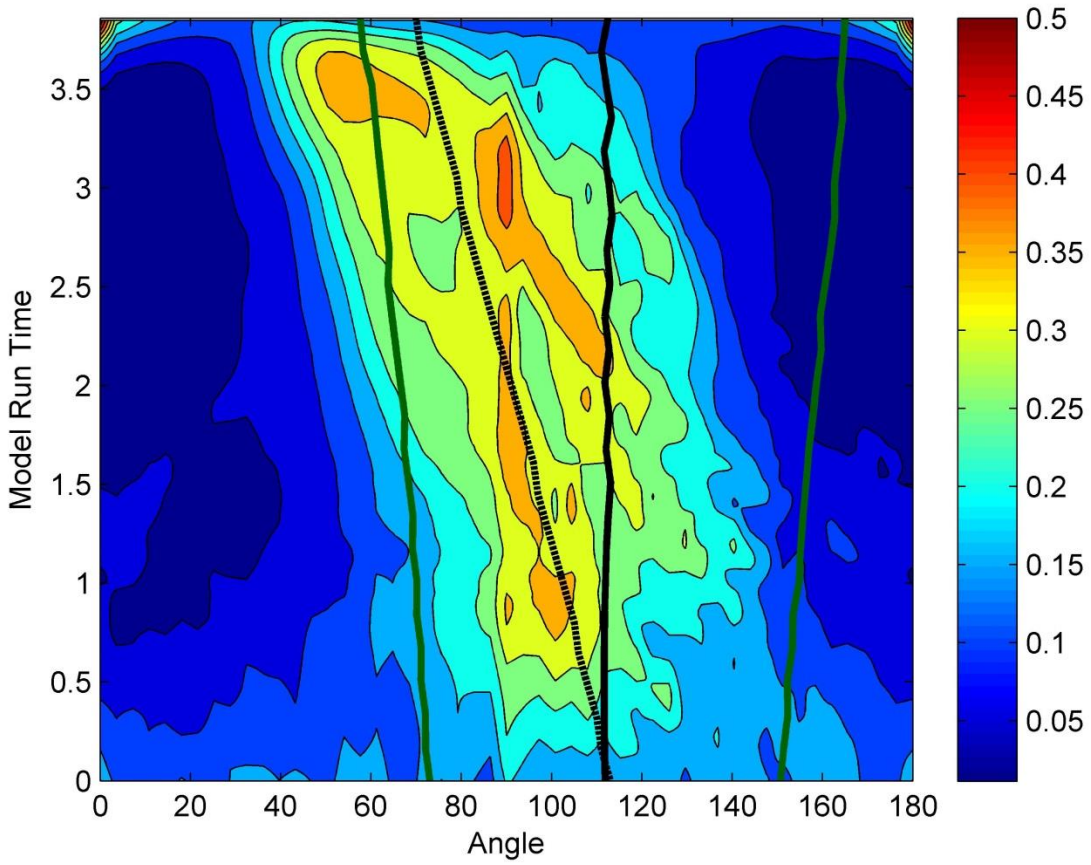

Figure 34: Contour of the angular power spectrum for the nonlinear simulation along the 30 km fast-spreading streamline for a strain rate independent matrix rheology.

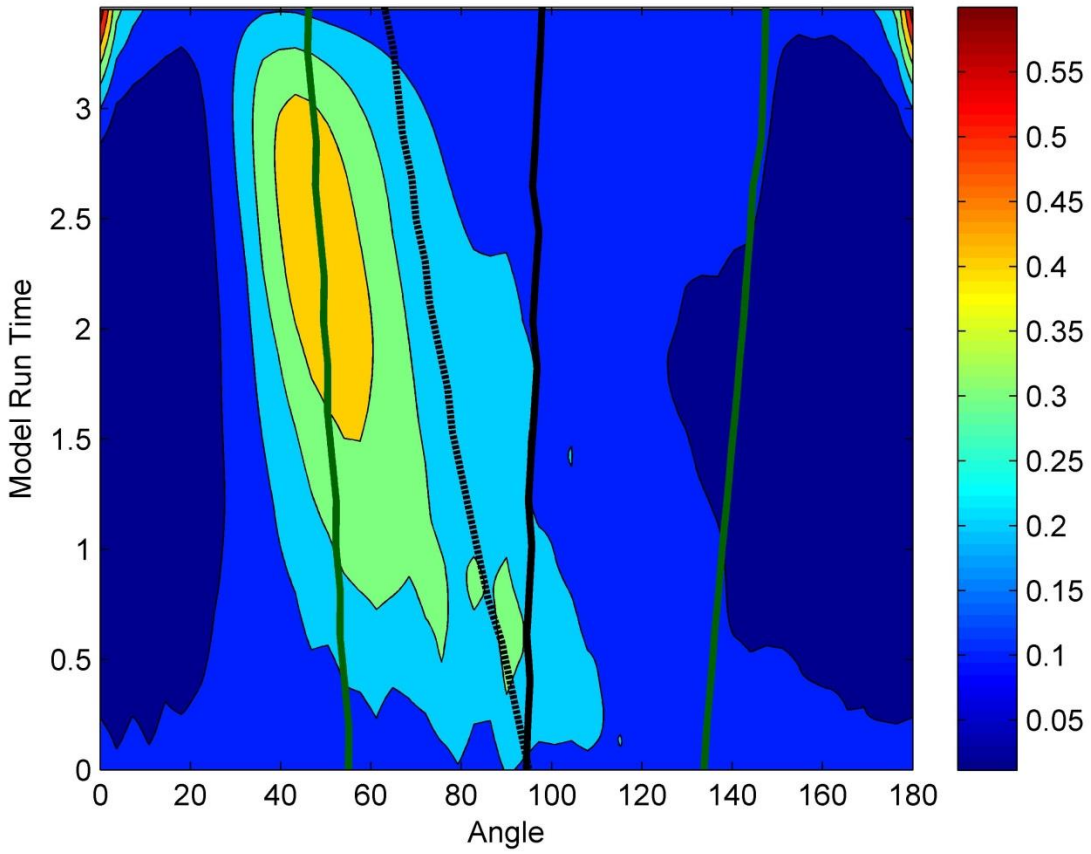

Figure 35: Contour of the angular power spectrum for the nonlinear simulation along the 60 km fast-spreading streamline for a strain rate independent matrix rheology.

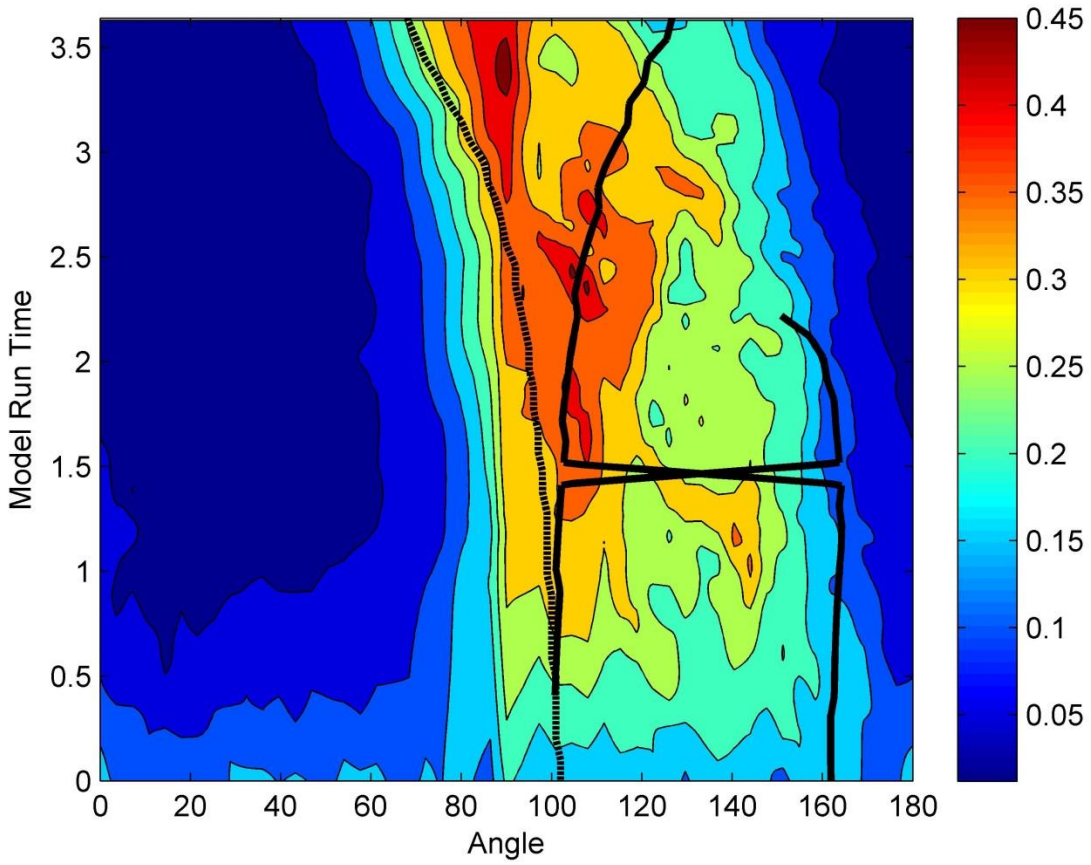

Figure 36: Contour of the angular power spectrum for the nonlinear simulation along the 15 km slow-spreading streamline for a strain rate dependent matrix rheology. Note that there are now occasionally two orientations given for the maximally perturbed bands, shown with two solid black lines.

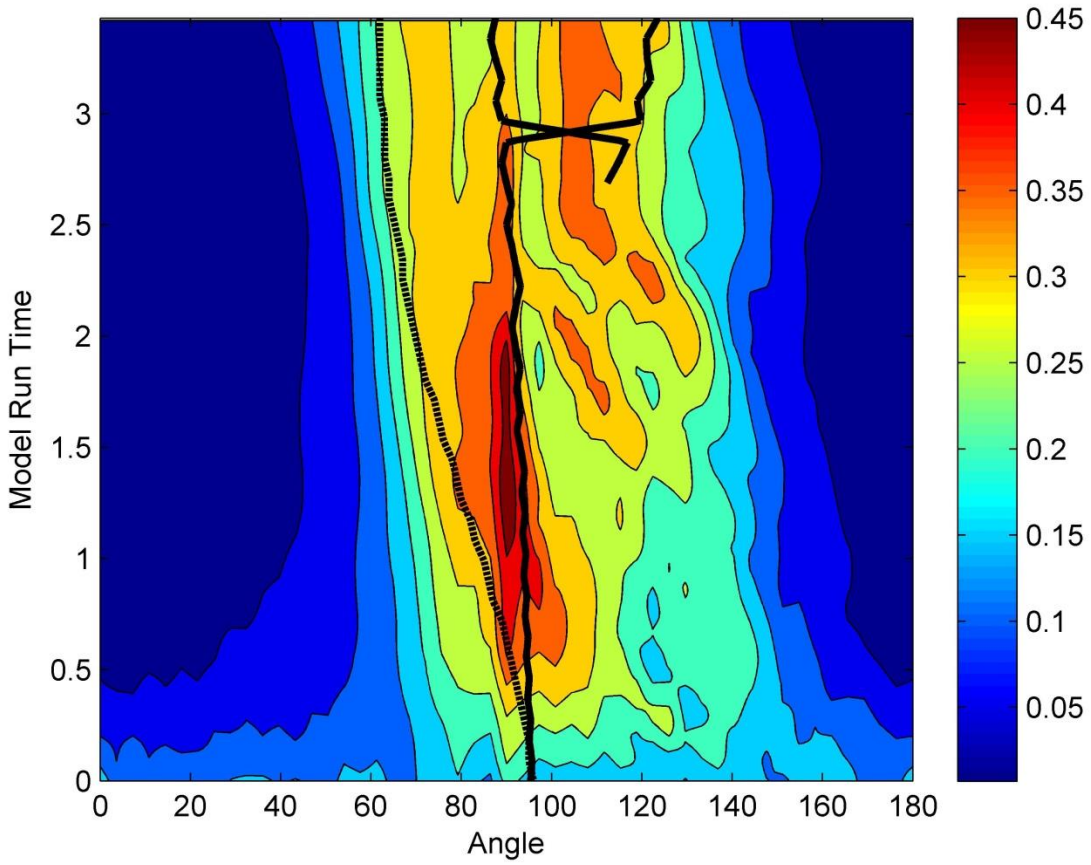

Figure 37: Contour of the angular power spectrum for the nonlinear simulation along the 30 km slow-spreading streamline for a strain rate dependent matrix rheology

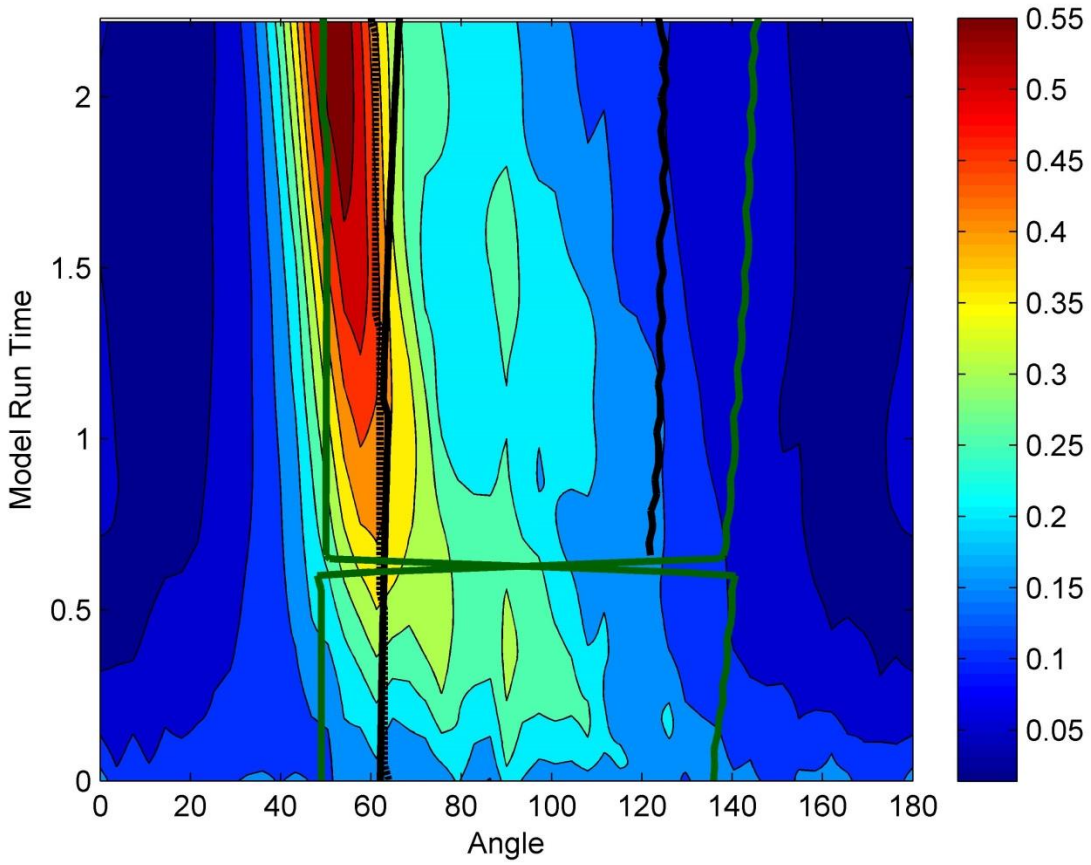

Figure 38: Contour of the angular power spectrum for the nonlinear simulation along the 60 km slow-spreading streamline for a strain rate dependent matrix rheology

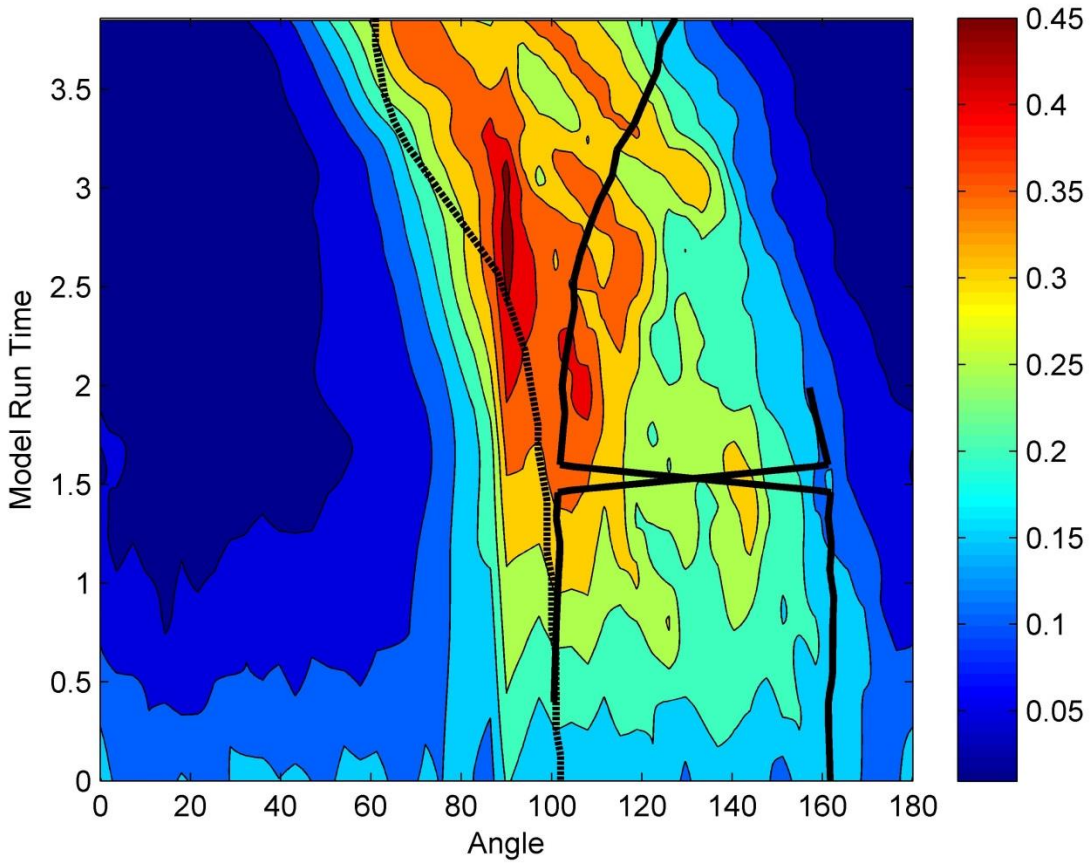

Figure 39: Contour of the angular power spectrum for the nonlinear simulation along the 15 km fast-spreading streamline for a strain rate dependent matrix rheology

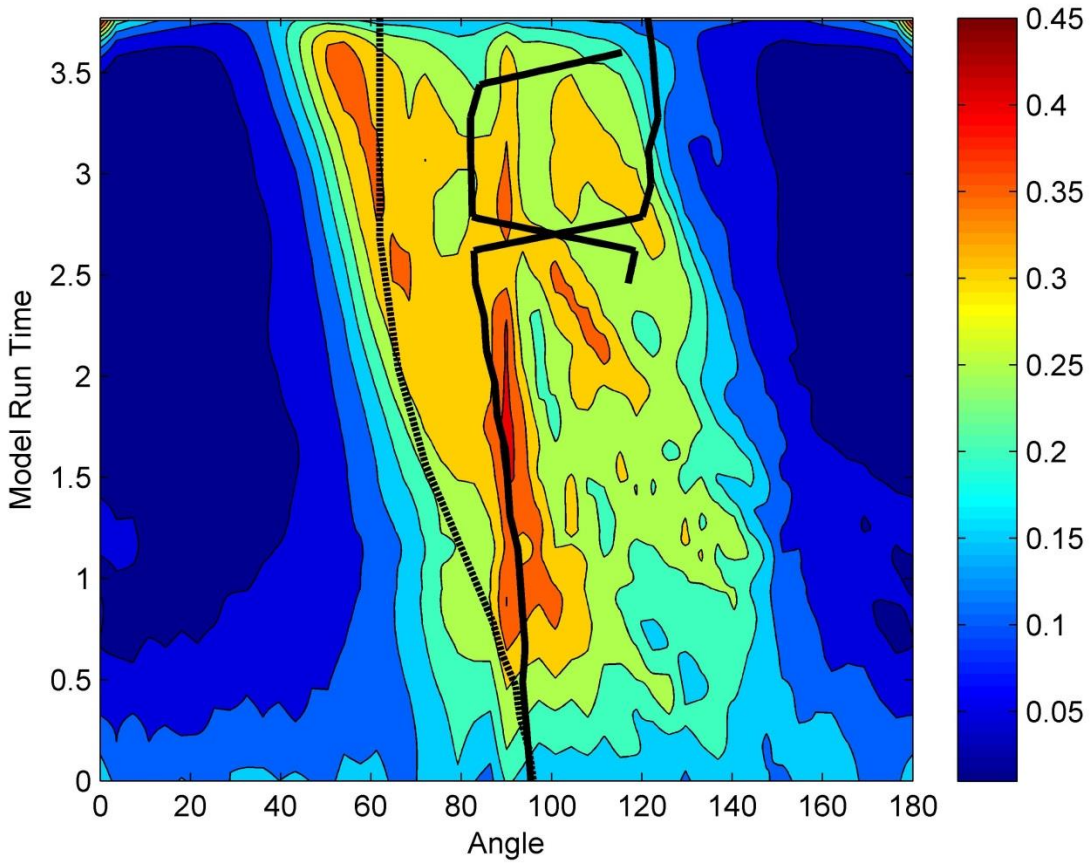

Figure 40: Contour of the angular power spectrum for the nonlinear simulation along the 30 km fast-spreading streamline for a strain rate dependent matrix rheology

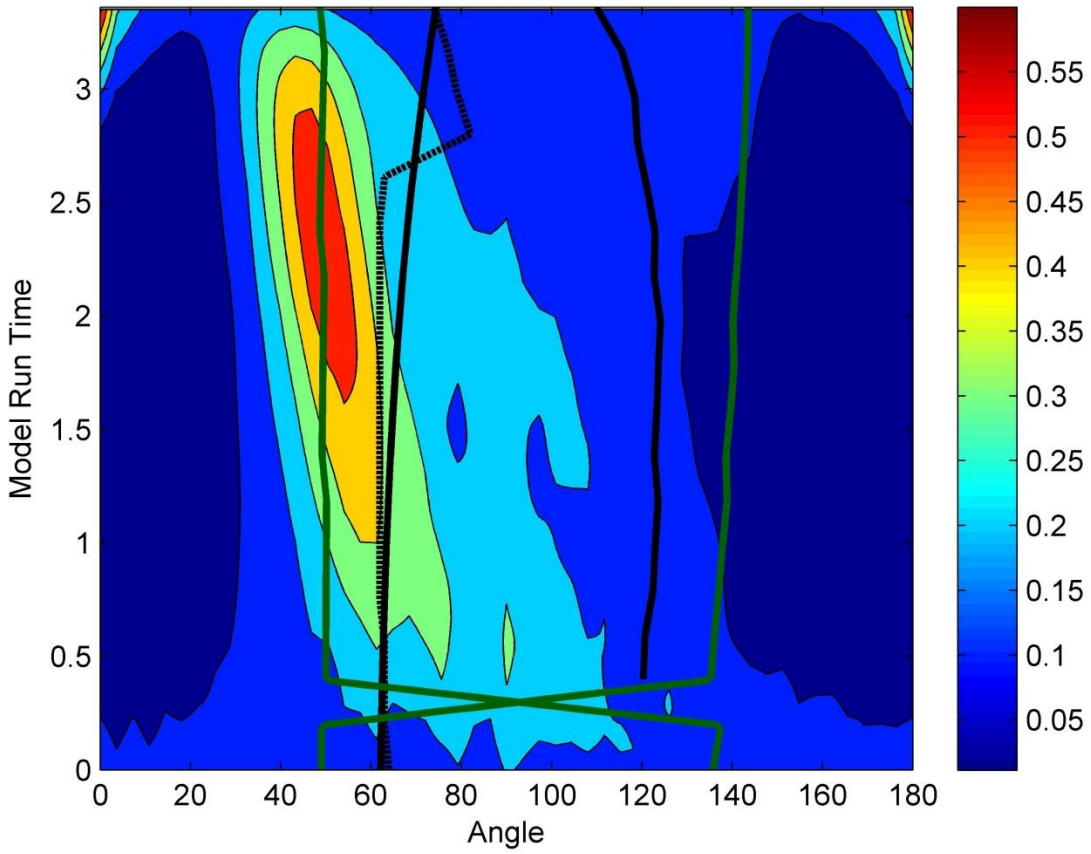

Figure 41: Contour of the angular power spectrum for the nonlinear simulation along the 60 km fast-spreading streamline for a strain rate dependent matrix rheology

The 60 km streamline spectra demonstrate the least agreement between linear and nonlinear orientations. These spectra consistently produce bands that are orientated at smaller angles to horizontal than both the fastest growing and maximally perturbed linear orientations. The bands formed along the 60 km streamline do not likely reach very large amplitudes, and so those simulations are likely to be more affected by the numerical instability on the boundary. Despite this, the nonlinear orientations still fall within the half-maximum amplitude envelope.

Despite witnessing no significant band growth in the anisotropic simulations, a comparison between the anisotropic nonlinear and linear models is briefly considered in Appendix 8.

Chapter 6: Conclusions

The melt bands formed using the numerical methods described in this thesis were not oriented directly toward the ridge axis and therefore will not likely serve as a mechanism for off-axis, lateral melt channelling at MORs. The melt bands evaluated in the linear analysis presented fast growing bands that were oriented toward the ridge axis, but these orientations did not persist in time as the cumulative effect of the background flow rotated bands into orientations facing the lithosphere-asthenosphere boundary. This was found to be the case for both fast and slow spreading ridge geometries, and for all three considered matrix rheologies: isotropic strain rate independent, isotropic strain rate dependent, and anisotropic strain rate independent. The nonlinear models presented band orientations that were similar to, although not exactly alike, those found in the linear analysis. This was found to be the case for all isotropic matrix rheologies. The anisotropic nonlinear model did not produce any significant bands. However, the anisotropic models, like all other nonlinear models, did present significant porosity accumulation along the top and bottom boundary which was often in excess of the RCMF. The origin of this porosity accumulation is believed to the result of a numerical instability.

The numerical methods used here revealed that the formation of melt bands at MORs is sensitive to two poorly constrained quantities: the matrix bulk viscosity of the mantle and the initial porosity. Both models found that the matrix bulk viscosity should be relatively small or else bands will at best be insignificant, if present at all. The linear analysis predicted that melt bands would likely only experience a sufficient change in porosity and permeability to effectively channel melt at close distances to the base of the plate. The nonlinear models often terminated before the model domain got very close to the base of the plate, especially in the case of fast spreading geometry. Increasing the initial porosity perturbation in the linear analysis led to larger areas of the MOR domain where the porosity exceeds the disaggregation limit for mantle rock. Similarly, increasing the magnitude of the initial porosity variation in the nonlinear model led to shorter runtimes for models.

The band orientations here do not support the notion that melt bands can serve as a mechanism for channeling melt directly to the ridge axis. Instead I would like to suggest that the melt bands oriented toward the base of the plate are ideal for channelling melt to the decompaction boundary layer proposed by Sparks and Parmentier (1991). This theoretical melt-

channelling model focuses on the claim that one of the phases in upwelling partial melt from the mantle freezes upon reaching the base of the plate at the lithosphere-asthenosphere boundary. In doing so a high porosity region opens up along the base of the plate, the decompaction boundary layer. Melt could then be transported to the ridge axis through this layer along the base of the plate under the influence of gravity.

5.1 Future Considerations

An obvious next-step for follow up research on this topic would be to make the model more Earth-like. This would be done by accounting for buoyancy and thermodynamics. Accounting for buoyancy would potentially help address a difference of opinion currently in the literature: Butler (2009) demonstrated that buoyancy can contribute to bands remaining near their orientation of fastest growth, while Katz (2010) saw no bands form in the MOR models that incorporated the necessary porosity-weakening rheology and buoyancy. Thermodynamics could be introduced by accounting for mass transfer between the matrix and melt phases through ongoing melting and by adding temperature dependence to the viscosity of both the matrix phase and the corner flow model. Additionally, incorporating thermodynamics could entail the inclusion of volatiles and reactive flow.

The physics presented here is only valid at small melt fractions (McKenzie, 1984), and at least some of the linear and nonlinear results presented here are in clear violation of the disaggregation limit for mantle rock. Subsequent partial melt investigations might identify the missing physics that can better control or limit the growth of porosity instabilities, or in some other way reconcile numerical studies of partial melt with experimental work. Knowing this, follow up research on this topic should incorporate any future work that contributes to a better understanding of the behaviour the deformation of partial melt.

Chapter 7: References

Ahern, J. and D. Turcotte (1979), Magma migration beneath an ocean ridge, *Earth and Planetary Science Letters*, *45*(1), 115-122, doi:10.1016/0012-821x(79)90113-4.

Batchelor, G. (1967), *An introduction to fluid dynamics*, U.P., Cambridge.

Bercovici, D., and Y. Ricard (2003), Energetics of a two-phase model of lithospheric damage, shear localization and plate-boundary formation, *Geophysical Journal International*, *152*(3), 581-596, doi:10.1046/j.1365-246x.2003.01854.x.

Butler, S. L. (2009), The effects of buoyancy on shear-induced melt bands in a compacting porous medium, *Physics of the Earth and Planetary Interiors*, *173*(1-2), 51-59, doi:10.1016/j.pepi.2008.10.022.

Butler, S. L. (2010), Porosity localizing instability in a compacting porous layer in a pure shear flow and the evolution of porosity band wavelength, *Physics of the Earth and Planetary Interiors*, *182*(1-2), 30-41, doi:10.1016/j.pepi.2010.06.004.

Butler, S. L. (2012), Numerical models of shear-induced melt band formation with anisotropic matrix viscosity, *Physics of the Earth and Planetary Interiors*, *200-201*, 28-36, doi:10.1016/j.pepi.2012.03.011.

Carman, P. (1939), Permeability of saturated sands, soils and clays, *J. Agric. Sci.*, *29*(02), 262, doi:10.1017/s0021859600051789.

Ceuleneer, G. and M. Rabinowicz (1992), Mantle Flow and Melt Migration beneath Oceanic Ridges: Models derived from Observations in Ophiolites, in *Mantle Flow and Melt Generation at Mid-Ocean Ridges*, ed. by J. Phipps Morgan, D. K. Blackman and J. M. Sinton, pp. 123-154, American Geophysical Union, Washington, DC.

Craik, A., and W. Criminale (1986), Evolution of Wavelike Disturbances in Shear Flows: A Class of Exact Solutions of the Navier-Stokes Equations, *Proceedings of the Royal Society A: Mathematical, Physical and Engineering Sciences*, *406*(1830), 13-26, doi:10.1098/rspa.1986.0061.

Daines, M., and D. Kohlstedt (1997), Influence of deformation on melt topology in peridotites, *J. Geophys. Res.*, *102*(B5), 10257, doi:10.1029/97jb00393.

Forsyth, D., D.S. Sheirer, S.C. Webb, et al (1998), Imaging the Deep Seismic Structure Beneath a Mid-Ocean Ridge: The MELT Experiment, *Science*, *280*(5367), 1215-1218, doi:10.1126/science.280.5367.1215.

Gebhardt, D. and S. Butler (2016), Linear analysis of melt band formation in a mid-ocean ridge corner flow, *Geophys. Res. Lett.*, *43*(8), 3700-3707, doi:10.1002/2016gl068688.

Hirth, G., and D. Kohlstedt (2003), Rheology of the upper mantle and the mantle wedge: A view from the experimentalists, *Inside the Subduction Factory*, 83-105, doi:10.1029/138gm06.

Holtzman, B., and D. Kohlstedt (2007), Stress-driven Melt Segregation and Strain Partitioning in Partially Molten Rocks: Effects of Stress and Strain, *Journal of Petrology*, *48*(12), 2379-2406, doi:10.1093/petrology/egm065.

Holtzman, B., N. Groebner, M. Zimmerman, S. Ginsberg, and D. Kohlstedt (2003), Stress-driven melt segregation in partially molten rocks, *Geochemistry, Geophysics, Geosystems*, *4*(5), doi:10.1029/2001gc000258.

Katz, R., M. Spiegelman, and B. Holtzman (2006), The dynamics of melt and shear localization in partially molten aggregates, *Nature*, *442*(7103), 676-679, doi:10.1038/nature05039.

Katz, R. (2010), Porosity-driven convection and asymmetry beneath mid-ocean ridges, *Geochemistry, Geophysics, Geosystems*, *11*(11), n/a-n/a, doi:10.1029/2010gc003282.

Katz, R., and Y. Takei (2013), Consequences of viscous anisotropy in a deforming, two-phase aggregate. Part 2. Numerical solutions of the full equations, *J. Fluid Mech.*, *734*, 456-485, doi:10.1017/jfm.2013.483.

Katz, R. and S. Weatherley (2012), Consequences of mantle heterogeneity for melt extraction at mid-ocean ridges, *Earth and Planetary Science Letters*, *335-336*, 226-237, doi:10.1016/j.epsl.2012.04.042.

Kelemen, P., G. Hirth, N. Shimizu, M. Spiegelman, and H. Dick (1997), A review of melt migration processes in the adiabatically upwelling mantle beneath oceanic spreading ridges, *Philosophical Transactions of the Royal Society A: Mathematical, Physical and Engineering Sciences*, *355*(1723), 283-318, doi:10.1098/rsta.1997.0010.

King, D., M. Zimmerman, and D. Kohlstedt (2010), Stress-driven Melt Segregation in Partially Molten Olivine-rich Rocks Deformed in Torsion, *Journal of Petrology*, *51*(1-2), 21-42, doi:10.1093/petrology/egp062.

Kohlstedt, D., M. Zimmerman, and S. Mackwell (2010), Stress-driven Melt Segregation in Partially Molten Feldspathic Rocks, *Journal of Petrology*, *51*(1-2), 9-19, doi:10.1093/petrology/egp043.

Korenaga, J., and S. Karato (2008), A new analysis of experimental data on olivine rheology, *J. Geophys. Res.*, *113*(B2), doi:10.1029/2007jb005100.

Lachenbruch, A. (1976), Dynamics of a passive spreading center, *J. Geophys. Res.*, *81*(11), 1883-1902, doi:10.1029/jb081i011p01883.

Lowrie, W. (2007), *Fundamentals of geophysics*, Cambridge University Press, Cambridge.

McKenzie, D. (1984), The Generation and Compaction of Partially Molten Rock, *Journal of Petrology, 25*(3), 713-765, doi:10.1093/petrology/25.3.713.

Mei, S., W. Bai, T. Hiraga, and D. Kohlstedt (2002), Influence of melt on the creep behavior of olivine-basalt aggregates under hydrous conditions, *Earth and Planetary Science Letters, 201*(3-4), 491-507, doi:10.1016/s0012-821x(02)00745-8.

Qi, C., D. Kohlstedt, R. Katz, and Y. Takei (2015), Experimental test of the viscous anisotropy hypothesis for partially molten rocks, *Proceedings of the National Academy of Sciences*, 201513790, doi:10.1073/pnas.1513790112.

Richardson, C. (1998), Melt flow in a variable viscosity matrix, *Geophys. Res. Lett., 25*(7), 1099-1102, doi:10.1029/98gl50565.

Scott, D., and D. Stevenson (1984), Magma solitons, *Geophys. Res. Lett., 11*(11), 1161-1164, doi:10.1029/gl011i011p01161.

Scott, T., and D. Kohlstedt (2006), The effect of large melt fraction on the deformation behavior of peridotite, *Earth and Planetary Science Letters, 246*(3-4), 177-187, doi:10.1016/j.epsl.2006.04.027.

Searle, R. (2013), *Mid-ocean ridges*, U.P., Cambridge.

Sparks, D., and E. Parmentier (1991), Melt extraction from the mantle beneath spreading centers, *Earth and Planetary Science Letters, 105*(4), 368-377, doi:10.1016/0012-821x(91)90178-k.

Spiegelman, M., and D. McKenzie (1987), Simple 2-D models for melt extraction at mid-ocean ridges and island arcs, *Earth and Planetary Science Letters, 83*(1-4), 137-152, doi:10.1016/0012-821x(87)90057-4.

Spiegelman, M. (2003), Linear analysis of melt band formation by simple shear, *Geochemistry, Geophysics, Geosystems, 4*(9), n/a-n/a, doi:10.1029/2002gc000499.

Stevenson, D. (1989), Spontaneous small-scale melt segregation in partial melts undergoing deformation, *Geophys. Res. Lett., 16*(9), 1067-1070, doi:10.1029/gl016i009p01067.

Takei, Y., and B. Holtzman (2009), Viscous constitutive relations of solid-liquid composites in terms of grain boundary contiguity: 3. Causes and consequences of viscous anisotropy, *J. Geophys. Res., 114*(B6), doi:10.1029/2008jb005852.

Takei, Y., and R. Katz (2013), Consequences of viscous anisotropy in a deforming, two-phase aggregate. Part 1. Governing equations and linearized analysis, *J. Fluid Mech., 734*, 424-455, doi:10.1017/jfm.2013.482.

Vera, E., J. Mutter, P. Buhl, J. Orcutt, A. Harding, M. Kappus, R. Detrick, and T. Brocher (1990), The structure of 0- to 0.2-m.y.-old oceanic crust at 9°N on the East Pacific Rise

from expanded spread profiles, *J. Geophys. Res.*, *95*(B10), 15529, doi:10.1029/jb095ib10p15529.

Appendix 1: Table of Selected Variables

	Symbol	Value
Melt fraction/porosity	ϕ	
Matrix, melt velocities	$\vec{U} = [U, V], \quad \vec{u} = [u, v]$	
Matrix permeability	k_ϕ	
Melt viscosity	μ	
Melt pressure	P	
Matrix bulk viscosity	ξ	
Matrix shear viscosity	η	
Bulk/shear viscosity ratio viscosity	r_ξ	5/3, 100
Initial porosity	ϕ_0	0.01
Initial porosity heterogeneity amplitude	$\Delta\phi$	1e-3, 1e-6
Perturbation angle clockwise from horizontal	θ	0° – 180°
Compaction length	δ_c	100 – 1000 m
Porosity weakening factor	λ	-25
Strain exponent	n_v	1, 6
Anisotropy magnitude	α	0 – 2
Anisotropy angle	Θ	
Saturation stress for anisotropy magnitude	σ_{sat}	2
Wedge angle	δ	13°, 40°

Table 2: This table contains a list of selected variables used in this analysis with corresponding symbols. Values are given when applicable.

Appendix 2: Anisotropic Viscosity Model

As stated earlier in section 2.4, the anisotropic matrix shear viscosity law presented by Takei and Katz (2013) is focused on the introduction of an anisotropy tensor. This tensor is the result of a grain-scale contiguity model in which grains are assumed to have 14 contact faces of radius a, as shown on the far right of Figure 42.

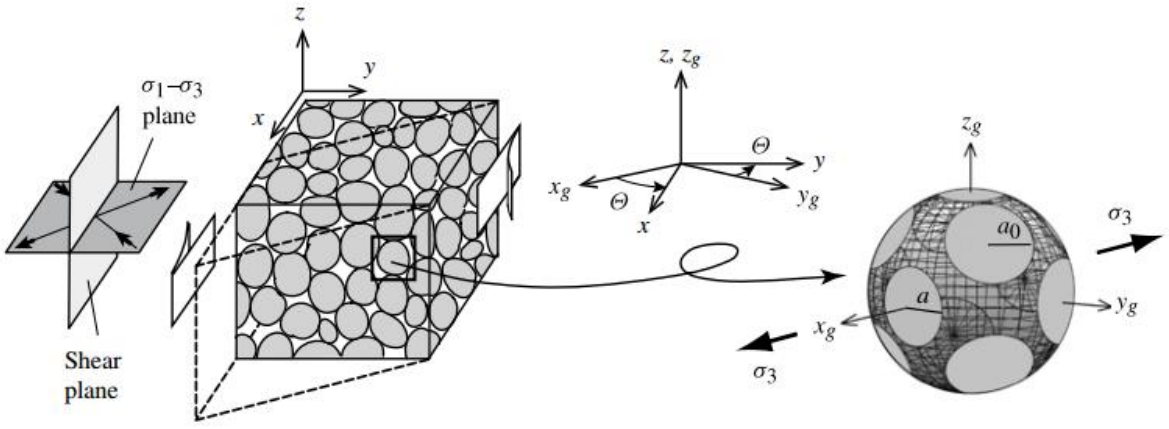

Figure 42: Each matrix grain is assumed to have 14 circular contact faces of radius a. Collections of contiguous grains and the directions of principle stress are defined general continuum coordinates (x, y, z) , while the grain-scale anisotropy is described using a localized grain coordinate system (x_g, y_g, z_g). These coordinate systems are related through the anisotropy angle Θ. This figure is taken from Takei and Katz (2013).

Two coordinate systems exist in this model: general Cartesian coordinates (x, y, z), and grain-centered Cartesian coordinates (x_g, y_g, z_g). These coordinate systems are related by the angle Θ, which is the same as the anisotropy angle from section 2.4. As shown in Figure 42, the x_g axis is assumed to be parallel to the direction of maximum tension (σ_3). Grain-scale anisotropy produced by stress is introduced as localized a reduction in the circular contact face radius in the x_g direction (Takei and Katz, 2013).

The initial form of the anisotropic viscosity tensor that results from this contiguity model is given by:

$$C_{ijkl} = \xi\delta_{ij}\delta_{kl} + \eta\left(\delta_{ik}\delta_{jl} + \delta_{il}\delta_{jk} - \frac{2}{3}\delta_{ij}\delta_{kl}\right) - \Delta\delta_{ix_g}\delta_{jx_g}\delta_{kx_g}\delta_{lx_g}. \quad \text{(A2.1)}$$

In equation (A2.1), the various δ_{ij} are Kronecker-deltas, while ξ is the matrix bulk viscosity and η is the porosity-weakening matrix shear viscosity given by $\eta = \eta_0 e^{\lambda(\phi-\phi_0)}$. In the final term in

this equation, Δ accounts for the viscosity decrease in the x_g direction and is related to the matrix shear viscosity via

$$\Delta = \alpha\,\eta. \tag{A2.2}$$

In equation (A2.2), α is the magnitude of the anisotropy as defined earlier in equation (16).

At this point, equation (A2.1) is defined in the grain-centered Cartesian coordinates. In order to translate this result to general Cartesian coordinates, Takei and Katz introduce a rotation matrix defined by

$$a_{ij} = \begin{pmatrix} cos\Theta & -sin\Theta & 0 \\ sin\Theta & cos\Theta & 0 \\ 0 & 0 & 1 \end{pmatrix}, \tag{A2.3}$$

where the rows correspond to general Cartesian coordinates and the columns correspond to the grain-centered coordinates.

Taking into account equation (A2.3) along with the non-dimensionalized parameters presented in equations (9) and (10) and the definition of the porosity-weakening shear viscosity, equation (A2.1) can be re-written as

$$C_{ijkl} = e^{\lambda(\phi-\phi_0)}\left[\left(r_\xi - \tfrac{2}{3}\right)\delta_{ij}\delta_{kl} + \delta_{ik}\delta_{jl} + \delta_{il}\delta_{jk} - \alpha a_{ix_g}a_{jx_g}a_{kx_g}a_{lx_g}\right]. \tag{A2.4}$$

In turn, equation (A2.4) can be written in matrix form as:

$$C_{ijkl} = e^{-\lambda(\phi-\phi_0)}\begin{bmatrix} r_\xi + \frac{4}{3} + \alpha\cos^4\Theta & r_\xi - \frac{2}{3} + \alpha\sin^2 2\Theta & -\alpha\cos^3\Theta\sin\Theta \\ r_\xi - \frac{2}{3} + \alpha\sin^2 2\Theta & r_\xi + \frac{4}{3} + \alpha\sin^4\Theta & -\alpha\cos\Theta\sin^3\Theta \\ -\alpha\cos^3\Theta\sin\Theta & -\alpha\cos\Theta\sin^3\Theta & 1 - \frac{\alpha}{4}\sin^2 2\Theta \end{bmatrix}.$$

Appendix 3: Mid-Ocean Ridge Velocity Field and Strain Rate Tensor Components

The following derivation follows the simple corner flow model presented by Spiegelman and McKenzie (1987). We start with a stream function and velocity field appropriate for a MOR corner flow:

$$\psi = r(Asin\theta - B\theta cos\theta), \tag{A3.1}$$

$$\vec{V} = \frac{1}{r}\frac{\partial \psi}{\partial \theta}\hat{r} - \frac{\partial \psi}{\partial r}\hat{\theta}. \tag{A3.2}$$

In equations (A3.1) and (A3.2), ψ denotes the stream function, $\vec{V}$ is the velocity field, r is the distance from the ridge crest and θ is the angle from the ridge axis while $\hat{r}$ and $\hat{\theta}$ denote unit vectors in the radial and azimuthal directions, respectively. This is illustrated in Figure 43. A and B are constants appropriate for the boundary conditions of a MOR and are given by

$$A = \frac{2sin^2\delta}{\pi - 2\delta - sin2\delta}, \tag{A3.3}$$

$$B = \frac{2}{\pi - 2\delta - sin2\delta}, \tag{A3.4}$$

where δ is the wedge angle. From the $\hat{r}$ component of equation (A3.2), the radial velocity field is defined as

$$V_r = Acos\theta + B\theta sin\theta - Bcos\theta, \tag{A3.5}$$

while the $\hat{\theta}$ component of equation (A3.2) defines azimuthal velocity as

$$V_\theta = B\theta cos\theta - Asin\theta. \tag{A3.6}$$

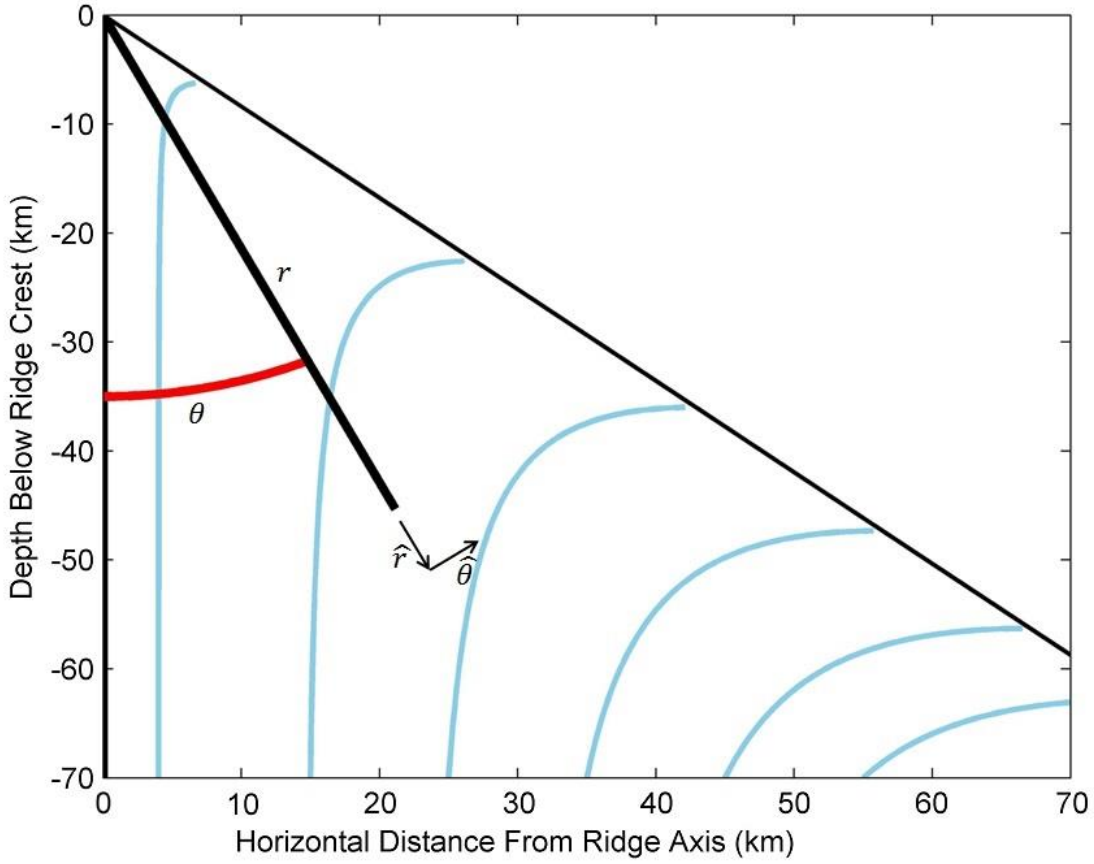

Figure 43: MOR geometry for a slow spreading ridge. Overlaying the streamlines (light blue) is a black line marked r denoting the radial distance from the ridge crest and a red curve marked θ denoting the angle from the ridge axis.

In order to transform equations (A3.5) and (A3.6) from polar to Cartesian coordinates, we define a position row vector $\vec{\rho} = (rsin\theta, \quad -rcos\theta)$. Using this position vector we can define a transformation from Polar to Cartesian coordinates as

$$\begin{bmatrix} U \\ V \end{bmatrix} = M^{-1} \begin{bmatrix} V_r \\ V_\theta \end{bmatrix}, \tag{A3.7}$$

where matrix M is the transformation matrix for a mapping from Cartesian to Polar coordinates. M is defined as

$$M = \begin{pmatrix} \hat{e}_r \\ \hat{e}_\theta \end{pmatrix}, \tag{A3.8}$$

where $\hat{e}_r$ and $\hat{e}_\theta$ are the normalized radial and azimuthal unit vectors, respectively. Inserting the definition of these unit vectors into equation (A3.8) yields

$$M = \begin{pmatrix} \frac{\partial \vec{\rho}}{\partial r} \cdot \frac{1}{\left\| \frac{\partial \vec{\rho}}{\partial r} \right\|} \\ \frac{\partial \vec{\rho}}{\partial \theta} \cdot \frac{1}{\left\| \frac{\partial \vec{\rho}}{\partial \theta} \right\|} \end{pmatrix} = \begin{pmatrix} sin\theta & -cos\theta \\ cos\theta & sin\theta \end{pmatrix}. \quad \text{(A3.9)}$$

Since M is an orthogonal matrix, $M^{-1} = M^T$. This implies that

$$M^{-1} = \begin{pmatrix} sin\theta & cos\theta \\ -cos\theta & sin\theta \end{pmatrix}. \quad \text{(A3.10)}$$

In our geometry, clockwise rotation is assumed to be positive, resulting in a conversion between polar and Cartesian coordinate variables defined by

$$\begin{cases} \theta = arctan(\frac{x}{y}) \\ r = \sqrt{x^2 + y^2}. \\ x = rsin\theta \\ y = rcos\theta \end{cases} \quad \text{(A3.11)}$$

Substituting (A3.5), (A3.6), (A3.10), and (A3.11) into (A3.7) we can then define the velocity field in Cartesian coordinates as

$$U = B\left(tan^{-1}\left(\frac{x}{y}\right) - \left(\frac{xy}{x^2 + y^2}\right)\right), \quad \text{(A3.12)}$$

$$V = -A + B\left(\frac{x^2}{x^2 + y^2}\right), \quad \text{(A3.13)}$$

where U corresponds to the horizontal component of the velocity field and V corresponds to the vertical component of the velocity field.

The first derivatives with respect to x and y of both equations (A3.11) and (A3.12) are necessary for defining the components of the strain-rate tensor for the MOR corner flow which is given by

$$\dot{\varepsilon}_{ij} = \begin{pmatrix} \frac{\partial U}{\partial x} & \frac{1}{2}\left(\frac{\partial U}{\partial y} + \frac{dV}{dx}\right) \\ \frac{1}{2}\left(\frac{\partial U}{\partial y} + \frac{dV}{dx}\right) & \frac{\partial V}{\partial y} \end{pmatrix}. \quad \text{(A3.13)}$$

Term $\dot{\varepsilon}_{11}$ can be found by taking the derivative with respect to x of equation (A3.12):

$$\frac{\partial U}{\partial x} = \frac{2Bx^2y}{(x^2 + y^2)^2}. \quad \text{(A3.16)}$$

Similarly, the other velocity derivatives are given by:

$$\frac{\partial U}{\partial y} = \frac{-2Bx^3}{(x^2+y^2)^2}, \tag{A3.17}$$

$$\frac{\partial V}{\partial x} = \frac{2Bxy^2}{(x^2+y^2)^2}, \tag{A3.18}$$

$$\frac{\partial V}{\partial y} = \frac{-2Bx^2y}{(x^2+y^2)^2}. \tag{A3.19}$$

Substituting equations (A3.16) through (A3.19) into (A3.13), the strain rate tensor for a MOR corner flow is then given by

$$\dot{\varepsilon}_{ij} = \begin{pmatrix} \frac{2Bx^2y}{(x^2+y^2)^2} & \frac{-Bx^3}{(x^2+y^2)^2} + \frac{Bxy^2}{(x^2+y^2)^2} \\ \frac{-Bx^3}{(x^2+y^2)^2} + \frac{Bxy^2}{(x^2+y^2)^2} & \frac{-2Bx^2y}{(x^2+y^2)^2} \end{pmatrix}. \tag{A3.20}$$

Appendix 4: Derivation of Linear Analysis ODEs

Begin with the following equations

$$\frac{\partial \phi}{\partial t} + \vec{U} \cdot \nabla \phi = (1 - \phi) \nabla \cdot \vec{U}, \tag{A4.1}$$

$$\phi = \phi_0 + \Delta \phi exp\left(i\big(k_x(t)x + k_y(t)y\big) + s(t)\right), \tag{A4.2}$$

where equation (A4.1) describes the mass balance for the system and equation (A4.2) is the plane wave porosity perturbation. In equation (A4.2), $\Delta\phi \ll \phi_0$. The two-component velocity field $\vec{U}$ is decomposed into zeroth and first order terms in $\Delta\phi$ as:

$$\vec{U} = [U_b + U_1\ , V_b + V_1]. \tag{A4.3}$$

In equation (A4.3), the b subscripts denote the background velocity terms while the terms subscripted with a one denote the first-order variation from the background velocity. In keeping with Gebhardt and Butler (2016), the first order perturbations of the velocity field are assumed to be proportional to the porosity perturbation in equation (A4.2). This proportional relationship is expressed as

$$\begin{cases} U_1 = -i\tilde{U}\phi_1 \\ V_1 = -i\tilde{V}\phi_1 \end{cases}, \tag{A4.4}$$

where ϕ_1 is the plane wave term from equation (A4.2).

Equation (A4.1) can be re-written by expanding the derivatives as

$$\frac{\partial \phi}{\partial t} + U\frac{\partial \phi}{\partial x} + V\frac{\partial \phi}{\partial y} = (1 - \phi)\left(\frac{\partial U}{\partial x} + \frac{\partial V}{\partial y}\right). \tag{A4.5}$$

Substituting (A4.2), (A4.3), and (A4.4) into (A4.5) yields:

$$\begin{aligned} &\phi_1\left(i\frac{\partial k_x}{\partial t}x + i\frac{\partial k_y}{\partial t}y + \frac{\partial s}{\partial t}\right) + i\phi_1 k_x(U_b - i\tilde{U}\phi_1) + i\phi_1 k_y(V_b - i\tilde{V}\phi_1) \\ &\qquad = (1 - \phi_0 - \phi_1)\left(\frac{\partial(U_b + \tilde{U}\phi_1)}{\partial x} + \frac{\partial(V_b + \tilde{V}\phi_1)}{\partial y}\right). \end{aligned} \tag{A4.6}$$

To first order, equation (A4.6) becomes

$$\left(i\frac{\partial k_x}{\partial t}x + i\frac{\partial k_y}{\partial t}y + \frac{\partial s}{\partial t}\right) + ik_xU_b + ik_yV_b = (1 - \phi_0)\big(k_x\tilde{U} + k_y\tilde{V}\big). \tag{A4.7}$$

The zeroth order velocity field terms are defined as

$$U_b = \frac{\partial U}{\partial x}x + \frac{\partial U}{\partial y}y, \tag{A4.8}$$

$$V_b = \frac{\partial V}{\partial x}x + \frac{\partial V}{\partial y}y. \tag{A4.9}$$

Substituting the expressions in equations (A4.8) and (A4.9) into (A4.7) yields

$$\left(i\frac{\partial k_x}{\partial t}x + i\frac{\partial k_y}{\partial t}y + \frac{\partial s}{\partial t}\right) + ik_x\left(\frac{\partial U}{\partial x}x + \frac{\partial U}{\partial y}y\right) + ik_y\left(\frac{\partial V}{\partial x}x + \frac{\partial V}{\partial y}y\right) \tag{A4.7}$$
$$= (1-\phi_0)\left(k_x\tilde{U} + k_y\tilde{V}\right).$$

At this point, gather the coefficients for x and y to produce the pair of ODEs describing the wavenumber evolution with time:

$$\frac{\partial k_x}{\partial t} = -\frac{\partial U}{\partial x}k_x - \frac{\partial V}{\partial x}k_y, \tag{A4.8}$$

$$\frac{\partial k_y}{\partial t} = -\frac{\partial U}{\partial y}k_x - \frac{\partial V}{\partial y}k_y. \tag{A4.9}$$

The remaining terms from (A4.7) form the ODE defining the perturbation amplitude growth rate in time:

$$\frac{\partial s}{\partial t} = (1-\phi_0)\left(k_x\tilde{U} + k_y\tilde{V}\right). \tag{A4.10}$$

Together, (A4.8), (A4.9) and (A4.10) form the basis of the linear analysis.

Appendix 5: Isotropic, Strain Rate Dependent Growth Rate Derivation

As with the case of the isotropic, strain rate independent growth rate, begin with the force balance equations for the two fluid phases:

$$\nabla \cdot \overrightarrow{U'} = \nabla \cdot [(\nabla P')], \tag{A5.1}$$

$$\nabla P'(1 + \xi') = \nabla \cdot \boldsymbol{\sigma}'. \tag{A5.2}$$

Applying a Fourier transform to equation (A5.1) and writing the result to first order yields the same result seen in equation (23),

$$ik_x\tilde{U} + ik_y\tilde{V} = -\left(k_x^2 + k_y^2\right)\tilde{P}. \tag{A3.3}$$

Expanding the operators in equation (A5.2) also yields the same two equations seen earlier in equations (24) and (25),

$$\frac{\partial}{\partial x}\left[-P(\xi + 1) + (\xi + 1)\eta\frac{\partial U}{\partial x} + (\xi - 1)\eta\frac{\partial V}{\partial y}\right] + \frac{\partial}{\partial y}\left[\eta\left(\frac{\partial U}{\partial y} + \frac{\partial V}{\partial x}\right)\right] = 0, \tag{A5.4}$$

$$\frac{\partial}{\partial y}\left[-P(\xi + 1) + (\xi - 1)\eta\frac{\partial U}{\partial x} + (\xi + 1)\eta\frac{\partial V}{\partial y}\right] + \frac{\partial}{\partial x}\left[\eta\left(\frac{\partial U}{\partial y} + \frac{\partial V}{\partial x}\right)\right] = 0. \tag{A5.5}$$

The most significant difference in this growth rate derivation comes from the matrix rheology law. The isotropic, strain rate dependent matrix shear viscosity is defined as

$$\eta = exp\left(\frac{\lambda(\phi - \phi_0)}{n_v}\right)\dot{\epsilon}_{II}^{\frac{(1-n_v)}{n_v}}. \tag{A5.6}$$

The form of equation (A5.6) requires that both the exponential porosity and the strain rate portions be linearized. Applying a Taylor series expansions ϕ about ϕ_0, the porosity dependent portion of equation (A5.6) can be re-written to first order as

$$exp\left(\frac{\lambda(\phi - \phi_0)}{n_v}\right) \approx 1 + \frac{\lambda\phi'}{n_v}, \tag{A5.7}$$

which is identical to the first order decomposition found earlier in equation (27). The strain rate portion of equation (A5.6) also requires linearization. The second invariant of the strain rate tensor term in (A5.6) is defined as

$$\dot{\epsilon}_{II}^{\frac{(1-n_v)}{n_v}} = (\dot{\epsilon}_{ij}\dot{\epsilon}_{ij})^{\frac{(1-n_v)}{2n_v}}. \tag{A5.8}$$

Written to first order, equation (A5.8) becomes

$$\dot{\epsilon}_{II}^{\frac{(1-n_v)}{n_v}} = \left(2\frac{\partial U_b}{\partial x}^2 + \frac{1}{2}\left(\frac{\partial U_b}{\partial y} + \frac{\partial V_b}{\partial x}\right)^2\right)^{\frac{(1-n_v)}{2n_v}} \times \left(1 + \frac{2\frac{\partial U_b}{\partial x}\left(\frac{\partial U_1}{\partial x} + \frac{\partial V_1}{\partial y}\right) + \left(\frac{\partial U_b}{\partial y} + \frac{\partial V_b}{\partial x}\right)\left(\frac{\partial U_1}{\partial y} + \frac{\partial V_1}{\partial x}\right)}{2\frac{\partial U_b}{\partial x}^2 + \frac{1}{2}\left(\frac{\partial U_b}{\partial y} + \frac{\partial V_b}{\partial x}\right)^2}\right)^{\frac{(1-n_v)}{2n_v}}. \tag{A5.9}$$

Applying a binomial approximation to the last term of equation (A5.9) leads to the following linearization for the second invariant of the strain-rate tensor:

$$\left(1 + \frac{2\frac{\partial U_b}{\partial x}\left(\frac{\partial U_1}{\partial x} + \frac{\partial V_1}{\partial y}\right) + \left(\frac{\partial U_b}{\partial y} + \frac{\partial V_b}{\partial x}\right)\left(\frac{\partial U_1}{\partial y} + \frac{\partial V_1}{\partial x}\right)}{2\frac{\partial U_b}{\partial x}^2 + \frac{1}{2}\left(\frac{\partial U_b}{\partial y} + \frac{\partial V_b}{\partial x}\right)^2}\right)^{\frac{(1-n_v)}{2n_v}} \approx 1 + \frac{(1-n_v)}{2n_v}\left[\frac{2\frac{\partial U_b}{\partial x}\left(\frac{\partial U_1}{\partial x} + \frac{\partial V_1}{\partial y}\right) + \left(\frac{\partial U_b}{\partial y} + \frac{\partial V_b}{\partial x}\right)\left(\frac{\partial U_1}{\partial y} + \frac{\partial V_1}{\partial x}\right)}{2\frac{\partial U_b}{\partial x}^2 + \frac{1}{2}\left(\frac{\partial U_b}{\partial y} + \frac{\partial V_b}{\partial x}\right)^2}\right]. \tag{A5.10}$$

Multiplying equations (A5.7) and (A5.10) results in

$$\eta = 1 + \frac{\lambda\phi'}{n_v} + \frac{(1-n_v)}{2n_v}\left[\frac{2\frac{\partial U_b}{\partial x}\left(\frac{\partial U_1}{\partial x} + \frac{\partial V_1}{\partial y}\right) + \left(\frac{\partial U_b}{\partial y} + \frac{\partial V_b}{\partial x}\right)\left(\frac{\partial U_1}{\partial y} + \frac{\partial V_1}{\partial x}\right)}{2\frac{\partial U_b}{\partial x}^2 + \frac{1}{2}\left(\frac{\partial U_b}{\partial y} + \frac{\partial V_b}{\partial x}\right)^2}\right] \tag{A5.11}$$

as the linear approximation for the matrix shear viscosity in the case of isotropic, strain rate dependent rheology.

Expanding the derivatives in equations (A5.4) and (A5.5) yields

$$-\frac{\partial P}{\partial x}(\xi+1) + (\xi+1)\frac{\partial \eta}{\partial x}\frac{\partial U}{\partial x} + (\xi+1)\eta\frac{\partial^2 U}{\partial x^2} + (\xi-1)\frac{\partial \eta}{\partial x}\frac{\partial V}{\partial y} + (\xi-1)\eta\frac{\partial^2 V}{\partial y \partial x} + \frac{\partial \eta}{\partial y}\left(\frac{\partial U}{\partial y} + \frac{\partial V}{\partial x}\right) + \eta\left(\frac{\partial^2 U}{\partial y^2} + \frac{\partial^2 V}{\partial x \partial y}\right) = 0, \tag{A5.12}$$

$$-\frac{\partial P}{\partial y}(\xi+1) + (\xi-1)\frac{\partial \eta}{\partial y}\frac{\partial U}{\partial x} + (\xi-1)\eta\frac{\partial^2 U}{\partial x \partial y} + (\xi+1)\frac{\partial \eta}{\partial y}\frac{\partial V}{\partial y} + (\xi+1)\eta\frac{\partial^2 V}{\partial y^2} + \frac{\partial \eta}{\partial x}\left(\frac{\partial U}{\partial y} + \frac{\partial V}{\partial x}\right) + \eta\left(\frac{\partial^2 U}{\partial y \partial x} + \frac{\partial^2 V}{\partial x^2}\right) = 0. \tag{A5.13}$$

Writing equations (A5.12) and (A5.13) to first order results in

$$0 = -\frac{\partial P}{\partial x}(\xi+1) + \frac{2\lambda}{n_v}\frac{\partial U_b}{\partial x}\frac{\partial \phi}{\partial x} + \frac{\lambda}{n_v}\left(\frac{\partial U_b}{\partial y}+\frac{\partial V_b}{\partial x}\right)\frac{\partial \phi}{\partial y} + \left(2\Psi\frac{\partial U_b}{\partial x}^2 + \xi + 1\right)\frac{\partial^2 U}{\partial x^2}$$
$$+\left(4\Psi\frac{\partial U_b}{\partial x}\left(\frac{\partial U_b}{\partial y}+\frac{\partial V_b}{\partial x}\right)\right)\frac{\partial^2 U}{\partial y \partial x} + \left(\Psi\left(\frac{\partial U_b}{\partial y}+\frac{\partial V_b}{\partial x}\right)^2 + 1\right)\frac{\partial^2 U}{\partial y^2} \quad \text{(A5.14)}$$
$$+\left(2\Psi\frac{\partial U_b}{\partial x}\left(\frac{\partial U_b}{\partial y}+\frac{\partial V_b}{\partial x}\right)\right)\left(\frac{\partial^2 V}{\partial x^2}+\frac{\partial^2 V}{\partial y^2}\right) + \left(2\Psi\frac{\partial U_b}{\partial x}^2 + \Psi\left(\frac{\partial U_b}{\partial y}+\frac{\partial V_b}{\partial x}\right)^2 + \xi\right)\frac{\partial^2 V}{\partial x \partial y},$$

$$0 = -\frac{\partial P}{\partial y}(\xi+1) - \frac{2\lambda}{n_v}\frac{\partial U_b}{\partial x}\frac{\partial \phi}{\partial y} + \frac{\lambda}{n_v}\left(\frac{\partial U_b}{\partial y}+\frac{\partial V_b}{\partial x}\right)\frac{\partial \phi}{\partial x}$$
$$+\left(2\Psi\frac{\partial U_b}{\partial x}\left(\frac{\partial U_b}{\partial y}+\frac{\partial V_b}{\partial x}\right)\right)\left(\frac{\partial^2 U}{\partial x^2}-\frac{\partial^2 U}{\partial y^2}\right) + \left(2\Psi\frac{\partial U_b}{\partial x}^2 + \Psi\left(\frac{\partial U_b}{\partial y}+\frac{\partial V_b}{\partial x}\right)^2 + \xi\right)\frac{\partial^2 U}{\partial y \partial x} \quad \text{(A5.15)}$$
$$+\left(\Psi\left(\frac{\partial U_b}{\partial y}+\frac{\partial V_b}{\partial x}\right)^2 + 1\right)\frac{\partial^2 V}{\partial x^2} + \left(2\Psi\frac{\partial U_b}{\partial x}^2 + \xi + 1\right)\frac{\partial^2 V}{\partial y^2},$$

where $\Psi = \left(\frac{1-n_v}{2n_v}\right)\left[\frac{1}{2\Psi\frac{\partial U_b}{\partial x}^2 + \frac{1}{2}\left(\frac{\partial U_b}{\partial y}+\frac{\partial V_b}{\partial x}\right)^2}\right]$.

Applying a Fourier transform to equations (A5.14) and (A5.15) transforms the spatial derivatives into wavenumbers. These transformed equations, along with equation (A5.3), yield the forms of the mass balance equations needed to derive the growth rate. Making the substitution $\widetilde{F}' = i\tilde{F}$ to these transformed equations yields the following matrix multiplication expression

$$\begin{bmatrix} k_x(\xi+1) & -4\Psi\frac{\partial U_b}{\partial x}\left(\frac{\partial U_b}{\partial y}+\frac{\partial V_b}{\partial x}\right)k_x k_y - k_x^2\left(4\Psi\frac{\partial U_b}{\partial x}^2+\xi+1\right) - k_y^2\left(\Psi\left(\frac{\partial U_b}{\partial y}+\frac{\partial V_b}{\partial x}\right)^2+1\right) & -\left(2\Psi\frac{\partial U_b}{\partial x}\left(\frac{\partial U_b}{\partial y}+\frac{\partial V_b}{\partial x}\right)\right)(k_x^2+k_y^2) - k_x k_y\left(-4\Psi\frac{\partial U_b}{\partial x}^2+\Psi\left(\frac{\partial U_b}{\partial y}+\frac{\partial V_b}{\partial x}\right)^2+\xi\right) \\ k_y(\xi+1) & -\left(2\Psi\frac{\partial U_b}{\partial x}\left(\frac{\partial U_b}{\partial y}+\frac{\partial V_b}{\partial x}\right)\right)(k_x^2+k_y^2) - k_x k_y\left(-4\Psi\frac{\partial U_b}{\partial x}^2+\Psi\left(\frac{\partial U_b}{\partial y}+\frac{\partial V_b}{\partial x}\right)^2+\xi\right) & -k_y^2\left(4\Psi\frac{\partial U_b}{\partial x}^2+\xi+1\right) - k_x^2\left(\Psi\left(\frac{\partial U_b}{\partial y}+\frac{\partial V_b}{\partial x}\right)^2+1\right) \\ k_x^2+k_y^2 & k_x & k_y \end{bmatrix}$$
$$\times\begin{bmatrix}\widetilde{P}' \\ \widetilde{U}' \\ \widetilde{V}'\end{bmatrix} = \begin{bmatrix}\frac{\lambda}{n_v}\left(2\frac{\partial U_b}{\partial x}k_x + \left(\frac{\partial U_b}{\partial y}+\frac{\partial V_b}{\partial x}\right)k_y\right) \\ \frac{\lambda}{n_v}\left(\left(\frac{\partial U_b}{\partial y}+\frac{\partial V_b}{\partial x}\right)k_x - 2\frac{\partial U_b}{\partial x}k_y\right) \\ 0\end{bmatrix}. \quad \text{(A5.16)}$$

The matrix in (A5.16) can be inverted in Mathematica to solve for $\widetilde{U}'$ and $\tilde{V}'$giving the following expression for the growth rate:

$$
\begin{aligned}
&\frac{ds}{dt} \\
&= \Bigg\{ \lambda(1-\phi_0)\left(4\frac{\partial U_b}{\partial x}^2 + \left(\frac{\partial U_b}{\partial y}+\frac{\partial V_b}{\partial x}\right)^2\right)^2 \left(-2\left(k_x^2+k_y^2\right)^2\right)\Bigg(\left(\frac{\partial U_b}{\partial y}+\frac{\partial V_b}{\partial x}\right)k_x k_y \\
&+ \frac{\partial U_b}{\partial x}\left(k_x-k_y\right)\left(k_x+k_y\right)\Bigg) \\
&+ \frac{\left[4\frac{\partial U_b}{\partial x}\left(\frac{\partial U_b}{\partial y}+\frac{\partial V_b}{\partial x}\right)k_y\left(k_x^2+k_y^2\right)\left(-2\frac{\partial U_b}{\partial x}k_x^3+\left(\frac{\partial U_b}{\partial y}+\frac{\partial V_b}{\partial x}\right)k_y^3\right)\right]}{4\frac{\partial U_b}{\partial x}^2+\left(\frac{\partial U_b}{\partial y}+\frac{\partial V_b}{\partial x}\right)^2}\frac{1-n_v}{n_v}\Bigg\} \\
\div \Bigg\{ & n_v\Bigg(\left(4\frac{\partial U_b}{\partial x}^2+\left(\frac{\partial U_b}{\partial y}+\frac{\partial V_b}{\partial x}\right)^2\right)\left(1+k_x^2+k_y^2\right)(\xi \\
&+1)\Bigg[\left(\left(k_x^2+k_y^2\right)^2\left(4\frac{\partial U_b}{\partial x}^2+\left(\frac{\partial U_b}{\partial y}+\frac{\partial V_b}{\partial x}\right)^2\right)\right. \\
&+\frac{1-n_v}{n_v}\Bigg(-2k_x^2k_y^2\left(-8\frac{\partial U_b}{\partial x}^2+\left(\frac{\partial U_b}{\partial y}+\frac{\partial V_b}{\partial x}\right)^2\right)-4\frac{\partial U_b}{\partial x}k_x^3k_y\left(\frac{\partial U_b}{\partial y}+\frac{\partial V_b}{\partial x}\right) \\
&\left.+\left(k_x^4+k_y^4\right)\left(\frac{\partial U_b}{\partial y}+\frac{\partial V_b}{\partial x}\right)^2\Bigg)\Bigg] \\
&+4\frac{1-n_v}{n_v}\left(k_x^2+k_y^2\right)\Bigg[\left(4\frac{\partial U_b}{\partial x}^2+\left(\frac{\partial U_b}{\partial y}+\frac{\partial V_b}{\partial x}\right)^2\right)\Bigg(\frac{\partial U_b}{\partial x}^2\left(k_x-k_y\right)^2 \\
&+\frac{\partial U_b}{\partial x}\left(\frac{\partial U_b}{\partial y}+\frac{\partial V_b}{\partial x}\right)k_xk_y\left(2k_x^2+k_y^2\right)+k_x^2k_y^2\left(\frac{\partial U_b}{\partial y}+\frac{\partial V_b}{\partial x}\right)^2\Bigg) \\
&-\frac{\partial U_b}{\partial x}\left(\frac{\partial U_b}{\partial y}+\frac{\partial V_b}{\partial x}\right)k_xk_y\frac{1-n_v}{n_v}\Bigg(k_y^2\left(\frac{\partial U_b}{\partial y}+\frac{\partial V_b}{\partial x}\right)^2 \\
&\left.-4\frac{\partial U_b}{\partial x}^2\left(k_x^2+2k_y^2\right)\Bigg)\Bigg]\Bigg)\Bigg\}
\end{aligned}
\tag{A5.17}
$$

Setting $n_v = 1$ reduces (A5.17) to the growth rate appropriate for an isotropic, strain rate independent matrix shear vicosity, as given in equation (34).

Appendix 6: Anisotropic, Strain Rate Independent Growth Rate Derivation

The growth rate for the case of anisotropic, strain rate dependent matrix shear viscosity follows the same process as with the previous two growth rate derivations: the force balance equations are expanded to first order and Fourier transformed so as to solve for the coefficients of the amplitude of the horizontal and vertical components of the velocity perturbation. However, different forms of the force balance equations, as given in Takei and Katz (2013), are used as a starting point for this derivation. These equations are given by

$$\nabla \cdot \boldsymbol{V} = \frac{R^2}{r_\xi + \frac{4}{3}} \nabla \cdot [\nabla P], \tag{A6.1}$$

$$\frac{\partial P}{\partial x_i} = \frac{\partial}{\partial x_j}\left[C_{ijkl}\dot{\epsilon}_{kl}\right]. \tag{A6.2}$$

In these equations $\boldsymbol{V}$ is the velocity field of the matrix phase consisting of both horizontal and vertical components, P is the nondimensional liquid pressure, C_{ijkl} is the anisotropic viscosity tensor defined in equation (15), and $\dot{\epsilon}_{kl}$ is the strain rate tensor. The variable r_ξ is the constant of proportionality that relates the matrix bulk viscosity to the matrix shear viscosity and is taken to be 5/3 (Takei and Holtzman, 2009). R is the ratio of compaction length to characteristic dimension of the domain, which in our contribution are the same, making R = 1.

Applying a Fourier transform and first order expansion to equation (A6.1) yields a result very similar to the derivations of the other growth rates

$$ik_x\tilde{U} + ik_y\tilde{V} = -\frac{\left(k_x^2 + k_y^2\right)}{r_\xi + \frac{4}{3}}\tilde{P}. \tag{A6.3}$$

Expanding equation (A6.2) yields two equations,

$$\begin{aligned}\frac{\partial P}{\partial x} = \frac{\partial}{\partial x}\left[C_{xxxx}\dot{\epsilon}_{xx} + 2C_{xxxy}\dot{\epsilon}_{xy} + C_{xxyy}\dot{\epsilon}_{yy}\right] \\ + \frac{\partial}{\partial y}\left[C_{xyxx}\dot{\epsilon}_{xx} + 2C_{xyxy}\dot{\epsilon}_{xy} + C_{xyyy}\dot{\epsilon}_{yy}\right],\end{aligned} \tag{A6.4}$$

$$\frac{\partial P}{\partial y} = \frac{\partial}{\partial x}\left[C_{xyxx}\dot{\epsilon}_{xx} + 2C_{xyxy}\dot{\epsilon}_{xy} + C_{xyyy}\dot{\epsilon}_{yy}\right] + \frac{\partial}{\partial y}\left[C_{yyxx}\dot{\epsilon}_{xx} + 2C_{yyxy}\dot{\epsilon}_{xy} + C_{yyyy}\dot{\epsilon}_{yy}\right]. \tag{A6.5}$$

Substituting values from both the anisotropic viscosity tensor and the strain rate tensor into equation (A6.5) yields

$$\begin{aligned}\frac{\partial P}{\partial x} = {} & \frac{\partial}{\partial x} e^{-\lambda(\phi-\phi_0)}\left[\left(r_\xi + \frac{4}{3} + \alpha\cos^4\Theta\right)\frac{\partial U}{\partial x} - \alpha\cos^3\Theta\sin\Theta\left(\frac{\partial U}{\partial y} + \frac{\partial V}{\partial x}\right)\right. \\ & \left. + \left(r_\xi - \frac{2}{3} + \alpha\sin^2 2\Theta\right)\frac{\partial V}{\partial y}\right] \\ & + \frac{\partial}{\partial y} e^{-\lambda(\phi-\phi_0)}\left[-\alpha\cos^3\Theta\sin\Theta\frac{\partial U}{\partial x} + \left(1 - \frac{\alpha}{4}\sin^2 2\Theta\right)\left(\frac{\partial U}{\partial y} + \frac{\partial V}{\partial x}\right)\right. \\ & \left. - \alpha\cos\Theta\sin^3\Theta\frac{\partial V}{\partial y}\right],\end{aligned} \tag{A6.6}$$

$$\begin{aligned}\frac{\partial P}{\partial y} = {} & \frac{\partial}{\partial x} e^{-\lambda(\phi-\phi_0)}\left[-\alpha\cos^3\Theta\sin\Theta\frac{\partial U}{\partial x} + \left(1 - \frac{\alpha}{4}\sin^2 2\Theta\right)\left(\frac{\partial U}{\partial y} + \frac{\partial V}{\partial x}\right)\right. \\ & \left. - \alpha\cos\Theta\sin^3\Theta\frac{\partial V}{\partial y}\right] \\ & + \frac{\partial}{\partial y} e^{-\lambda(\phi-\phi_0)}\left[\left(r_\xi - \frac{2}{3} + \alpha\sin^2 2\Theta\right)\frac{\partial U}{\partial x}\right. \\ & \left. - \alpha\cos\Theta\sin^3\Theta\left(\frac{\partial U}{\partial y} + \frac{\partial V}{\partial x}\right) + \left(r_\xi + \frac{4}{3} + \alpha\sin^4\Theta\right)\frac{\partial V}{\partial y}\right].\end{aligned} \tag{A6.7}$$

The porosity weakening portion of the matrix viscosity and the components of the strain rate use the same first order decompositions as the previous growth rate derivations. Knowing this, equations (A6.6) and (A6.7) can be written to first order as

$$
\begin{aligned}
\frac{\partial P}{\partial x} = \lambda \frac{\partial \phi'}{\partial x}\Bigg[&\left(r_\xi + \frac{4}{3} + \alpha\cos^4\Theta\right)\frac{\partial U_b}{\partial x} - \alpha\cos^3\Theta\sin\Theta\left(\frac{\partial U_b}{\partial y} + \frac{\partial V_b}{\partial x}\right) \\
&+ \left(r_\xi - \frac{2}{3} + \alpha\sin^2 2\Theta\right)\frac{\partial V_b}{\partial y}\Bigg] \\
&+ \Bigg[\left(r_\xi + \frac{4}{3} + \alpha\cos^4\Theta\right)\frac{\partial^2 U_1}{\partial x^2} - \alpha\cos^3\Theta\sin\Theta\left(\frac{\partial^2 U_1}{\partial y\partial x} + \frac{\partial^2 V_1}{\partial x^2}\right) \\
&+ \left(r_\xi - \frac{2}{3} + \alpha\sin^2 2\Theta\right)\frac{\partial^2 V_1}{\partial y\partial x}\Bigg] \\
&+ \lambda \frac{\partial \phi'}{\partial y}\Bigg[-\alpha\cos^3\Theta\sin\Theta\frac{\partial U_b}{\partial x} + \left(1 - \frac{\alpha}{4}\sin^2 2\Theta\right)\left(\frac{\partial U_b}{\partial y} + \frac{\partial V_b}{\partial x}\right) \\
&- \alpha\cos\Theta\sin^3\Theta\frac{\partial V_b}{\partial y}\Bigg] \\
&+ \Bigg[-\alpha\cos^3\Theta\sin\Theta\frac{\partial^2 U_1}{\partial x\partial y} + \left(1 - \frac{\alpha}{4}\sin^2 2\Theta\right)\left(\frac{\partial^2 U_1}{\partial y^2} + \frac{\partial^2 V_1}{\partial x\partial y}\right) \\
&- \alpha\cos\Theta\sin^3\Theta\frac{\partial^2 V_1}{\partial y^2}\Bigg],
\end{aligned}
\tag{A6.8}
$$

$$
\begin{aligned}
\frac{\partial P}{\partial y} = \lambda \frac{\partial \phi'}{\partial x}\Bigg[&-\alpha\cos^3\Theta\sin\Theta\frac{\partial U_b}{\partial x} + \left(1 - \frac{\alpha}{4}\sin^2 2\Theta\right)\left(\frac{\partial U_b}{\partial y} + \frac{\partial V_b}{\partial x}\right) \\
&- \alpha\cos\Theta\sin^3\Theta\frac{\partial V_b}{\partial y}\Bigg] \\
&+ \Bigg[-\alpha\cos^3\Theta\sin\Theta\frac{\partial^2 U_1}{\partial x^2} + \left(1 - \frac{\alpha}{4}\sin^2 2\Theta\right)\left(\frac{\partial^2 U_1}{\partial y\partial x} + \frac{\partial^2 V_1}{\partial x^2}\right) \\
&- \alpha\cos\Theta\sin^3\Theta\frac{\partial^2 V_1}{\partial y\partial x}\Bigg] \\
&+ \lambda \frac{\partial \phi'}{\partial y}\Bigg[\left(r_\xi - \frac{2}{3} + \alpha\sin^2 2\Theta\right)\frac{\partial U_b}{\partial x} - \alpha\cos\Theta\sin^3\Theta\left(\frac{\partial U_b}{\partial y} + \frac{\partial V_b}{\partial x}\right) \\
&+ \left(r_\xi + \frac{4}{3} + \alpha\sin^4\Theta\right)\frac{\partial V_b}{\partial y}\Bigg] \\
&+ \Bigg[\left(r_\xi - \frac{2}{3} + \alpha\sin^2 2\Theta\right)\frac{\partial^2 U_1}{\partial x\partial y} - \alpha\cos\Theta\sin^3\Theta\left(\frac{\partial^2 U_1}{\partial y^2} + \frac{\partial^2 V_1}{\partial x\partial y}\right) \\
&+ \left(r_\xi + \frac{4}{3} + \alpha\sin^4\Theta\right)\frac{\partial^2 V_1}{\partial y^2}\Bigg].
\end{aligned}
\tag{A6.9}
$$

Applying a Fourier transform to equations (A6.8) and (A6.9) yields

$$
\begin{aligned}
ik_x\tilde{P} = \; & ik_x\lambda\tilde{\phi}\left[\left(r_\xi + \frac{4}{3} + \alpha\cos^4\Theta\right)\frac{\partial U_b}{\partial x} - \alpha\cos^3\Theta\sin\Theta\left(\frac{\partial U_b}{\partial y} + \frac{\partial V_b}{\partial x}\right)\right. \\
& \left. + \left(r_\xi - \frac{2}{3} + \alpha\sin^2 2\Theta\right)\frac{\partial V_b}{\partial y}\right] \\
& - \left[\left(r_\xi + \frac{4}{3} + \alpha\cos^4\Theta\right)k_x^2\tilde{U} - \alpha\cos^3\Theta\sin\Theta\left(k_yk_x\tilde{U} + k_x^2\tilde{V}\right)\right. \\
& \left. + \left(r_\xi - \frac{2}{3} + \alpha\sin^2 2\Theta\right)k_yk_x\tilde{V}\right] \\
& + ik_y\lambda\tilde{\phi}\left[-\alpha\cos^3\Theta\sin\Theta\frac{\partial U_b}{\partial x} + \left(1 - \frac{\alpha}{4}\sin^2 2\Theta\right)\left(\frac{\partial U_b}{\partial y} + \frac{\partial V_b}{\partial x}\right)\right. \\
& \left. - \alpha\cos\Theta\sin^3\Theta\frac{\partial V_b}{\partial y}\right] \\
& + \left[-\alpha\cos^3\Theta\sin\Theta\,k_yk_x\tilde{U} + \left(1 - \frac{\alpha}{4}\sin^2 2\Theta\right)\left(k_y^2\tilde{U} + k_yk_x\tilde{V}\right)\right. \\
& \left. - \alpha\cos\Theta\sin^3\Theta\,k_y^2\tilde{V}\right],
\end{aligned}
\tag{A6.10}
$$

$$
\begin{aligned}
ik_y\tilde{P} = \; & ik_x\lambda\tilde{\phi}\left[-\alpha\cos^3\Theta\sin\Theta\frac{\partial U_b}{\partial x} + \left(1 - \frac{\alpha}{4}\sin^2 2\Theta\right)\left(\frac{\partial U_b}{\partial y} + \frac{\partial V_b}{\partial x}\right)\right. \\
& \left. - \alpha\cos\Theta\sin^3\Theta\frac{\partial V_b}{\partial y}\right] \\
& + \left[-\alpha\cos^3\Theta\sin\Theta\,k_x^2\tilde{U} + \left(1 - \frac{\alpha}{4}\sin^2 2\Theta\right)\left(k_yk_x\tilde{U} + k_x^2\tilde{V}\right)\right. \\
& \left. - \alpha\cos\Theta\sin^3\Theta\,k_yk_x\tilde{V}\right] \\
& + ik_y\lambda\tilde{\phi}\left[\left(r_\xi - \frac{2}{3} + \alpha\sin^2 2\Theta\right)\frac{\partial U_b}{\partial x} - \alpha\cos\Theta\sin^3\Theta\left(\frac{\partial U_b}{\partial y} + \frac{\partial V_b}{\partial x}\right)\right. \\
& \left. + \left(r_\xi + \frac{4}{3} + \alpha\sin^4\Theta\right)\frac{\partial V_b}{\partial y}\right] \\
& + \left[\left(r_\xi - \frac{2}{3} + \alpha\sin^2 2\Theta\right)k_yk_x\tilde{U} - \alpha\cos\Theta\sin^3\Theta\left(k_y^2\tilde{U} + k_yk_x\tilde{V}\right)\right. \\
& \left. + \left(r_\xi + \frac{4}{3} + \alpha\sin^4\Theta\right)k_y^2\tilde{V}\right].
\end{aligned}
\tag{A6.11}
$$

Applying the substitution $\widetilde{F'} = i\tilde{F}$ to equations (A6.3), (A6.10), and (A6.11), terms can be gathered according to their transformed coefficients and presented in a matrix-vector multiplication expression. This is given by equation (A6.12). A succinct expression for the growth rate was not solved for in the case of this rheology law.

$$
\begin{bmatrix}
-\frac{\left(k_x^2+k_y^2\right)}{r_\xi+\frac{4}{\alpha}} & -k_x & -k_y \\
-k_x & -\left(r_\xi+\frac{4}{3}+\alpha\cos^4\Theta\right)k_x^2+2\alpha\cos^3\Theta\sin\Theta k_y k_x-\left(1-\frac{\alpha}{4}\sin^2 2\Theta\right)k_y^2 & \alpha\cos^3\Theta\sin\Theta k_x^2-\left(r_\xi-\frac{1}{3}-\frac{3}{4}\alpha si\,n^2\,2\Theta\right)k_y k_x+\alpha\cos\Theta\sin^3\Theta k_y^2 \\
-k_y & \alpha\cos^3\Theta\sin\Theta k_x^2-\left(r_\xi-\frac{1}{3}+\frac{3}{4}\alpha\sin^2 2\Theta\right)k_y k_x+\alpha\cos\Theta\sin^3\Theta k_y^2 & -\left(1-\frac{\alpha}{4}\sin^2 2\Theta\right)k_x^2+2\alpha\cos\Theta\sin^3\Theta k_y k_x-\left(r_\xi+\frac{4}{3}+\alpha\sin^4\Theta\right)k_y^2
\end{bmatrix}
\begin{bmatrix}
\widetilde{P'} \\ \widetilde{U'} \\ \widetilde{V'}
\end{bmatrix}
$$

(A6.12)

$$
=
\begin{bmatrix}
0 & -\lambda\left\{k_x\left[\left(r_\xi+\frac{4}{3}+\alpha\cos^4\Theta\right)\frac{\partial U_b}{\partial x}-\alpha\cos^3\Theta\sin\Theta\left(\frac{\partial U_b}{\partial y}+\frac{\partial V_b}{\partial x}\right)+\left(r_\xi-\frac{2}{3}+\alpha\sin^2 2\Theta\right)\frac{\partial V_b}{\partial y}\right]+k_y\left[-\alpha\cos^3\Theta\sin\Theta\frac{\partial U_b}{\partial x}+\left(1-\frac{\alpha}{4}\sin^2 2\Theta\right)\left(\frac{\partial U_b}{\partial y}+\frac{\partial V_b}{\partial x}\right)-\alpha\cos\Theta\sin^3\Theta\frac{\partial V_b}{\partial y}\right]\right\} \\
0 & -\lambda\left\{k_x\left[-\alpha\cos^3\Theta\sin\Theta\frac{\partial U_b}{\partial x}+\left(1-\frac{\alpha}{4}\sin^2 2\Theta\right)\left(\frac{\partial U_b}{\partial y}+\frac{\partial V_b}{\partial x}\right)-\alpha\cos\Theta\sin^3\Theta\left(\frac{\partial U_b}{\partial y}+\frac{\partial V_b}{\partial x}\right)+\left(r_\xi+\frac{4}{3}+\alpha\sin^4\Theta\right)\frac{\partial V_b}{\partial y}\right]\right\}
\end{bmatrix}
$$

Appendix 7: Bands Evolved for Orientation Toward the Ridge Axis

This appendix contains the linear analysis results for the evolution of bands oriented directly toward the ridge axis.

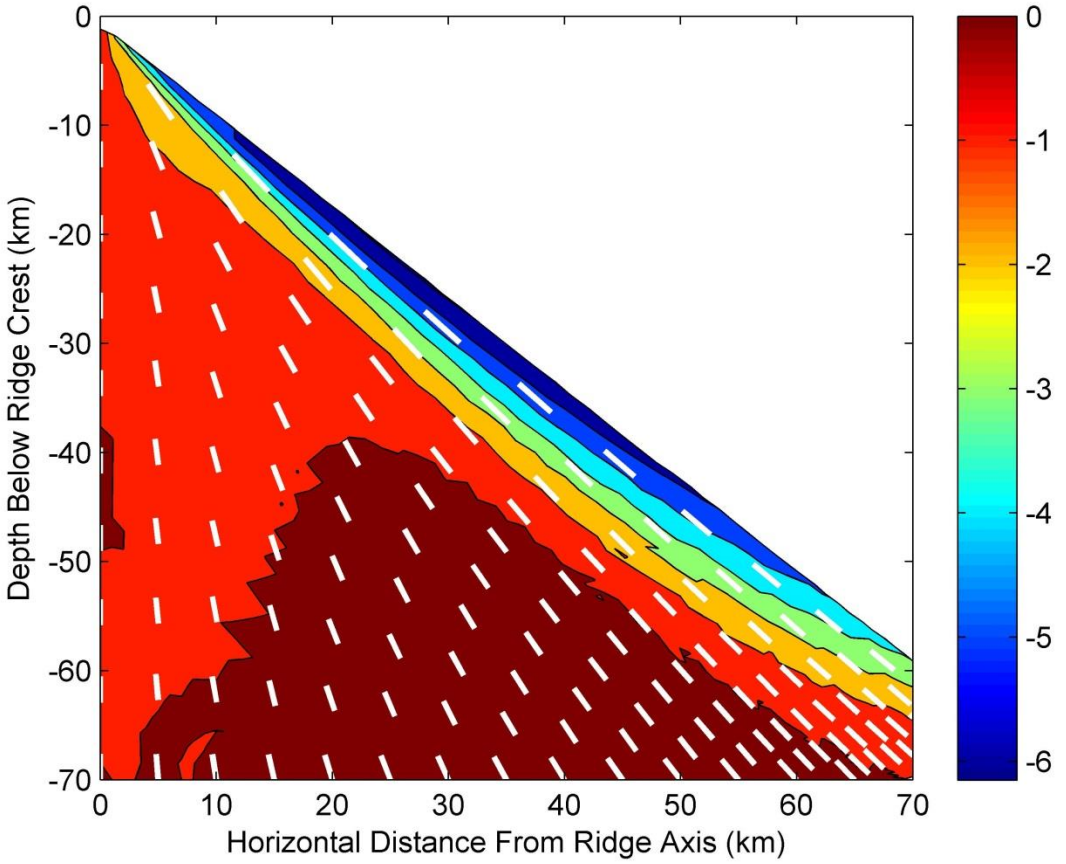

Figure 44: Contour plot of perturbation amplitude for bands evolved for preferential orientation toward the ridge axis for the case of a slow spreading ridge geometry with an isotropic, strain rate dependent $(n_v = 6)$ matrix rheology.

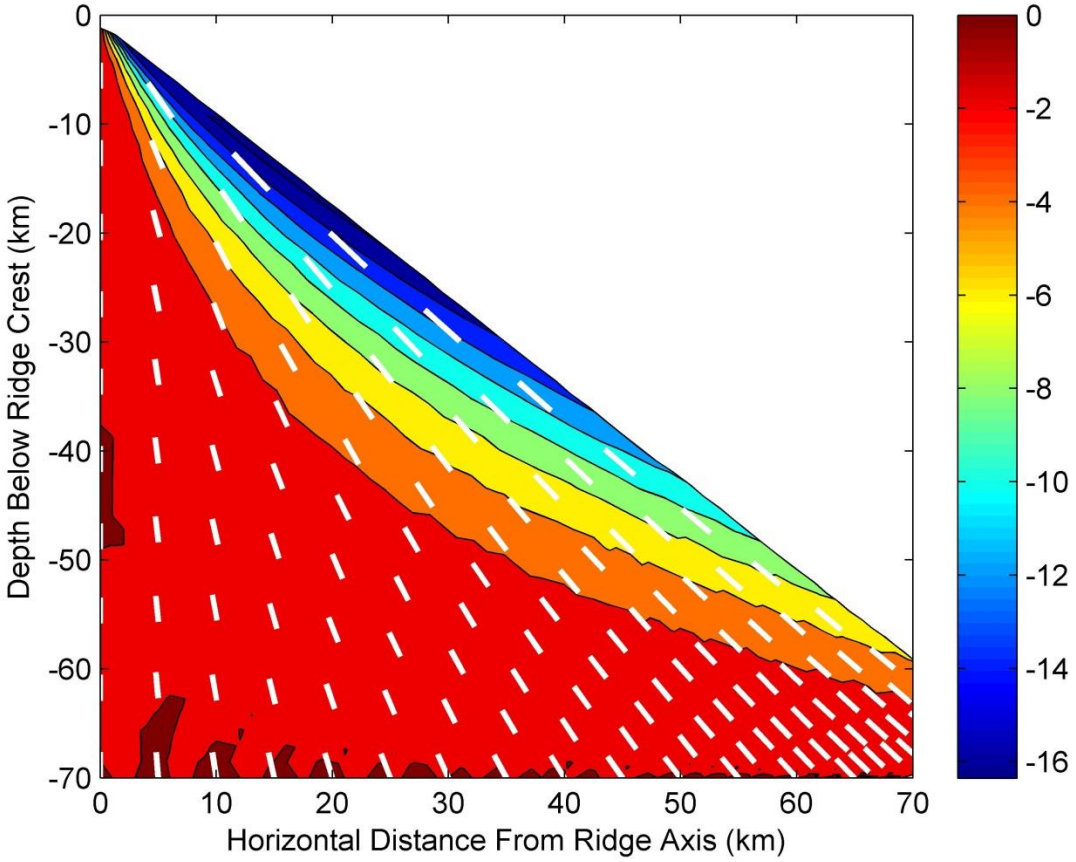

Figure 45: Contour plot of perturbation amplitude for bands evolved for preferential orientation toward the ridge axis for the case of a slow spreading ridge geometry with an anisotropic, strain rate independent matrix rheology.

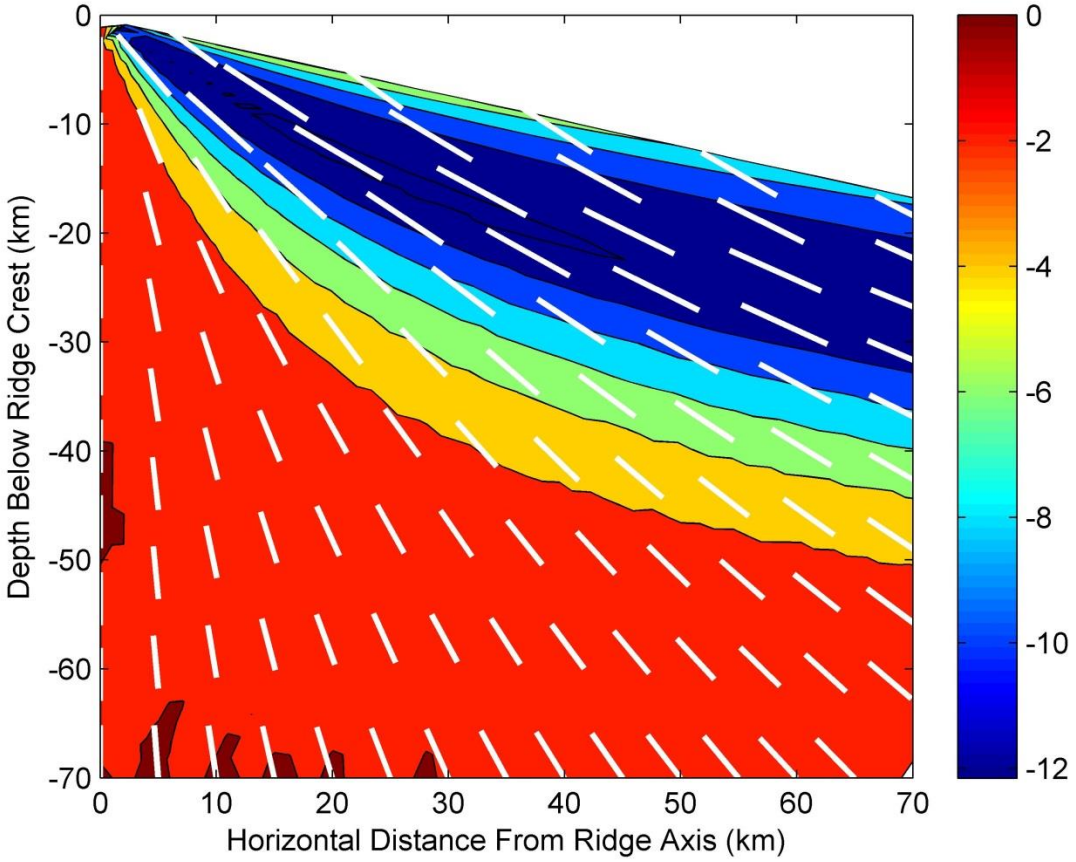

Figure 46: Contour plot of perturbation amplitude for bands evolved for preferential orientation toward the ridge axis for the case of a fast spreading ridge geometry with an isotropic, strain rate independent matrix rheology.

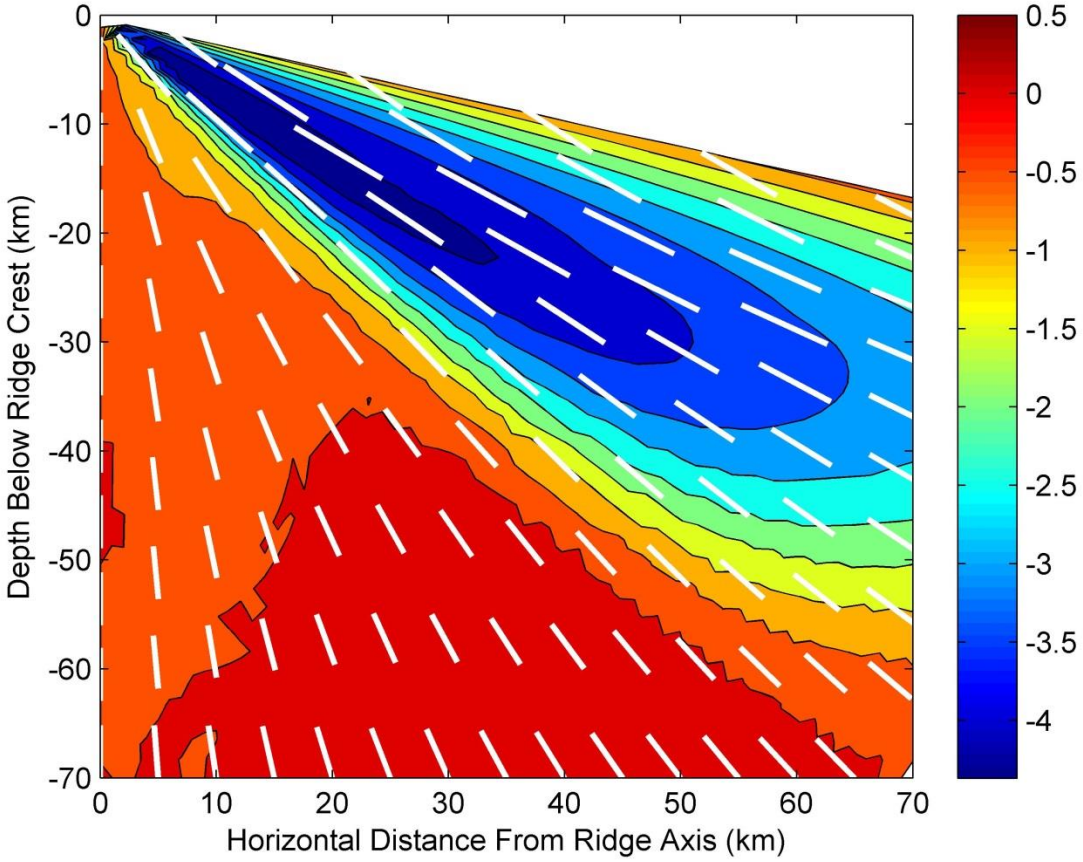

Figure 47: Contour plot of perturbation amplitude for bands evolved for preferential orientation toward the ridge axis for the case of a fast spreading ridge geometry with an isotropic, strain rate dependent $(n_v = 6)$ matrix rheology.

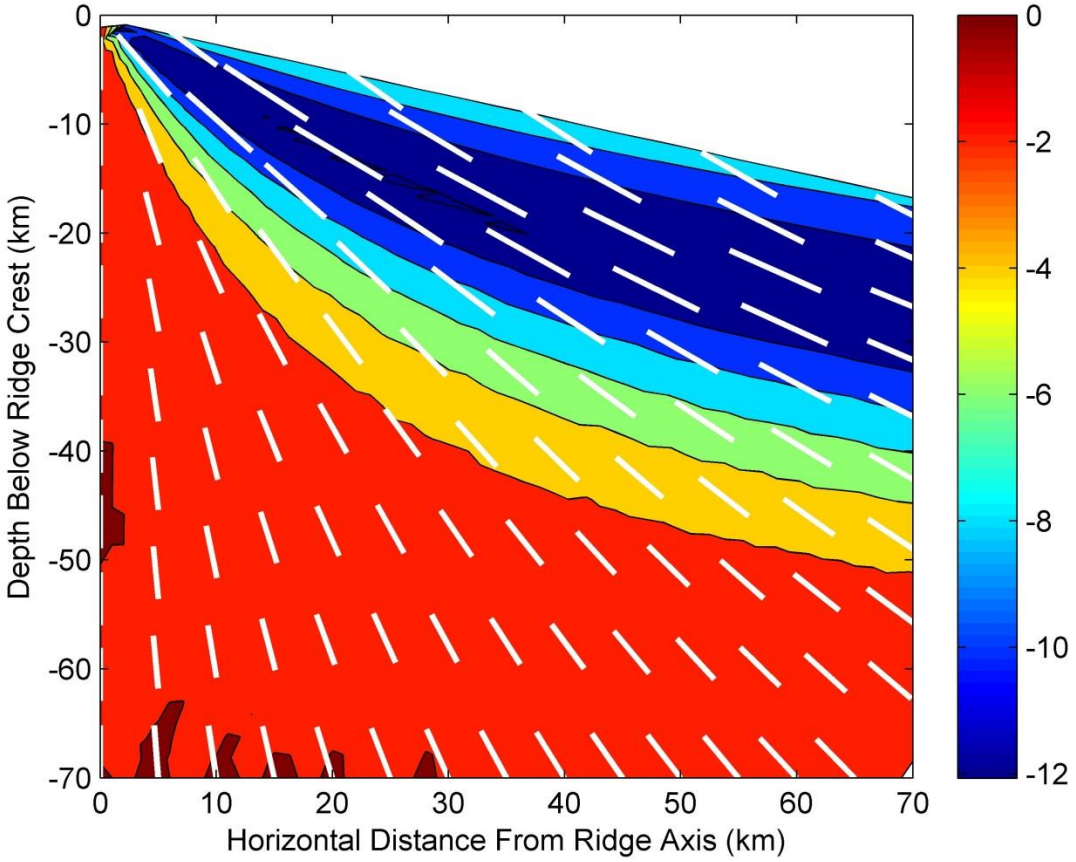

Figure 48: Contour plot of perturbation amplitude for bands evolved for preferential orientation toward the ridge axis for the case of a fast spreading ridge geometry with an anisotropic, strain rate independent matrix rheology.

Appendix 8: Anisotropic Nonlinear Simulation Results

All of the anisotropic simulations shared a lack of significant band development. Using slow-spreading ridge geometry, the models along streamlines 15 km and 30 km from the ridge axis saw brief band-like structures form of very low amplitude. These bands did not persist long, and were not as well defined as any of the bands shown in Figures 23 through 26. The 60 km streamline model saw no bands form at all. For the fast-spreading ridge geometry, the results were very similar: the 15 km and 30 km streamline models saw low-amplitude bands form early in the model and then disappear as the model progressed, while the 60 km streamline model saw no significant bands form. Both the fast-spreading and slow-spreading models progressed slightly further along streamlines than their isotropic counterparts, although all of the anisotropic models reached values of ϕ_{max} at their end that exceeded the RCMF. All of the anisotropic simulations demonstrated a significant amount of porosity accumulation on the boundaries of the model domain.

The angular spectra for the anisotropic nonlinear models are shown in Figures 49 and 50. The 15 km spectra, shown in the top panels of both figures, best demonstrate the early time, low amplitude bands that were present over the course of the simulations. The 30 km streamline spectra in Figure 50 also shows the presence of low amplitude bands in early time. By comparison, the early-time bands in the slow-spreading 30 km spectra in Figure 49 are significantly reduced in amplitude. All of the spectra present orientations consistent with the numerical instability discussed with the isotropic spectra, especially late in the model run time. The prevalence of these orientations in the anisotropic spectra indicates that the band growth is insignificant when compared to the magnitude of the numerical instability at these times.

15 km

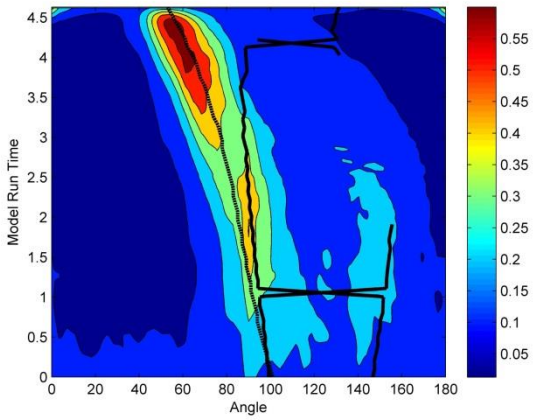

30 km

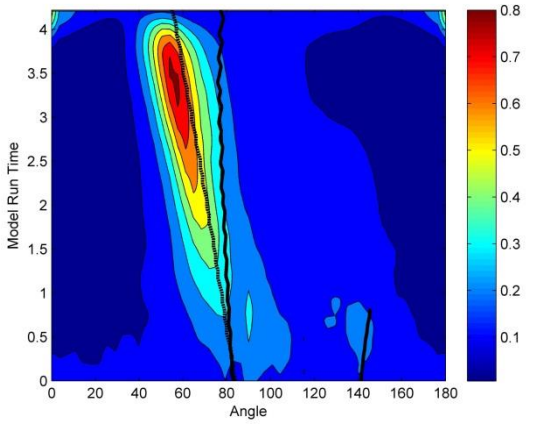

60 km

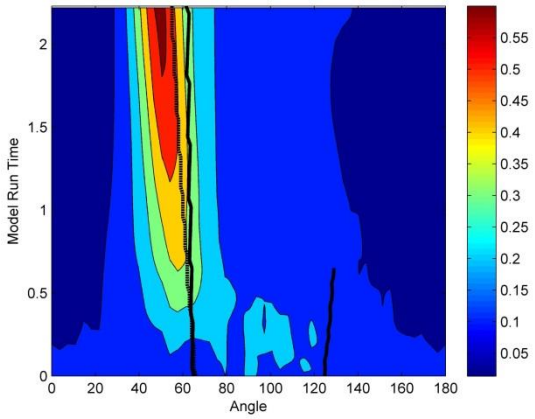

Figure 49: Angular power spectra for the nonlinear simulation with an anisotropic, strain rate independent matrix rheology and slow-spreading ridge geometry along all three considered streamlines.

15 km

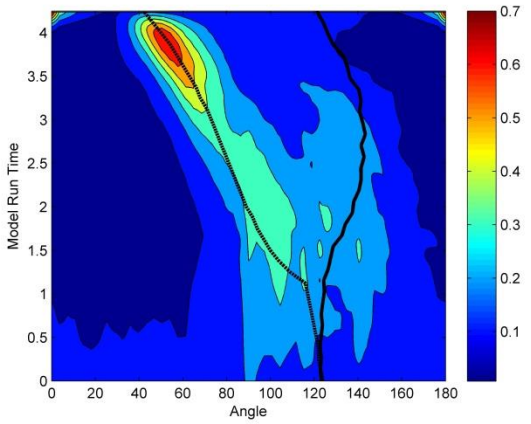

30 km

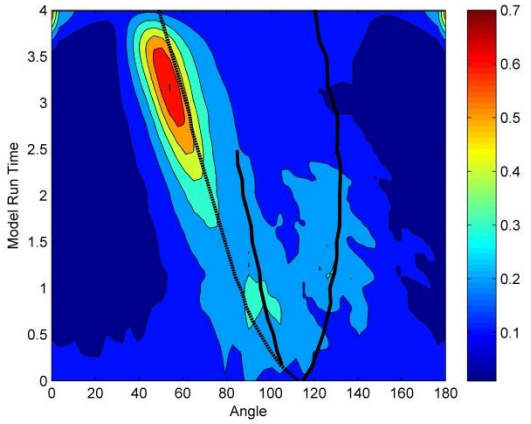

60 km

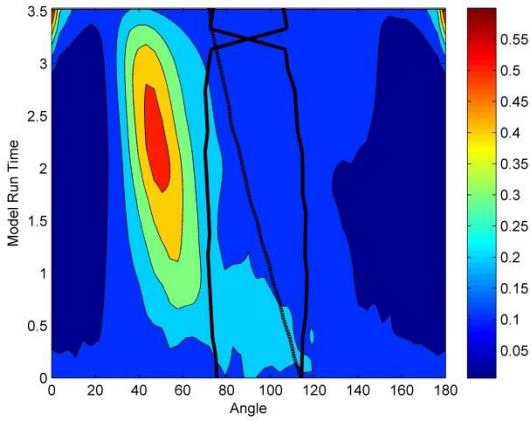

Figure 50: Angular power spectra for the nonlinear simulation with an anisotropic, strain rate independent matrix rheology and fast-spreading ridge geometry along all three considered streamlines.